Australian Government
Geoscience Australia

Uranium mineralisation events in Australia

Geochronology of the Nolans Bore, Oasis, Kintyre, Mt Gee-Armchair, and Maureen uranium deposits

Edited by Roger G. Skirrow

With contributions from David L. Huston, Roger G. Skirrow, Geoff L. Fraser, Andrew Cross, Natalie Kositcin, Robert A. Creaser, Roland Maas, Stephen B. Hore, Subhash Jaireth, Kelvin Hussey

Record
2011/12

GeoCat # 71639

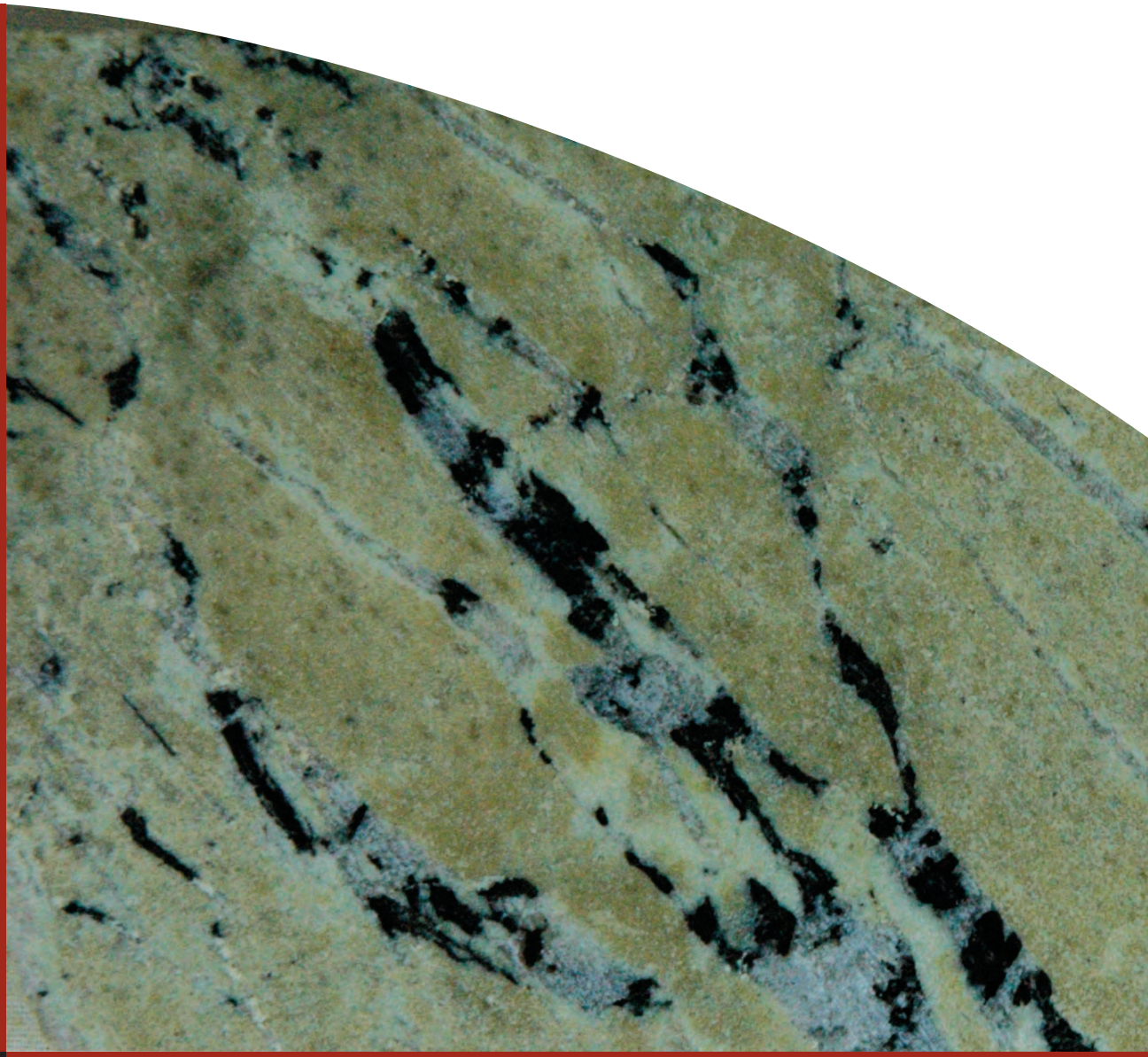

Uranium mineralisation events in Australia: geochronology of the Nolans Bore, Oasis, Kintyre, Mt Gee-Armchair, and Maureen uranium deposits

GEOSCIENCE AUSTRALIA
RECORD 2011/12

Edited by

Roger G. Skirrow

With contributions from

David L. Huston[1], Roger G. Skirrow[1], Geoff L. Fraser[1], Andrew Cross[1], Natalie Kositcin[1], Robert A. Creaser[2], Roland Maas[3], Stephen B. Hore[4], Subhash Jaireth[1], Kelvin Hussey[5]

[1] Geoscience Australia, Onshore Energy and Minerals Division, GPO Box 378, Canberra, ACT 2601
[2] University of Alberta, Edmonton, Alberta, Canada T6G 2R3
[3] University of Melbourne, Victoria 3010
[4] Primary Industries and Resources South Australia, Adelaide, South Australia
[5] Arafura Resources Ltd, PO Box 37220, Winnellie, Northern Territory 0821

Department of Resources, Energy and Tourism
Minister for Resources and Energy: The Hon. Martin Ferguson, AM MP
Secretary: Mr John Pierce

Geoscience Australia
Chief Executive Officer: Dr Chris Pigram

ISSN 1448-2177
ISBN 978 1 921781 93 3 (web copy)
978 1 921781 94 0 (hardcopy)

GeoCat # 71639

Bibliographic reference for GA Record: Skirrow, R.G. (editor), 2011. Uranium mineralisation events in Australia: geochronology of the Nolans Bore, Oasis, Kintyre, Mt Gee-Armchair, and Maureen uranium deposits. Geoscience Australia Record 2011/12, 89 pp.

Bibliographic reference for Chapter, e.g.: Huston, D.L., Maas, R. Fraser, G. and Hussey, K., 2011. Nolans Bore REE-U-Th deposit, Northern Territory. *In:* Skirrow, R.G. (editor), Uranium mineralisation events in Australia: geochronology of the Nolans Bore, Oasis, Kintyre, Mt Gee-Armchair, and Maureen uranium deposits. Geoscience Australia Record 2011/12, p. 9-20.

Contents

Abstract

This report presents new geochronological results for five uranium deposits in Australia, detailing the timing of uranium mineralisation in relation to regional geological events. The purpose of the study is to better constrain ore genetic and exploration models for these uranium mineral systems, and ultimately to improve understanding of the uranium resource potential of the Australian continent. The work was carried out under the auspices of the Onshore Energy Security Program.

Each of the five uranium deposits represents a different style of mineralisation within three broad families of uranium mineral systems: magmatic-related, basin-related, and 'metamorphic'-related. The results contribute to the current paucity of age data for uranium deposits in Australia, and for most of the deposits the new dates are the first reported direct ages for mineralisation or associated alteration.

The Nolans Bore rare earth element – uranium – thorium (REE-U-Th) deposit in the Northern Territory is one of Australia's most important REE resources, and contains mineralised fluorapatite-rich veins hosted by Paleoproterozoic granitic gneiss. Fluorapatite was dated by the U-Pb TIMS method and yielded an age of 1244 ± 10 Ma, interpreted to be the minimum age of REE-U-Th mineralisation in the Nolans Bore deposit. Muscovite and biotite in a mylonitic shear zone within the granitic gneiss yielded ^{40}Ar-^{39}Ar ages between 345 ± 2 Ma and 377 ± 2 Ma, attributed to the effects of the Alice Springs Orogeny.

The major undeveloped Kintyre uranium deposit in the Paterson Province of northern Western Australia is thought to be a member of the unconformity-related deposit class. Reconnaissance dating of uraninite mineralisation by the electron microprobe chemical (U-Th-Pb) dating method has revealed an age of 837 $^{+35}/_{-31}$ Ma. Although this is interpreted as a minimum age, and the regional event chronology is not well established, this age is consistent with uranium introduction and/or remobilisation during or soon after deposition of the Yeneena Basin, which unconformably overlies the Rudall Complex host to mineralisation. The age also overlaps with the age of the Miles Orogeny, with which copper mineralisation at the Nifty deposit is believed to be associated.

The Oasis uranium deposit in the Etheridge Province of north Queensland is hosted by a mylonitic biotite-rich shear zone, within Mesoproterozoic (1559 ± 3 Ma) granite. The ages of uraninite (433 ± 3 Ma, determined by electron microprobe U-Th-Pb chemical dating) and of micas in the shear zone (~429-439 Ma, determined by ^{40}Ar-^{39}Ar dating of biotite and muscovite) are very similar, strongly suggesting that uranium was introduced at this time and during shearing. Alternatively the uranium was remobilised during a mid Silurian tectonothermal event.

Uranium-REE deposits in the Mt Gee-Armchair area of the Mt Painter Province, South Australia, are mineralogically similar to some iron oxide copper-gold (IOCG) deposits, despite the apparent lack of copper and gold. Molybdenite associated with uraninite in the Armchair deposit yielded three Re-Os isotope ages between 361 ± 2 Ma and 365 ± 2 Ma. If the Mt Gee-Armchair U-REE deposits have affinities with the IOCG deposit class, these would represent the first known IOCG-related mineralisation recognised in the Paleozoic of eastern Australia. The mineralising event appears to have been synchronous with parts of the Kanimblan Orogeny.

The Maureen U-Mo deposit in north Queensland has been variously interpreted as a volcanic-associated or unconformity-related deposit. Fluorite associated with the U-Mo mineralisation yielded a TIMS U-Pb age of ~330 ± 10 Ma, which is interpreted to represent a possible age of the U-Mo mineralisation. Although new data were also obtained on the age of the basin host rocks (U-Pb SHRIMP zircon, maximum depositional age of ~342-335 Ma), the results do not discriminate between alternative mineralisation models.

1. Introduction

Roger G. Skirrow[1]

1.1 PURPOSE AND SCOPE

Australia hosts the world's largest resources of uranium, including the largest single resource in the Olympic Dam deposit, South Australia (IAEA, 2009). The three operating uranium mines in Australia contribute significantly to the nation's export earnings, and will be augmented by several new uranium mines in coming years. A fundamental dataset in understanding where and how uranium deposits form, and in predicting where undiscovered deposits may occur, is the age of mineralisation. Despite the significance of Australia's uranium deposits, only 14 of the 98 deposits listed in the OZMIN database have information on age (Geoscience Australia, 2011).

This report presents new geochronological results for five uranium deposits in different geological settings in Australia, and represents work undertaken as part of the Onshore Energy Security Program (OESP, 2006-2011) at Geoscience Australia. The purpose of the geochronology is to provide constraints on the timing of uranium mineralisation in relation to regional geological events, so that more robust ore formation and exploration models can be built. These results are being used in the OESP to assess the potential for undiscovered uranium resources in Australia (see also Huston et al., 2009; Schofield, 2010).

Following Chapter 2 on Analytical Methods, Chapters 3 to 7 present results for each of the five uranium deposits: Nolans Bore, Kintyre, Oasis, Mt Gee-Armchair, and Maureen (Fig. 1.1). Chapter 8 presents a summary of the new results. The deposits are presented in order of determined age.

1.2 URANIUM MINERAL SYSTEMS, AND DEPOSITS INVESTIGATED

The deposits discussed in this report are very diverse in age, geological setting, type, and economic significance. Using the IAEA classification scheme for uranium deposits, McKay and Miezitis (2001) described the Kintyre deposit as 'unconformity-related', the Maureen deposit as 'volcanic', and the Mt Gee-Armchair deposits as 'breccia complex' deposits (Table 1.1). The Nolans Bore and Oasis deposits are relatively recent discoveries. The Nolans Bore deposit would be classified as 'intrusive' or 'vein' type in the IAEA scheme, whereas the Oasis deposit is hosted by a biotite-rich shear zone within albite-altered granite and could be considered as a 'vein' or 'metasomatic' or 'metamorphic' type deposit in the IAEA scheme.

Alternative schemes for classifying uranium deposits have been proposed, based on genesis or process (Plant et al., 1999; Cuney, 2009; Skirrow et al., 2009). Based on the *mineral systems* concept and on the fundamental fluid types involved in the formation of these deposits, Skirrow et al. (2009) proposed three families of uranium mineral systems: magmatic-related, basin- and surface-related, and 'metamorphic'-related. Deposit types in the IAEA classification may be placed within the tripartite mineral systems scheme, which provides a framework for understanding the genetic relationships between deposit types (Fig. 1.2).

[1] Geoscience Australia, GPO Box 378, Canberra, ACT 2601, Australia

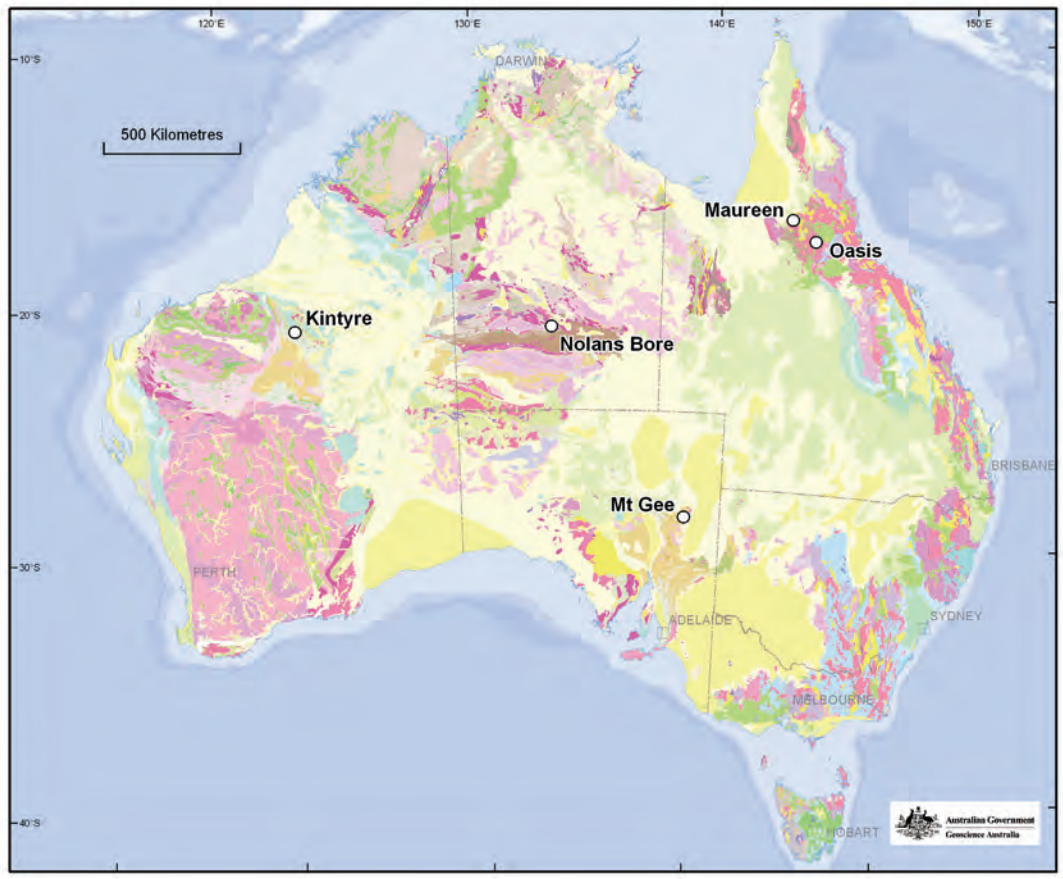

Figure 1.1: *Location of uranium deposits investigated in this study. Geology of Australia from Geoscience Australia.*

Table 1.1: Summary of uranium deposits investigated in this study.

Deposit	Location	[1]Deposit type	[2]Mineral system	Size / grade	[4]Ownership
Nolans Bore	Central-south NT	Intrusive	Magmatic-related	30 Mt @ 2.8% REO, 0.020% U_3O_8	Arafura Resources
Kintyre	Rudall Complex, northern WA	Unconformity-related	Basin-related	[3]36,000 t U_3O_8	Cameco, Mitsubishi Development
Oasis	Etheridge Province, north Qld	Vein or metasomatic or metamorphic	'Metamorphic'-related	0.10-0.17% U_3O_8	Lease in application
Mt Gee/Armchair	Mt Painter Province, northeast SA	Breccia complex	Hybrid - IOCGU	51 Mt @ 0.061% U_3O_8	Marathon Resources
Maureen	Georgetown Province, north Qld	Volcanic or unconformity-related	Basin-related or magmatic-related?	3.28 Mt @ 0.10% U_3O_8, 0.07% Mo	Mega Uranium

[1] Deposit type, after IAEA classification scheme

[2] Uranium mineral system, based on Skirrow et al. (2009)

[3] 'Probable resource' + inferred resource, Gauci and Cunningham (1992)

[4] Ownership status as of February 2011

Using this scheme, the five deposits investigated in this study (Table 1.1) are positioned in Figure 1.2. Within the basin- and surface-related family of systems, there is a continuum of ore-forming fluids from meteoric or seawater through groundwaters and formation waters to diagenetic fluids. Unconformity-related deposits, of which the major Kintyre deposit is believed to be an example, are envisaged to have formed by the reaction of basin-derived, oxidised, diagenetic fluids or formation waters with chemical reductants near the interface between the basin and the underlying basement. The Maureen deposit has been attributed to the 'volcanic' deposit type (e.g., McKay and Miezitis, 2001), but Wall (2006), Hurtig (2008) and Mathison and Hurtig (2009) interpreted the deposit as unconformity-related. The new geochronology results presented herein for both Kintyre and Maureen provide constraints on previous mineralisation models, aimed at testing for example whether uranium was introduced synchronously with volcanism at Maureen, or later during basin diagenesis.

At higher temperature-pressure conditions fluids of surface or basinal origin may become difficult to distinguish from fluids of true metamorphic origin (i.e., from devolatilisation reactions), as the crustal fluids equilibrate chemically and isotopically with metamorphic rocks. For this reason Skirrow et al. (2009) grouped fluids that have reacted at elevated temperature-pressure conditions with metamorphic rocks as 'metamorphic' fluids. Many of the so-called 'vein' type and 'metasomatic' uranium deposits are considered to have formed from such 'metamorphic' fluids or from mixtures of these with magmatic-hydrothermal fluids. From the limited information available for the Oasis deposit, we suggest it is a member of the 'metamorphic'-related uranium mineral system family. The geochronology study aims to test which tectono-thermal event was responsible for this uranium mineralisation in north Queensland.

The Nolans Bore deposit is an unusual rare earth element (REE) deposit with significant tonnages of low grade uranium and thorium mineralisation (Chapter 3). Uranium and REE mineralisation occurs in fluorapatite-rich veins hosted mostly by Paleoproterozoic granitic gneiss. A key question prompting the current geochronology study is whether the mineralisation is genetically related to the host igneous rocks, or to later events. The relative importance of magmatic-hydrothermal fluids versus 'metamorphic' fluids has yet to be established for this deposit, but at this stage we group Nolans Bore within the magmatic-related mineral system family.

Uranium-bearing iron oxide copper-gold deposits such as the Olympic Dam deposit are considered to be hybrids, involving both deep-sourced fluids of possible magmatic-hydrothermal origin and fluids of surficial or basinal origin (Skirrow et al., 2009). The Mt Gee-Armchair deposits arguably are members of this diverse class of mineral deposits, although copper and gold are at low levels in the known prospects in this district (Chapter 6). Since the discovery of the Olympic Dam deposit in 1975 comparisons have been made between the Mt Gee U-REE deposit and this giant Mesoproterozoic deposit (e.g., Youles, 1975; Lambert et al., 1982). Dating of the Mt Gee-Armchair uranium mineral system was undertaken to test whether a component of the mineralisation was Mesoproterozoic or younger (e.g., Paleozoic) in age.

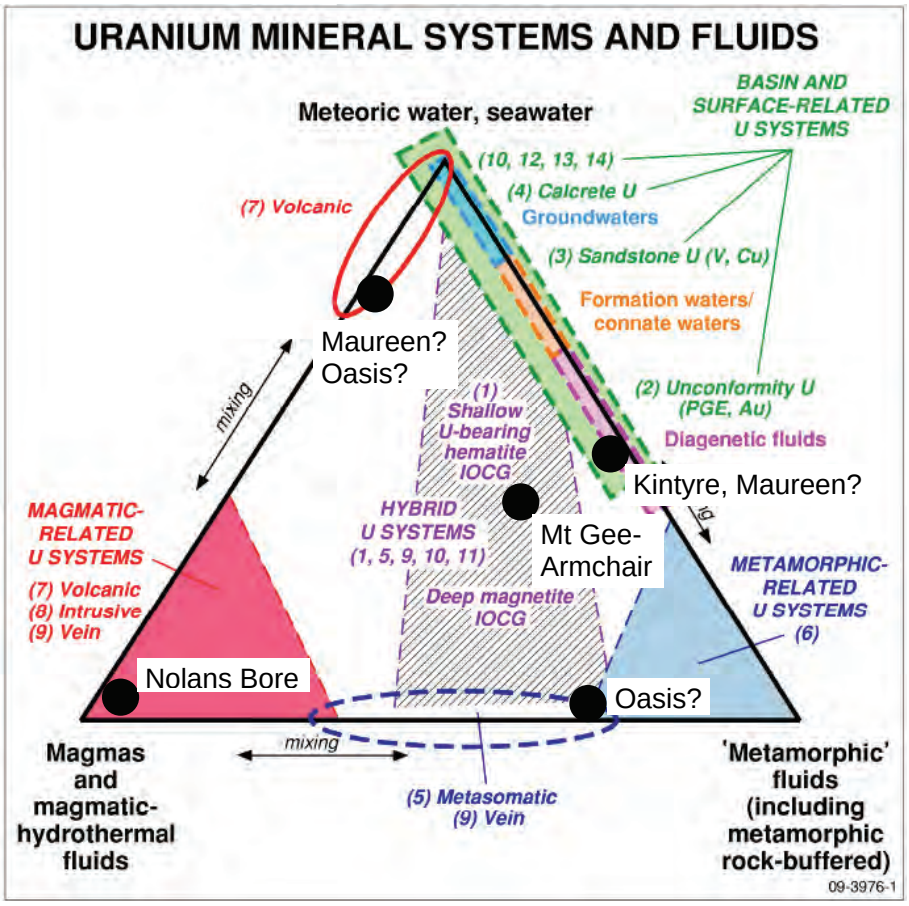

Figure 1.2: *Scheme of three families of uranium mineralising systems, and three end-member fluid types. For reference, numbered deposit types are from the IAEA Red Book, in order of economic importance in Australia. Source: Skirrow et al. (2009).*

2. Analytical methods

Robert Creaser[1], Andrew Cross[2], Geoff Fraser[2], Natalie Kositcin[2], and Roland Maas[3]

This section briefly describes analytical methods used in subsequent chapters of this Record. Additional details are provided in individual chapters.

2.1 U-PB AND RB-SR METHODS

Isotope dilution U-Pb and Sm-Nd analyses were carried out at the University of Melbourne using procedures modified from Woodhead et al. (2006) and Maas et al. (2005). Apatite from Nolans Bore (which contains silicate impurities) was dissolved in HNO_3 or $HF/HNO_3/HCl$, and 6M HCl was used to dissolve fluorite. Samples were spiked with ^{233}U-^{205}Pb and ^{149}Sm-^{150}Nd traces as appropriate, followed by separation of Pb and U using conventional HBr-HCl anion exchange (AG-1 X8, 100-200) and EICHROM TRU resin; Sm-Nd separations were done with EICHROM RE and LN resin. Procedural blanks are 50±25 pg Pb, 5 pg U and <100 pg Nd. All isotopic analyses were carried out on a NU Plasma multi-collector ICPMS. Instrumental mass bias for Pb was corrected by standard bracketing with SRM981, while Nd mass bias was corrected by normalizing to $^{146}Nd/^{145}Nd=2.0719425$ (equivalent to $^{146}Nd/^{144}Nd = 0.7219$). Nd isotope data are reported relative to La Jolla = 0.511860; $^{147}Sm/^{144}Nd$ and $^{143}Nd/^{144}Nd$ for BCR-2 give 0.1382±2 and 0.5126400±20 (2sd), consistent with TIMS reference values. Mt Dromedary titanite yields concordant Pb/U ages of ~99 Ma, consistent with the known Ar-Ar age. The decay constants used are: ^{147}Sm $6.54e^{-12}$ a^{-1}, ^{238}U $0.155125e^{-9}$ a^{-1} and ^{235}U $0.98485e^{-9}$ a^{-1}

2.2 RE-OS METHODS

Methods used for molybdenite Re-Os isotope analysis are described in detail by Selby and Creaser (2004). The ^{187}Re and ^{187}Os concentrations in molybdenite were determined by isotope dilution mass spectrometry using Carius-tube, solvent extraction, anion chromatography and negative thermal ionization mass spectrometry techniques. For this work, a mixed double spike containing known amounts of isotopically enriched ^{185}Re, ^{190}Os, and ^{188}Os analysis was used. Isotopic analysis was made using a ThermoScientific Triton mass spectrometer by Faraday collector. Total procedural blanks for Re and Os are <3 picograms and <2 picograms, respectively. These procedural blanks are insignificant in comparison to the Re and Os concentrations in molybdenite. The Chinese molybdenite powder HLP-5 (Markey et al., 1998), which is used as an in-house "control sample" by the AIRIE group, Colorado State University, is also routinely analyzed at the University of Alberta. For this "control sample" we determined a Re-Os date of 221.7 ± 1.0 Ma during the course of analyses, with an average Re-Os date of 220.52 ± 0.24 Ma recorded over a 5 year period (n=17). This Re-Os age date is identical to that reported by Markey et al. (1998) of 221.0 ± 1.0 Ma. In addition, the age determined for the Henderson Molybdenite Reference Material using the above methods and instrumentation, was 27.71 ± 0.13 Ma, in accord with previous determinations (Markey et al., 2007). The decay constant used for ^{187}Re is $1.666e^{-11}.a^{-1}$ (Smoliar et al., 1996).

[1] University of Alberta, Edmonton, Alberta, Canada T6G 2R3
[2] Geoscience Australia, GPO Box 378, Canberra, ACT 2601, Australia
[3] University of Melbourne, Victoria 3010, Australia

2.3 ^{40}AR/^{39}AR METHODS

Mineral separates for $^{40}Ar/^{39}Ar$ analysis were prepared at Geoscience Australia, via standard methods, including crushing, sieving, heavy liquid density separation, and hand picking. Samples were packed at the University of Queensland argon laboratory for irradiation. Aliquots of pure mineral separate were loaded into pits in an aluminium disk together with the standard material Fish Canyon Sanidine (FCs, age = 28.201 ± 0.046 Ma, Kuiper et al., 2008). The pits in the irradiation disk were enclosed with an aluminium cover, and wrapped in aluminium foil before being vacuum heat-sealed into quartz vials and irradiated for 42 hours in the Cadmium-lined B-1 CLICIT facility at Oregon State University. Following irradiation, samples were baked under vacuum at ~200°C for 12 hours. Step heating was conducted on multi-grain aliquots via a continuous-wave Ar-ion laser with a 2 mm wide defocussed beam, before isotopic analyses in a MAP215-50 mass spectrometer at the University of Queensland. Data processing, including correction for mass discrimination, nucleogenic interferences and atmospheric contamination, via the software "MassSpec version 7.527", written by Alan Deino. Instrumental mass discrimination was calculated using a $^{40}Ar/^{39}Ar$ value of 298.56 ± 0.31 for atmospheric argon (Renne et al., 2009).

The neutron fluence parameter, J, was determined for each Al-irradiation disk via laser total fusion and isotopic analysis of 15 individual aliquots of Fish Canyon sanidine. Plotting of data, and calculation of plateau ages, was via the Isoplot software of Ludwig (2001). Criteria used to define plateau ages are 60% of the total ^{39}Ar released in at least three consecutive heating steps with a minimum probability of fit of 0.05. Uncertainties on plateau ages include 0.16% (1σ) uncertainty in the J-parameter, but do not include uncertainties in the age of the standard material, or in the potassium decay constants. All ages are calculated using the decay constants recommended by Steiger and Jaeger (1977).

2.4 ELECTRON MICROPROBE U-TH-PB CHEMICAL DATING OF URANINITE

Chemical U-Th-Pb dating by electron microprobe (EPMA) was mostly developed for the dating of monazite in the early 1990's (e.g., Suzuki & Adachi, 1991; Montel et al., 1996; Cocherie et al., 1998; Williams et al., 1999) and since then has been applied in numerous studies in the literature. Only relatively few studies have used this method for the dating of uraninite (e.g., Bowles, 1990; Förster, 1999; Kempe, 2003; Polito et al., 2005; Zacharias et al., 2008).

Chemical U-Th-Pb dating is based on the premise that all Pb in the sample is radiogenic, derived solely from the radioactive decay of ^{235}U, ^{238}U and ^{232}Th. The three independent decay schemes: ^{232}Th-^{208}Pb; ^{235}U-^{207}Pb and; ^{238}U-^{206}Pb are then combined into a composite age equation.

$$Pb_{conc} = \frac{Th_{conc}}{232}(e^{\lambda 232t} - 1)208 + \frac{U_{conc}(0.9928)}{238.04}(e^{\lambda 238t} - 1)206 + \frac{U_{conc}(0.0072)}{238.04}(e^{\lambda 235t} - 1)207$$

Where Pb_{conc}, U_{conc} and Th_{conc} are the EPMA determined concentrations in ppm, that are converted into atomic proportions and λ232, λ238 and λ235 are the decay constants for ^{232}Th, ^{238}U and ^{235}U, respectively. Additionally, the concentration for each of the U isotopes is determined by multiplying their fractional natural abundance (i.e., present day $^{235}U/^{238}U$ = 1/137.88) by the U_{conc}. The equation can then be solved by iteratively substituting a value for t (time) into each of the three age equations until a solution is reached (Montel et al., 1996). There are two important limitations inherent to

chemical U-Th-Pb dating. Firstly, the presence of common Pb cannot be measured, and secondly any post-crystallisation, non-radiogenic modification to either the U-Pb or Th-Pb ratios cannot be assessed.

2.4.1 Uraninite analytical procedures

Uraninite grains from the Kintyre deposit were separated from crushed and sieved rock samples at the Mineral Separation Laboratory, Australian Nuclear Science and Technology Organisation, at Lucas Heights, Sydney. The uraninite grains were then mounted in epoxy resin and polished to reveal their interiors, and photomicrographs were taken in reflected light. Uraninite grains from the Oasis deposit were identified *in situ* using SEM imaging of polished thin sections. Backscattered scanning electron microscope imaging was carried out to determine the most suitable areas for EPMA analysis.

EPMA analyses were undertaken using a Cameca SX100 electron microprobe located at the Research School of Earth Sciences, Australian National University, Canberra. The uraninite grains were analysed for U, Th, Pb, Y, Si, Ca, Ti and Fe using a 15 kV electron beam regulated at 100 nA. The X-ray lines were Pb*Mα*, Th*Mα* and U*Mβ*. Counting times for Pb, Th and U were 150 s, 60 s and 60 s, respectively Uraninite age calculations were done with the EPMA dating Excel® Add–In of Pommier et al. (2002). The uraninite standard U6897 (TIMS U-Pb age between ~1058 to ~1043 Ma; W. Davis, pers. comm.) was used as an internal check for the EPMA U-Th-Pb chemical dating results.

3. Nolans Bore REE-U-Th deposit, Northern Territory

David Huston[1], Roland Maas[2], Geoff Fraser[1] and Kelvin Hussey[3]

The Nolans Bore deposit, along with the Mount Weld deposit in Western Australia, are members of an emerging group of Australian rare earth element (REE) deposits in line to commence production in the next few years. Although the main commodities present at Nolans Bore are rare earth elements, this deposit differs from other primary rare earth element deposits in having uranium and phosphorus as significant byproducts. In addition, the deposit also contains high concentrations of thorium, which will be stockpiled against future possible demand. To constrain the timing of mineralisation, a series of samples were collected from the host rocks, the mineralised apatite veins, a pegmatite vein that cuts and is cut by the veins, and late mylonites. This contribution presents the results of isotopic analyses of apatite from the veins and mica from the mylonites.

3.1 GEOLOGICAL SETTING

The Nolans Bore prospect is located on the southern end of the Reynolds Range near Aileron in south-central Northern Territory (Fig. 3.1). Historically, supracrustal rocks in the Reynolds Range have been divided into two broad units: the Lander Rock beds and the Reynolds Range Group. The Lander Rock beds comprise (meta)turbiditic rocks that range in metamorphic grade from greenschist to granulite. These rocks are overlain unconformably by metaquartzite, slate, schist and marble of the Reynolds Range Group.

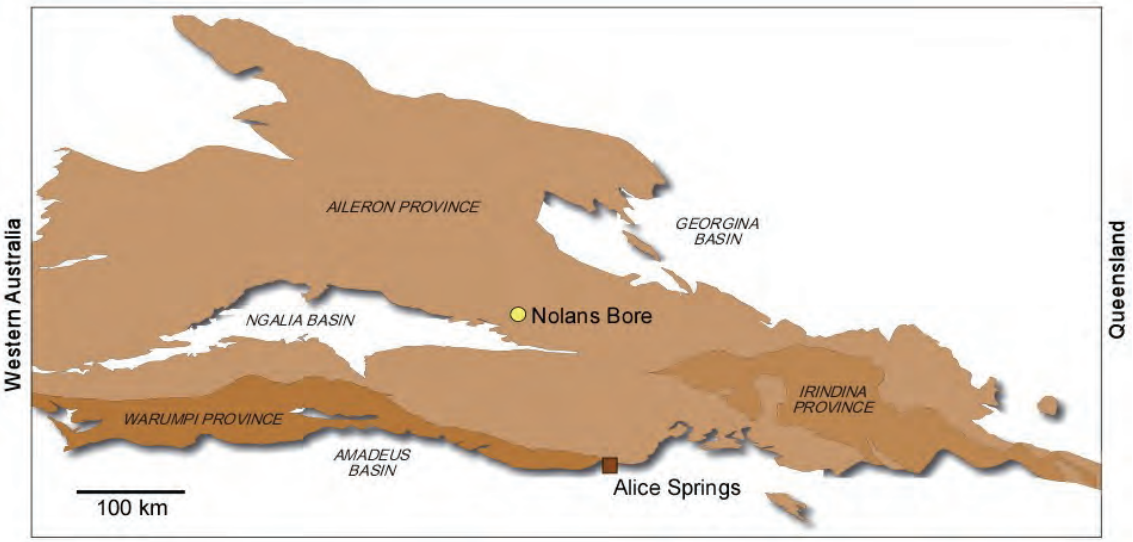

Figure 3.1: *Regional geology of the southern Northern Territory showing the location of the Nolans Bore deposit. Base map is courtesy Northern Territory Geological Survey.*

[1] Geoscience Australia, GPO Box 378, Canberra, ACT 2601, Australia
[2] University of Melbourne, Victoria 3010, Australia
[3] Arafura Resources Ltd, PO Box 37220, Winnellie, Northern Territory 0821

Claoué-Long et al. (2008) suggested the Lander Rock beds comprise two temporally discrete, though similar appearing, turbiditic packages. The oldest package is interpreted to have been deposited between 1840 and 1810 Ma based on detrital zircon populations and intrusive relationships. This unit is (presumably) overlain by the second package which was deposited between ~1805 (Claoué-Long et al., 2008) and ~1780 Ma (age of metavolcanic Coniston Schist: Smith, 2001). The uppermost Paleoproterozoic unit in the region, the Reynolds Range Group, is constrained by a maximum depositional age of ~1785 Ma and a minimum provided by the deposition at ~1780 Ma of sediments forming the Coniston Schist (Smith, 2001).

Granite intrusion occurred in the Reynolds Range area between ~1820 and ~1770 Ma (Young et al., 1995; Collins and Williams, 1995; Vry et al., 1996). The supracrustal rocks and granites were overprinted by high grade metamorphism (to granulite facies) during the Chewings Event, which has been dated using metamorphic monazite and zircon overgrowths at between 1595 and 1565 Ma (Vry et al., 1995; Williams et al, 1996; Rubatto et al., 2001). Collins and Williams (1995) obtained a similar age for pegmatite emplacement during this event.

The Reynolds Range has a characteristic northwest-southeast grain defined in large part by similarly oriented shear zones and faults. These late shear zones have been dated at ~333 Ma using both Rb-Sr and Ar-Ar techniques (Cartwright et al., 1999), suggesting that they were active during the later stages of the Alice Springs Orogeny.

3.2 NOLANS BORE REE-U-TH DEPOSIT

The Nolans Bore REE-U-Th and phosphorus (P) deposit (Fig. 3.2) contains a JORC-compliant mineral resource of 30.0 million tonnes at 2.8% rare earth element oxides (REO), 12.9% P_2O_5 and 0.020% U_3O_8 (including a measured resource of 5.1 Mt at 3.2% REO, 13.5% P_2O_5, and 0.026% U_3O_8). The deposit consists of a series of rare earth element-bearing fluorapatite veins that are hosted mostly by granite gneiss. The prospect area also contains Lander Rock beds (not shown in Figure 3.2), which locally comprise schist, phyllite, andalusite hornfels, garnet-cordierite-biotite-quartz granofels, sillimanite-biotite-cordierite-orthoclase granofels and tourmaline-bearing quartzite (Stewart, 1981). These rocks have been intruded by granites (now granite gneisses) that have been correlated with the Boothby Orthogneiss and the Napperby Gneiss. The Boothby Orthogneiss has an age of 1806 ± 4 Ma, whereas the Napperby Gneiss has an age of 1778 ± 8 Ma (Collins and Williams, 1995; Worden et al., 2008; both SHRIMP zircon U-Pb ages). Much of the deposit is covered by alluvial sand and gravel, which can be up to 4.5 m in thickness.

At surface (Fig. 3.2A), the deposit consists mostly of a series of east-northeast- to northeast-trending and steeply (65-90°) north-dipping fluorapatite veins (Fig. 3.2B) and breccias that are hosted in strongly kaolinitised granitic gneiss. Kaolinitic alteration does not persist at depth and is presumably related to weathering. The veins vary in thickness from 0.3 to 75 m and are concentrated in two zones, the northern zone and the southern zone. The northern zone is at least 700 m long and up to 200 m wide, whereas the eastern zone is narrower (50-100 m) and irregular, although it extends for at least 1000 m along strike (Fig. 3.2A).

Four styles of REE mineralisation have been recognised at Nolans Bore: (1) massive fluorapatite veins that typically contain 4-6% rare earth element oxides and constitute most of the defined resource, (2) very high-grade (7-10% REO) zones found in cheralite-bearing, apatite-poor kaolinitic

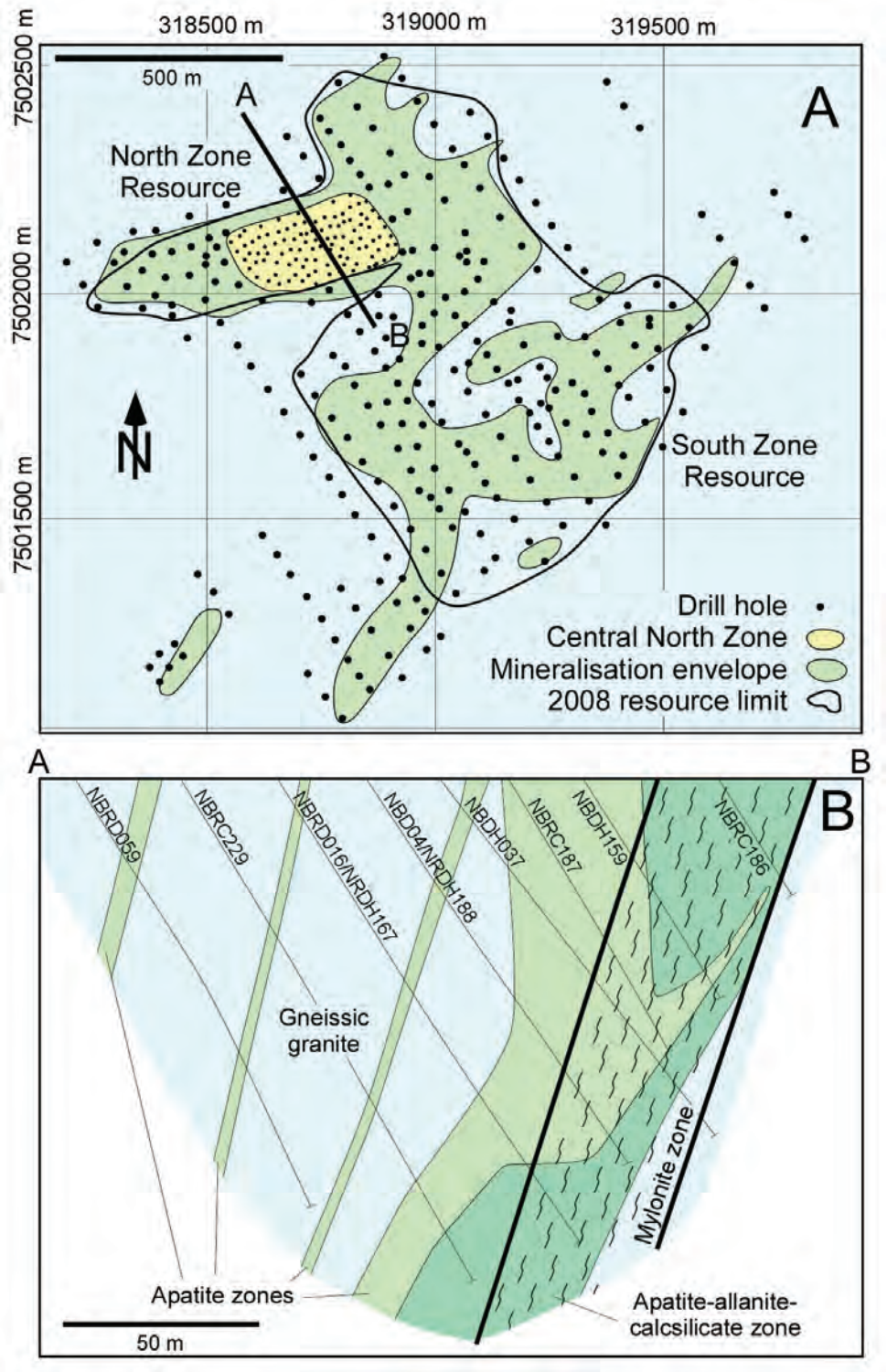

Figure 3.2: *Diagrams showing the (A) surface geology and (B) cross section of the Nolans Bore deposit. The location of the section in part (B) is shown in (A). Modified after www.arafuraresources.com.au.*

zones outside of the veins, (3) apatite-allanite-epidote zones hosted by calc-silicates, and (4) low-grade stockwork zones in gneiss and kaolinitised rock adjacent to the veins and mylonite zones. The high grade cheralite-rich zones are probably the result of supergene upgrading as they are associated with clay alteration and are present in the near surface parts of the deposit. The main difference between the ore types is the REE/P ratio, which is significantly higher in the high-grade cheralite-dominated zones outside of the main fluorapatite veins. In the veins, the apatite is generally fine-grained, although local zones are coarse-grained with grains up to 15 mm. Locally the apatite has been brecciated, with coarse clasts (to 15 mm) in a fine-grained matrix. Mineralogically, most of the REE are hosted by cheralite, a phosphate-deficient REE mineral. Only about 30-35% of the REE is hosted in the crystal structure of apatite.

3.3 SAMPLE DESCRIPTIONS

Samples for this study were mostly collected from diamond drill hole NBDH157, which passed through the host granite gneisses, intersecting several narrow veins in the upper part of the hole and an ~18-m-thick vein near the bottom of the hole. Table 3-1 summarises the characteristics of each sample analysed in this study; Figure 3.3 contains photographs of these three samples; and Figure 3.4 contains photomicrographs showing textural relationships in sample 2007080001-25.

Table 3.1: Samples analysed from the Nolans Bore deposit.

SAMPLE	LOCATION (HOLE, DEPTH)	DESCRIPTION	MINERAL SEPARATION AND ANALYTICAL METHODS
2007080001-10	NBDH157, 65.3-65.7 m	Coarse grained, foliated gneiss of granitic (*sensu lato*) composition dominated by leucocratic bands composed of polygonal-textured quartz, plagioclase and K-feldspar and bands of finer-grained recrystallised quartz (Fig. 3.3a). A few coarse-grained K-feldspar (perthitic microcline) augen are preserved and are wrapped by bands of recrystallised quartz. Narrow, discontinuous, anastamosing bands of biotite form a strong foliation. Muscovite is not present in this sample.	Biotite was separated using standard techniques. Analysed using laser ^{40}Ar-^{39}Ar step heating.
2007080001-11	NBDH157, 67.1-67.3 m	Similar characteristics to 2007080001-10 except for the presence of a ~2-cm-wide, dark coloured, mylonitic band (Fig. 3.3b) oriented sub-parallel with the foliation in the host granitic gneiss. The mylonitic band consists of broad zones overwhelmingly dominated by aligned biotite, and narrow, discrete, light coloured bands of aligned muscovite. In most cases the biotite and muscovite have the same orientation, but a small proportion of the muscovite occurs as individual crystals oriented at high angle to the preferred orientation. The presence of muscovite in this sample, as well as the much higher concentration of biotite, distinguishes it from the host granitic gneiss.	The mica rich mylonitic band was carefully cut from the host gneiss before mineral separation in an attempt to date the mylonitic mica fabrics. Both biotite and muscovite were separated using standard techniques and analysed using laser ^{40}Ar-^{39}Ar step heating.
2007080001-25	NBDH157, 136.0-136.2 m	Massive to weakly brecciated apatite cut by calcite-allanite veins (Figs. 3.3c and 3.4a). The apatite contains abundant inclusions (Fig. 3.4b) of thorite, Th-Ce silicates and rare-earth element fluorocarbonates. In addition to allanite, the calcite veins contain minor to trace quantities of rare-earth element fluorocarbonates (Fig. 3.5c), barite, uranium silicate minerals and monazite.	Apatite, allanite and calcite were separated using standard techniques. Apatite was analysed for U and Pb isotopes using ICP-MS.

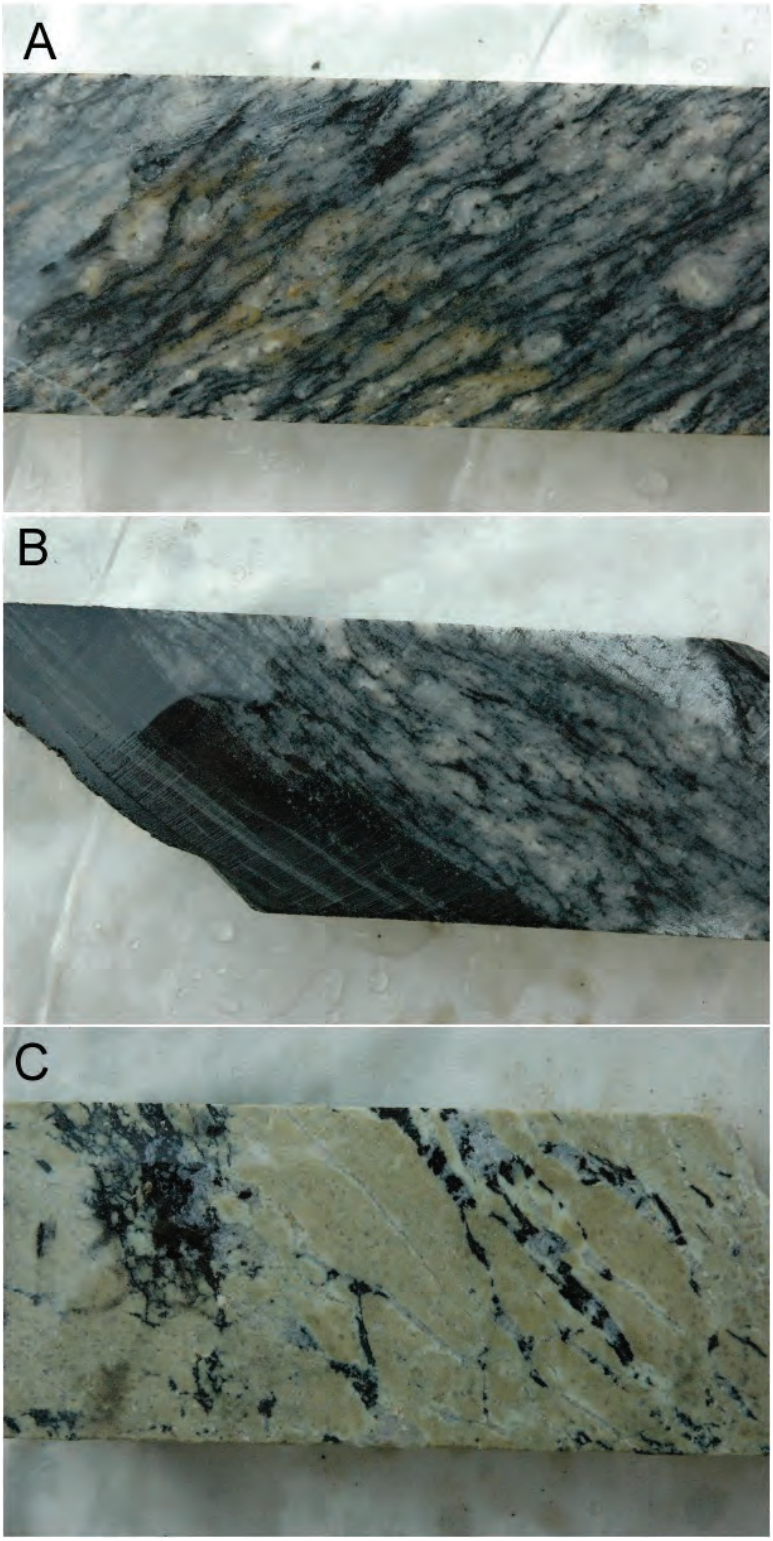

Figure 3.3: *Photographs of samples analysed in this study: (A) 2007080001-10; (B) 2007080001-11; and (C) 2007080001-25.*

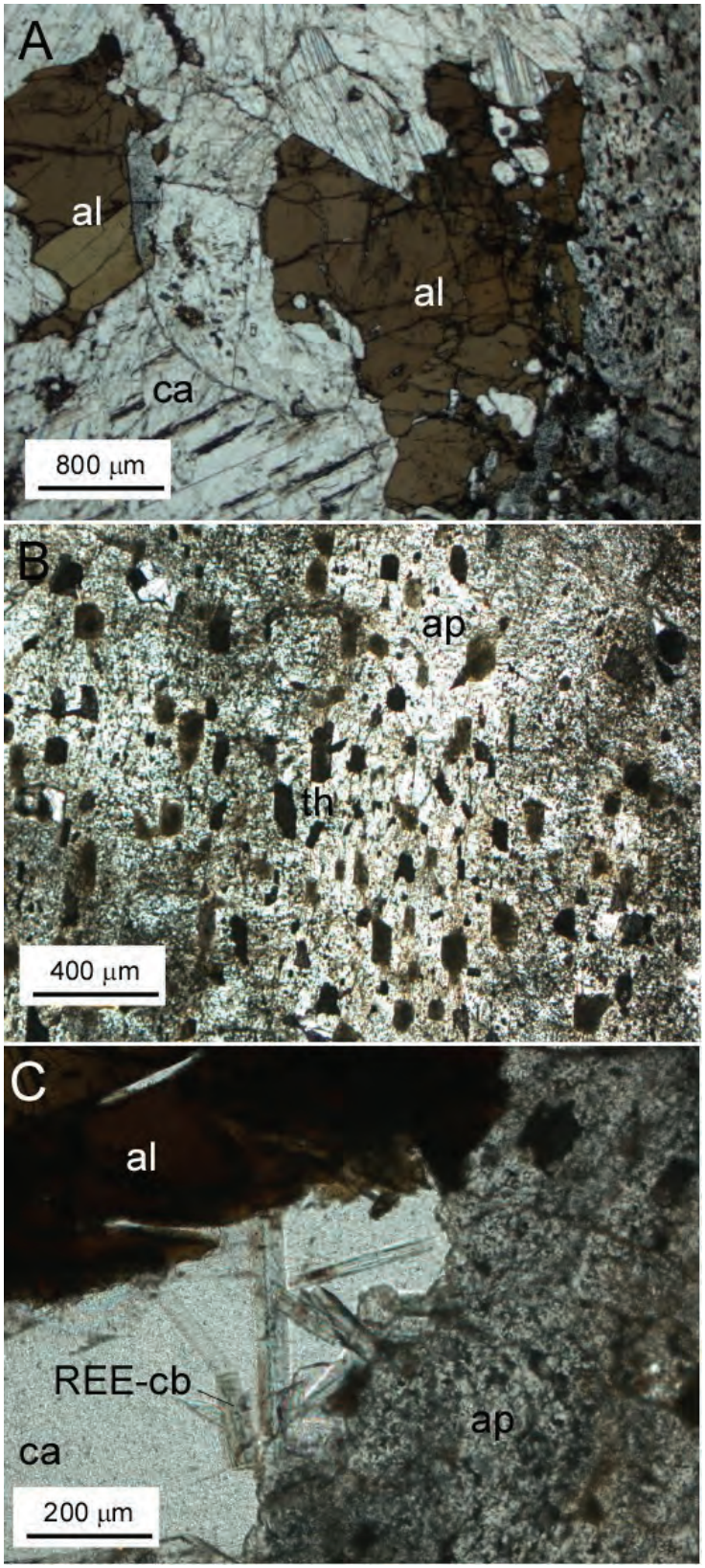

Figure 3.4: *Photomicrographs showing textural relationships in sample 2007080001-25: (A) calcite (ca)-allanite (al) vein cutting apatite; (B) apatite with abundant inclusions of thorite and REE-bearing minerals (th); and (C) REE-bearing carbonates (REE-cb) associated with calcite.*

3.4 U-Pb ISOTOPE ANALYSES OF VEIN APATITE

Being the dominant mineral and a significant REE repository at Nolans Bore, apatite was separated from sample 2007080001-25 and analysed for U-Pb, Sm-Nd and Sr isotopes. As presented below, the U-Pb results yield consistent and interpretable age data whereas the Sm-Nd isotope results could not be used for age dating, due to the low and uniform Sm/Nd ratios in this apatite. The Sm-Nd and Sr data, which have implications for the origin of the apatite veins, will be reported at a later date.

3.4.1 Results and discussion

U-Pb isotopic analyses were carried out by multi-collector ICPMS at the University of Melbourne following the methods described in Chapter 2. An additional Pb purification step was required to remove the unusually large amounts of LREE which produce polyatomic interference on the Pb spectrum in the ICP-mass spectrometer. Complete results are tabulated in Appendix 1. Radiogenic Pb/U ratios, calculated after common Pb correction with a 1200 Ma Pb from the Stacey-Kramers growth curve, yield a well-fitted discordia array in the Wetherill diagram (Fig. 3.5). The upper intercept of this discordia line yields an age of 1244 ± 10 Ma (2σ). This upper intercept is insensitive to the choice of common Pb and is tentatively interpreted as the age of mineralisation. The lower intercept is within error of 0 Ma, indicating modern radiogenic Pb loss, possibly related to weathering.

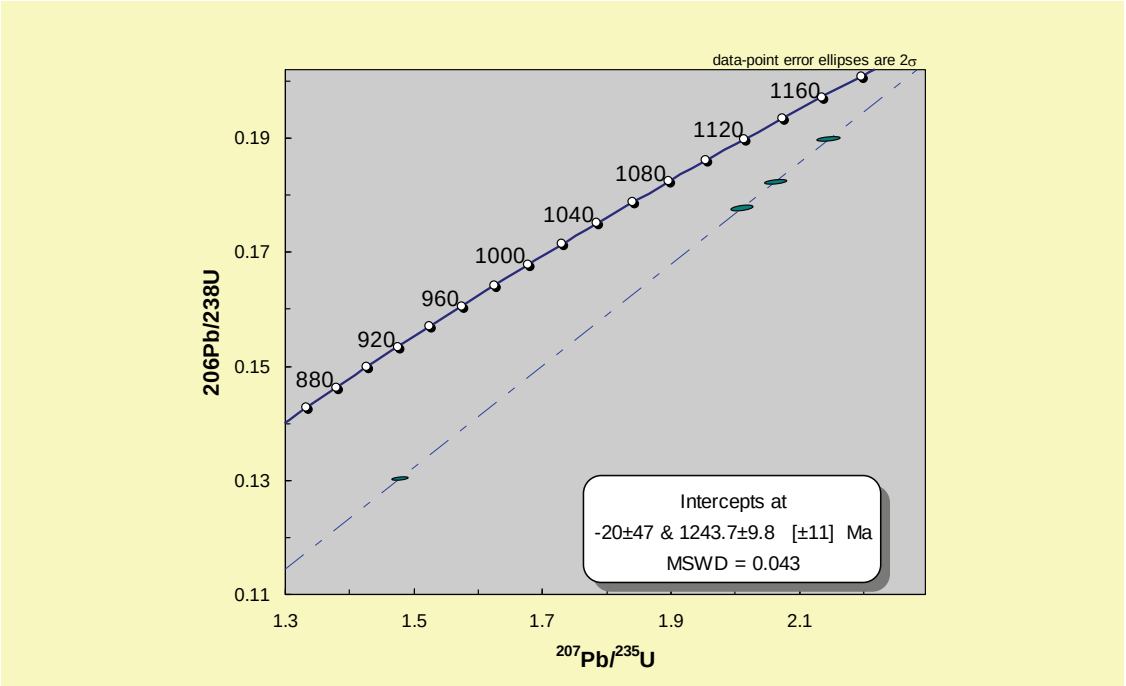

Figure 3.5: *Wetherill concordia diagram showing discordia established by apatite separates from sample 2007080001-25.*

3.5 ^{40}AR-^{39}AR ISOTOPE ANALYSIS OF MICA FROM WALL ROCK AND MYLONITES

Mica minerals, particularly biotite, commonly define a well developed fabric within the granite gneiss that forms the wall rock to the Nolans Bore apatite veins, and, in places, biotite-rich mylonites form discrete bands within the wall rocks. Although relationships between these mylonites and the apatite veins were not observed in drill core or at surface, the timing of the development of this fabric and the mylonites has important implications with respect to regional deformation.

3.5.1 Results

Step-heating analyses were conducted on three mineral separates, from two different rock samples, with each mineral separate being analysed in two separate aliquots, giving a total of six results. Results are summarised in Table 3-2 and presented diagrammatically in Figure 3.6. Complete analytical data are presented in Appendix 2.

Table 3.2: Summary of $^{40}Ar/^{39}Ar$ geochronology results from the Nolans Bore mylonites.

Sample	Mineral	Aliquot	Age[1] (Ma)	Uncertainty (2σ) (Ma)[2]
2007080001-10	Biotite	1	377.4	1.6
		2	374.4	1.6
2007080001-11	Biotite	1	368.1	1.6
		2	366.3	1.8
2007080001-11	Muscovite	1	344.8	1.6
		2	345.8	1.6

Notes: [1]ages are "plateau" ages. [2]uncertainties include 0.16% 1σ uncertainty on the J-parameter, but do NOT include uncertainty in the age of the reference material (Fish Canyon Sanidine, age 28.201 ± 0.046 Ma, Kuiper et al., 2008), or uncertainty in decay constants.

3.5.2 Discussion

Each of the six step-heating experiments yielded a statistically acceptable "plateau age" (Fig. 3.6) and different aliquots of each mineral separate yielded mutually consistent plateau ages, providing confidence that the apparent ages are geologically meaningful. Biotite from the host granitic gneiss (2007080001-10) yielded plateau ages of ~375 Ma. Biotite from the mylonitic band (2007080001-11) yielded plateau ages of ~367 Ma, whereas muscovite from the mylonitic band (2007080001-11) yielded plateau ages of ~345 Ma (Table 3-2, Fig. 3-6).

All of the mica ages are Paleozoic (Devonian to Carboniferous), although the host Boothby orthogneiss has a Paleoproterozoic U-Pb zircon crystallisation age of ~1806 Ma (Worden et al., 2008). These Paleozoic argon ages may represent either thermal resetting of Proterozoic mica or Paleozoic new mica mineral growth, or a combination of both.

The preservation of older ages in biotite (~375 Ma and ~367 Ma) relative to muscovite (~345 Ma) suggests muscovite growth took place at temperatures below the closure temperature for biotite (~300°C), and, therefore, also below the closure temperature for muscovite (~350 – 400°C). The muscovite age, therefore, likely represents the timing of muscovite growth rather than a cooling age. The presence of muscovite only within the mylonitic band and not in the host gneiss suggests muscovite has grown as a consequence of mylonitic deformation.

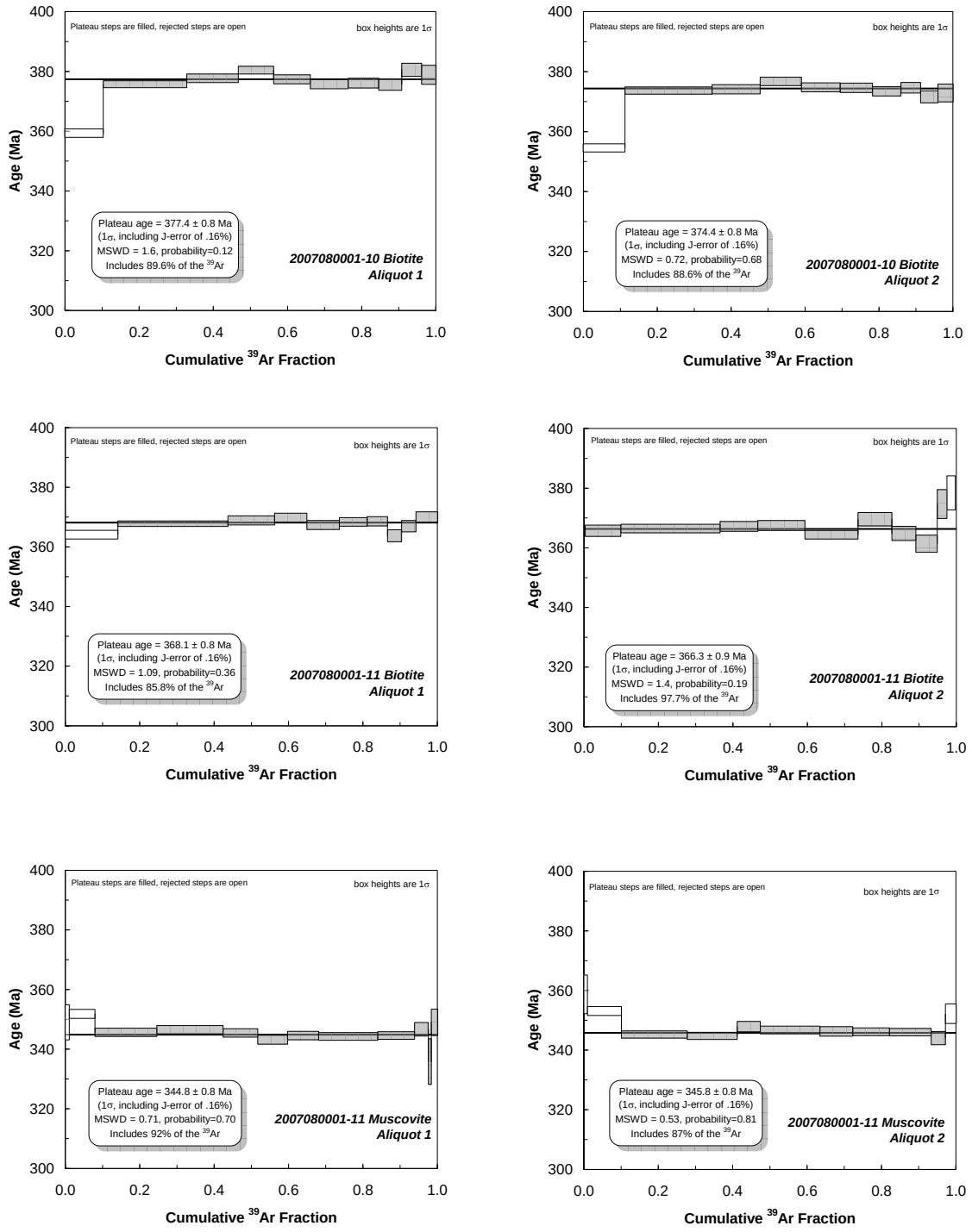

Figure 3.6: *$^{40}Ar/^{39}Ar$ age spectra from the samples discussed in the text.*

The muscovite age of ~345 Ma is, therefore, interpreted as the best estimate for the timing of mylonitic deformation at this locality. We note that this age for mylonitic deformation is broadly similar to the age of ~333 Ma reported by Cartwright et al. (1999), and interpreted by those authors as the timing of shear-fabric development at Sandy Creek in the Reynolds Range, approximately 20 km west of the Nolans Bore deposit.

The geological meaning of the biotite ages of ~367 Ma and 375 Ma is less clear. The preferred interpretation is that these ages represent regional cooling through a temperature of ~300°C. This period of cooling may have been a consequence of regional deformation and exhumation, or it may have occurred simply due to conductive cooling after an earlier thermal event. The data presented here cannot distinguish between these possibilities. The preservation of biotite ages within the mylonitic band that predate muscovite growth suggests that much of the biotite in these mylonite bands may be pre-existing biotite from the granitic gneiss rather than biotite that was newly-formed during shearing.

3.6 IMPLICATIONS OF THE ISOTOPIC DATA FOR THE TIMING OF REE-U-Th-P MINERALISATION AND DEFORMATION

Based on the U-Pb data for apatite, we infer a minimum age of ~1244 Ma for the emplacement of the apatite veins. However, until confirmed by other data (analyses currently in progress), we consider this age as tentative. The implications of the $^{40}Ar/^{39}Ar$ age results for timing of rare earth element mineralisation at the Nolans Bore deposit are not immediately obvious, and depend on the timing relationships of the mineralising event relative to deformation and mylonitisation.

The minimum ~1244 Ma age of mineralisation is younger than the high-grade metamorphic fabrics in the host rocks (attributed to the ~1590 Ma Chewings Orogeny) which are cut by the ore veins, providing first order qualitative support for the U-Pb apatite age. This age is broadly similar to the ages of (i) lamproite at the Argyle diamond mine in the Kimberley Province of Western Australia (~1178 Ma: Pidgeon et al., 1989), (ii) the Mudginberri phonolite dyke in the Pine Creek Orogen (Page et al., 1980), and (iii) a period of global carbonatite magmatism between 1300 and 1130 Ma (Pidgeon et al., 1989; Jaques, 2008). It also corresponds to ages of 1233 ± 65 Ma (whole rock Sm-Nd: Zhang et al., 1994) and 1208 ± 12 Ma ($^{40}Ar/^{39}Ar$: Ren et al., 1994) reported for carbonatite dikes associated with the Bayan Obo deposit in China (Smith and Wu, 2000).

The $^{40}Ar/^{39}Ar$ age results are best interpreted to reflect cooling of biotite through 300°C by ~367 Ma, and growth of new muscovite at ~345 Ma. Scrimgeour and Raith (2001) recorded $^{40}Ar/^{39}Ar$ ages of 365-360 Ma from muscovite the Delny-Mount Sainthill shear zones, which they interpreted to indicate movement along this shear zone during the Pertnjara Movement of the Alice Springs Orgeny. A possible interpretation of the new biotite data for Nolans Bore is that they record cooling associated with this event.

The growth of new muscovite at ~345 Ma does not correspond directly to any of the documented deformational events during the Alice Springs Orogeny. It is significantly younger than the Pertnjara Movement, but slightly older than the 340-320 Ma (Bendall et al., 1998; Cartwright et al., 1999) Mount Eclipse Movement. As the $^{40}Ar/^{39}Ar$ data record new muscovite growth following closure of biotite at ~367 Ma, the simplest interpretation is that the ~345 Ma age reflects early stages of the Mount Eclipse Movement. In any case, this deformation likely post-dated mineralisation.

3.7 SUMMARY AND CONCLUSIONS

Uranium-lead isotopic data for apatite separates from the Nolans Bore REE-U-Th-P deposit indicate a tentative minimum age for mineralisation of 1244 ± 10 Ma. This age, which will be further tested using other methods, falls within a broad period of global alkalic magmatism, ranging from 1300 to 1130 Ma. $^{40}Ar/^{39}Ar$ data from shear-related biotite and muscovite indicate a biotite cooling event at ~367 Ma and growth of new muscovite at ~345 Ma. These events may correspond to the 365-360 Ma Pertnjara and 340-320 Ma Mount Eclipse Movements of the Alice Springs Orogeny, respectively.

4. Kintyre U deposit, Western Australia

Andrew Cross[1], Subhash Jaireth[1] and Robert Rapp[2]

4.1 KINTYRE U DEPOSIT AND GEOLOGICAL SETTING

The Kintyre unconformity-related uranium deposit is located in the Paterson Orogen, Western Australia. It is hosted by Paleo- to Mesoproterozoic carbonaceous metasediments of the Yandagooge Formation adjacent to the unconformity with the Neoproterozoic Coolbro Sandstone of the Yeneena Basin (Mckay and Miezitis, 2001). The mineralised veins tend to be concentrated in the hinges of folds and have an orientation sub-parallel to the axial planes (Fig. 4.1).

The veins are dominated by a chlorite-carbonate assemblage, with carbonate minerals including dolomite, ankerite and calcite. Colloform pitchblende is the dominant ore mineral, with minor bismuthinite, chalcopyrite, bornite and galena, and trace native bismuth and gold. Platinum group elements have also been noted with gold, which has a geochemical association with copper and bismuth (Jackson and Andrew, 1990).

Geochronological data constrain deposition of sediments in the Yeneena Basin to between ~910 Ma, the age of the youngest detrital zircon in the basal Coolbro Formation (Bagas and Nelson, 2007), and ~830 Ma, the age of intermediate to mafic rocks that intrude the lower part of the basin (D. Maidment, unpublished data). These constraints are compatible with a Pb-Pb isochron age for carbonate rocks of the Isdell Formation of ~860 Ma (R. Maas & D.L. Huston, unpublished data), interpreted as a diagenetic age.

Unlike other well-known unconformity-related deposits in the Pine Creek Orogen and the Athabasca Basin in Canada, the Yeneena Basin sediments overlying the unconformity, and the unconformity surface, were deformed and folded during the Paterson Orogeny (~650 Ma), which also affected the orebody.

4.2 SAMPLES

Twenty-six EPMA analyses were carried out on the uraninite standard U6897. With the removal of one slightly younger analysis, the remaining 25 all have the same chemical U-Th-Pb age within their analytical uncertainties and combine to give an age of 1034 ± 10 Ma (MSWD = 1.4; 95% confidence), which is within uncertainty of its reference ID-TIMS U-Pb age.

The uraninite grains from Kintyre range in size between ~70 and ~120 µm in diameter and appear to be fragments of larger crystals. All are intensely cracked and speckled with numerous sulphide inclusions and veins (Fig. 4.2). The poor surface texture of these grains meant that the EPMA analytical spot inevitably overlapped onto some of the cracks and sulphide inclusions.

[1] Geoscience Australia, GPO Box 378, Canberra, ACT, Australia 2601
[2] Research School of Earth Sciences, The Australian National University, Canberra, ACT 0200

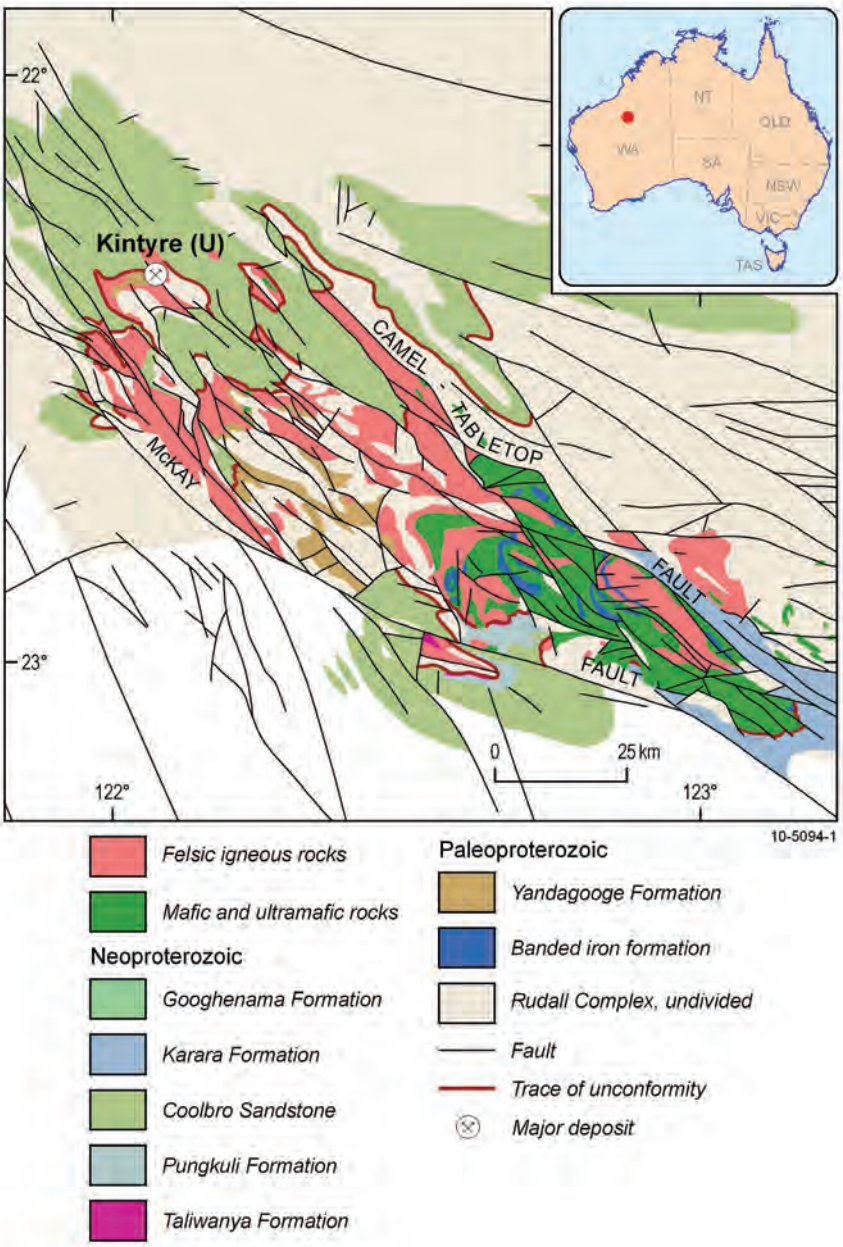

Figure 4.1: *Location of the Kintyre uranium deposit, Paterson Province, Western Australia.*

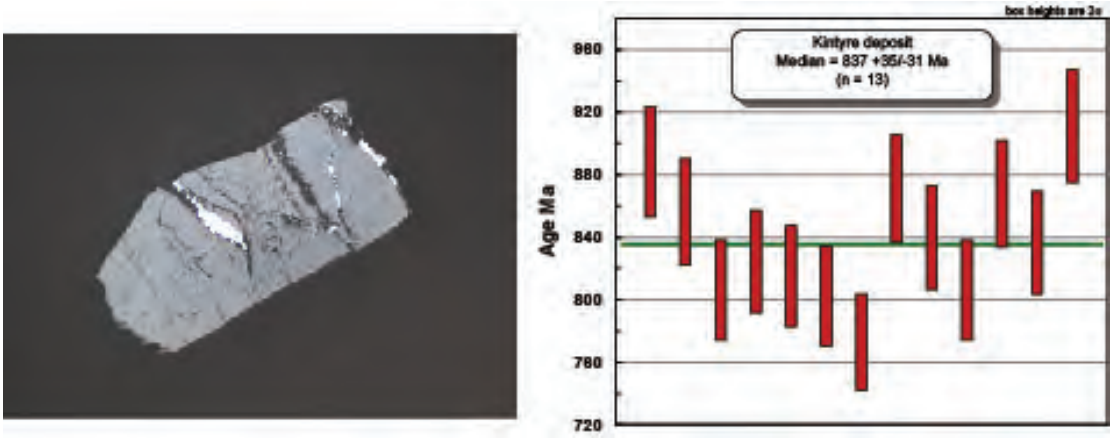

Figure 4.2: *Left - Uraninite grain (grey) with galena (white) in fractures, from the Kintyre deposit (reflected light. Right - U-Th-Pb ages from EPMA dating of the uraninite (from Cross et al., in review).*

4.3 DATING RESULTS

Nineteen EPMA analyses were undertaken and of these, six were removed as they either have low totals and high SiO_2 concentrations or overlapped onto sulphide inclusions. The remaining 13 analyses range from (in wt%): ~71.1 to 84.8% UO_2, <0.01% ThO_2 and 8.6 to 10.8% PbO. The chemical U-Th-Pb ages for these grains are however, scattered beyond their analytical uncertainties (MSWD = 5.5). However, a robust median age calculation, which is insensitive to outliers, gives an age of 837 +35/-31 Ma. Full EPMA results for uraninite from Kintyre, U6897 and also the Rössing South prospect (not reported here) are fully reported in Cross et al. (in review).

4.4 INTERPRETATION OF RESULTS

The chemical U-Th-Pb uraninite age of ~840 Ma reported here for the Kintyre deposit represents a good reconnaissance level radiometric determination for this deposit. Importantly, an age of 840 ± 10 Ma age determined from pitchblende grains from the same deposit by Maas and Bagas (in preparation) is well within error of the EPMA age. Additionally, the chemical U-Th-Pb uraninite age for the uraninite standard U6897 is well within error of its reference age, adding confidence to the EPMA chemical U-Th-Pb dating technique used.

Ages of ~840 to ~830 Ma for the Kintyre deposit and of ~815 Ma for the Nifty deposit (Huston et al., 2007; 2009) suggest mineralisation occurred during or soon after the latest period of sedimentation in the Yeneena Basin, probably during the ~850 to ~800 Ma Miles Orogeny.

5. Oasis U deposit, Queensland

David Huston[1], Geoff Fraser[1], Andrew Cross[1] and Natalie Kositcin[1]

5.1 GEOLOGICAL SETTING

The Oasis deposit is located 20 km to the northwest of The Lynd in northeastern Queensland. It is hosted by the Mesoproterozoic Mywyn Granite, which intrudes Paleo- to Mesoproterozoic metasedimentary rocks of the Etheridge Province (Fig. 5.1). The Proterozoic rocks are overlain unconformably by Phanerozoic successions, including Devonian siliciclastic rocks and Permo-Carboniferous volcanic rocks. The Proterozoic and Phanerozoic rocks are intruded by a series of Silurian-Devonian and Permo-Carboniferous granites.

5.2 OASIS U DEPOSIT

The Oasis deposit is located several kilometres to the west of the Lynd Mylonite Zone, which marks the eastern exposed margin of the Etheridge Province. The following description is based on the Mega Uranium website (www.megauranium.com), the Glengarry Resources website (www.glengarry.com.au), discussion with Mega Uranium geologists, observations from a site visit by some of the authors (August 2007), and analytical results on samples collected from that visit.

The deposit is hosted by a north-trending, moderately to steeply west-dipping shear zone (Fig. 5.2) that cuts the Mesoproterozoic Mywyn Granite. This granite consists of a foliated, feldspar porphyritic biotite granite. The mineralised zone is tabular and up to 15 m thick (mostly < 10 m) that has been traced 300 m along strike and is up to 175 m in depth (Fig. 5.2). Typical grades for this zone are between 0.12 and 0.17% U_3O_8. The uranium is hosted by mylonitic biotite-quartz schist, with the main uranium mineral being uraninite which occurs with biotite. At surface, a strong, north-trending fabric is present that dips 60-70° to the west; shear sense indicators indicate reverse motion with west side up.

[1] Geoscience Australia, GPO Box 378, Canberra, ACT, Australia 2601

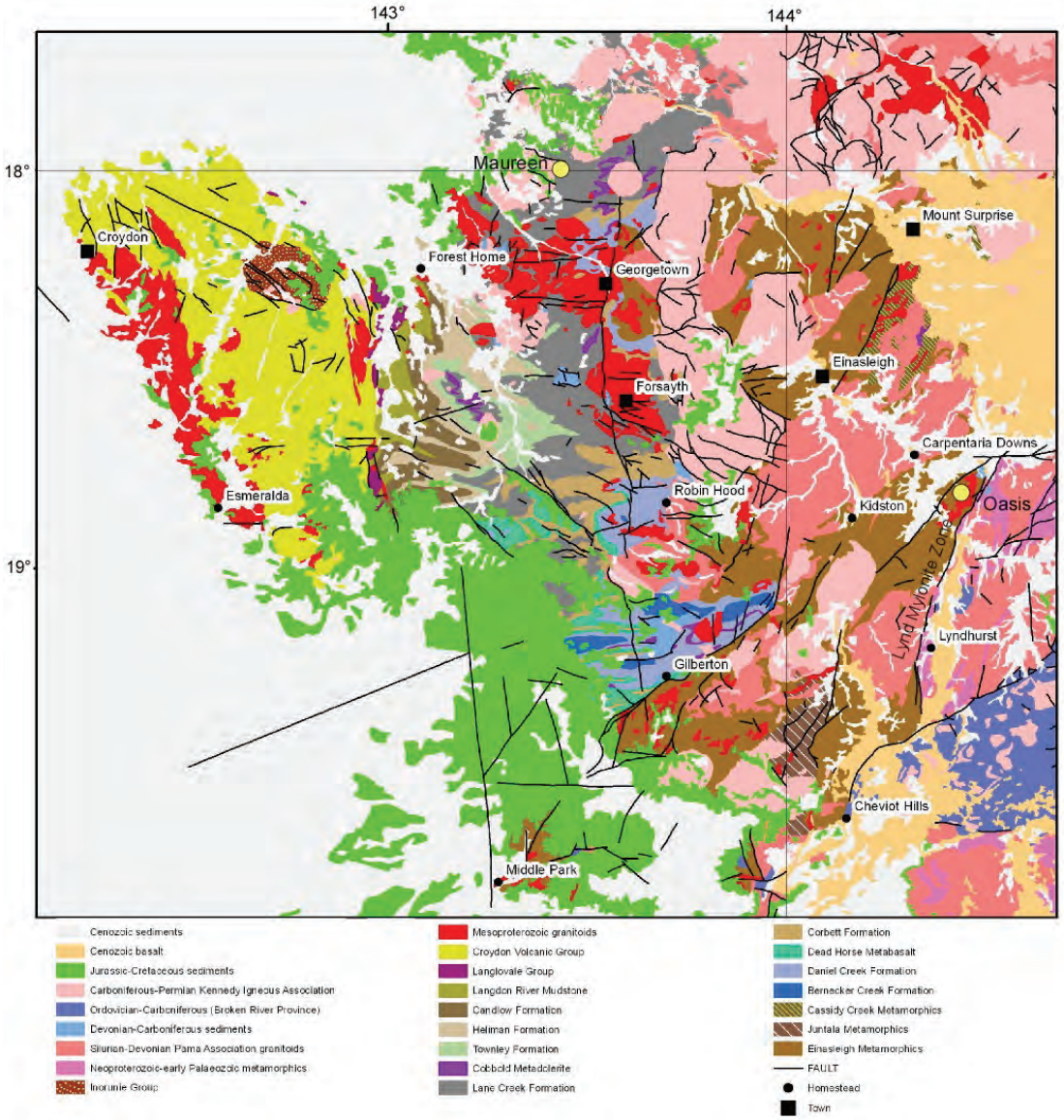

Figure 5.1: *Geology of the Georgetown region showing the location of the Oasis and Maureen uranium deposits (yellow filled circles). Modified after regional map provided by Ian Withnall, Geological Survey of Queensland.*

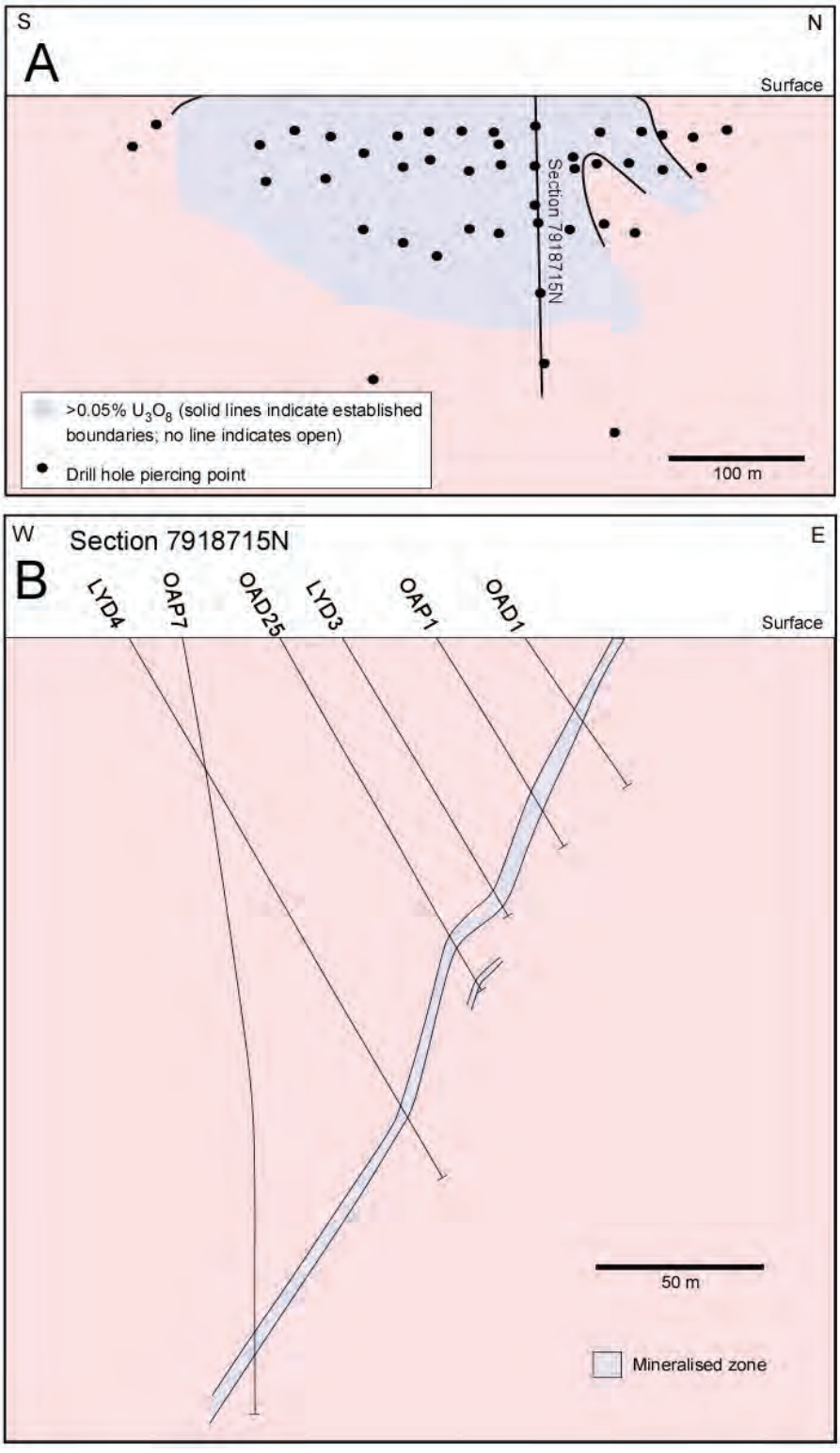

Figure 5.2: *Diagrams showing (A) long and (B) cross sections of the Oasis deposit and uranium mineralised zones (modified after Richards, 2006).*

5.3 SAMPLE DESCRIPTIONS AND U-REE PETROLOGY

Samples for this study were collected from diamond drill holes LDY001, LDY002 and 06LDY003, which all passed through the Mywyn Granite and the mylonitic biotite-quartz schist that hosts uranium mineralisation. Table 5-1 summarises the characteristics of each sample analysed in this study.

Samples 2007167005-03 and 2007167006-04 were examined using both optical and scanning electron microscopy. The dominant uranium mineral is uraninite, which occurs as individual grains (1-20 μm; Fig. 5.3A) disseminated along the foliation defined by biotite or as aggregates (Fig 5.3B). In detail, however, the uraninite overprints and, in many cases (e.g., Fig. 5.3C), replaces biotite and, to a lesser extent, muscovite along cleavage planes. The uraninite is commonly accompanied by coffinite, which typically replaces biotite, and which itself is commonly altered to chlorite along cleavage planes (Fig. 5.3D).

Other hydrothermal minerals present in the shear zone include thorite, a second unidentified thorium silicate with Th:Si of ~2, epidote group minerals (mostly allanite; Fig. 5.3E), apatite, a Ca-REE fluorocarbonate mineral, a Ca-REE fluoride mineral, pyrite (Fig. 5.3E), and hematite (Fig. 5.3B). Energy dispersive electron probe analyses indicate that the REE-bearing minerals can contain percent-level uranium. In addition, pre-existing zircon was extensively corroded and replaced by hydrothermal zircon which locally contains uraninite inclusions (Fig. 5.3F).

5.4 ALTERATION GEOCHEMISTRY RESULTS

The mineralised shear zone at Oasis is flanked on both sides by a zone of albite-biotite altered granite that passes laterally into unaltered granite. As part of this study we undertook whole rock geochemical analysis (at Geoscience Australia) of a number of altered and unaltered granite samples. Figure 5.4 compares the most altered (2007167004-03) versus the least altered (2007167004-02) sample of granite. These samples were taken approximately ten metres apart within the same drill hole, and a gradient in alteration intensity was present between the two samples. Comparison of altered with unaltered granite indicates significant mobility of many elements (Fig. 5.4A), but, overall, suggest little net change to rock mass, as the ratios of generally immobile elements (e.g., Y, Zr, Nb and Hf) between the altered granite and adjacent unaltered granite are near unity, with a few important exceptions (e.g., Ti and Th).

The most important changes are significant enrichments in sodium and magnesium, which reflects the albite-biotite alteration mineral assemblage. The enrichments appear to have been at the expense of potassium and calcium, in particular. Other alkali metals (Rb and Cs) as well as alkali earth elements (Sr and Ba) have also been lost. A small net loss of total iron reflects the combination of a small increase in ferrous iron and a significant decrease in ferric iron. The former also reflects the albite-biotite alteration assemblage. Other significant losses include fluorine and vanadium, but bismuth was added. As mentioned above, there appears to have been significant gains in both titanium and thorium, and possibly a small gain of aluminium and a small loss in tantalum. In addition, light rare earth elements (lanthanum to europium) have been gained in the altered granite, possibly with a slight positive europium anomaly (Fig. 5.4B). The middle and heavy rare earth elements do not appear to have been mobilised during alteration. The combination of enrichments in thorium and light rare earth elements suggest a light-rare-earth-element-enriched mineral, such as monazite or allanite, may have been produced during alteration. Allanite has been identified within the uraniferous mylonitic biotite-quartz schist (see below).

The most significant change in relative terms is uranium, which increased in absolute terms from 3 to 34 ppm from least altered to albite-biotite-altered granite. Within the mylonite zone, the main

host to uranium is uraninite, with minor coffinite. Uranium is also present at significant levels in uranothorite and in unidentified Ca-REE fluorocarbonates and possible fluorides. These results suggest significant dispersion of uranium beyond the mineralised shear zone.

Table 5.1: Samples analysed from the Oasis deposit.

SAMPLE	LOCATION (HOLE, DEPTH)	DESCRIPTION	MINERAL SEPARATION AND ANALYTICAL METHODS
2007167004-01	LYD002, 11.6-12.5 m	Foliated, feldspar-porphyritic biotite granite with patchy (10-20% of sample) biotite-albite altered zones; minor weathering along joints.	Zircon was separated using standard techniques. Analysed using SHRIMP U-Pb
2007167004-02	LYD002, 12.5-13.2 m	Foliated, feldspar-porphyritic biotite granite; minor weathering along joints; least altered.	Whole rock geochemistry
2007167004-03	LYD002, 23.4-25.6 m	Foliated, biotite and albite(?) altered feldspar-porphyritic biotite granite ; minor weathering along joints.	Whole rock geochemistry
2007167005-03	LYD001, 61.7-61.8 m	Biotite-quartz schist with alternating biotite-rich and biotite-poor domains. Other accessory to minor minerals include quartz, oligoclase, orthoclase and muscovite. The quartz and feldspar are remnants from the original granite protolith, but now are largely mylonitised, with the feldspars commonly occurring as porphyroclasts that have been rotated into a mylonitic fabric defined by biotite. The muscovite largely is developed parallel to the biotite fabric, although in places it overgrowths this mylonitic fabric. The main ore mineral is uraninite, which, though grossly parallel to the fabric, in detail overgrows the fabric. Other trace minerals include coffinite, allanite, apatite, pyrite, hematite, complex Ca-REE fluorocarbonates, zircon and galena. This sample came from an interval that assayed 2500 ppm U.	Biotite and muscovite were separated using standard techniques and analysed using laser ^{40}Ar-^{39}Ar step-heating. Uraninite from thin sections was analysed for uranium, lead and other elements using WDS electron microprobe analysis.
2007167006-04	06LYD003, 93.7-93.9 m	Biotite schist with minor albite and muscovite. Biotite, which forms a well-defined fabric, constitutes over 95% of the sample. The fabric is folded and overgrown by muscovite. The main ore mineral is uraninite, which overgrows the fabric defined by biotite. Other trace minerals include coffinite, allanite, apatite, pyrite, hematite, complex Ca-REE fluorocarbonate and fluoride(?) minerals, zircon and galena. This sample came from an interval that assayed 2570 ppm U.	Biotite and muscovite were separated using standard techniques and analysed using laser ^{40}Ar-^{39}Ar step-heating. Uraninite from thin sections was analysed for uranium, lead and other elements using WDS electron microprobe analysis.

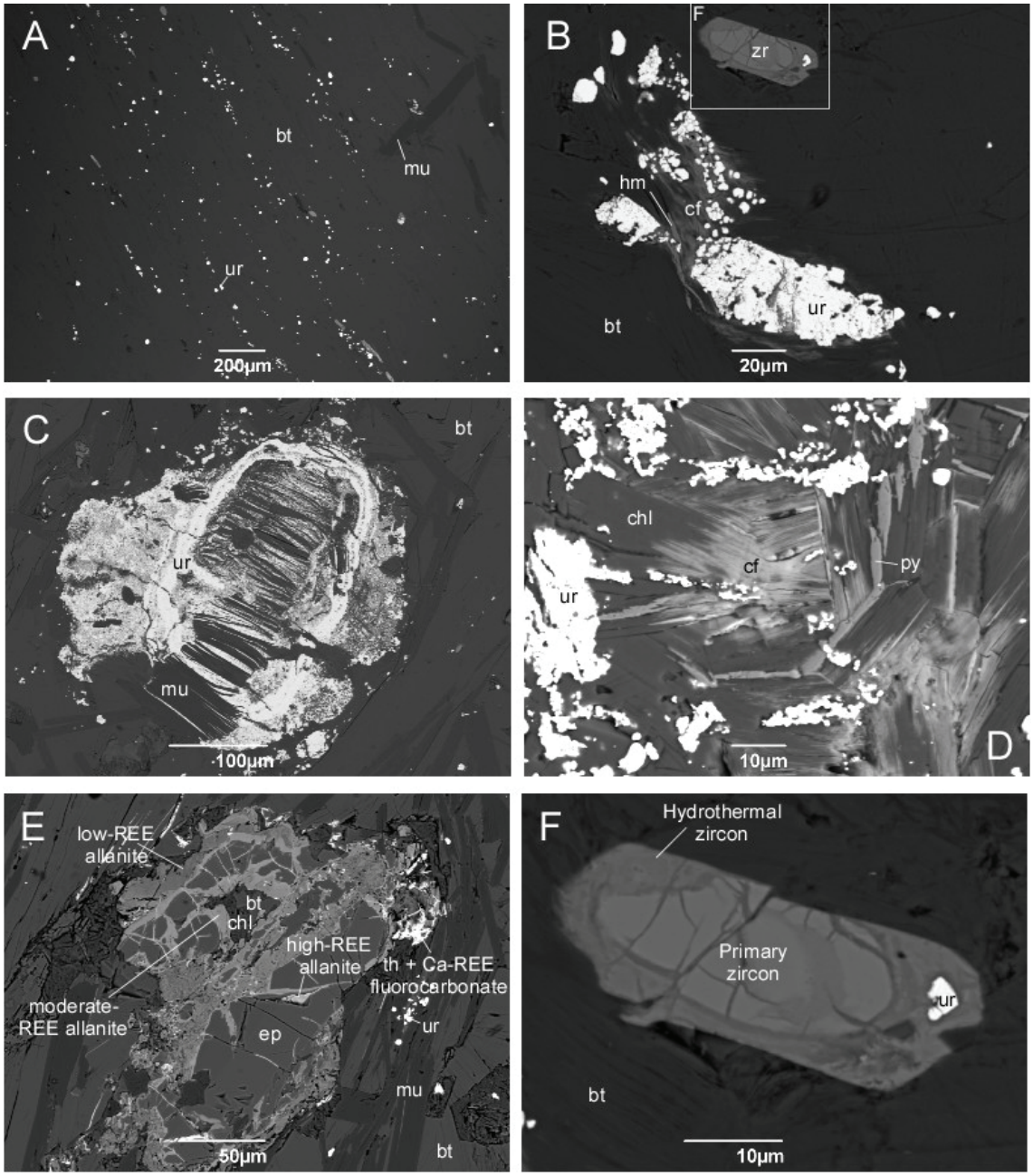

Figure 5.3: *Scanning electron microscope images showing textural relationships between minerals at the Oasis uranium deposit. (A) Uraninite (ur) grains along foliation defined by biotite (bt), which is overgrown by muscovite (mu). (B) Uraninite aggregate associated with coffinite (cf) and hematite (hm) that replace biotite (note zircon grain in upper centre, which is enlarged in 5.5F). (C) Uraninite replacing biotite and muscovite. (D) Coffinite and pyrite (py) replacing chlorite (chl) in association with uraninite. (E) Allanite replacing epidote (ep) in association with thorite (th) and Ca-REE fluorocarbonate. (F) Hydrothermal zircon overgrowing and replacing primary zircon. The hydrothermal overgrowth includes a uraninite grain.*

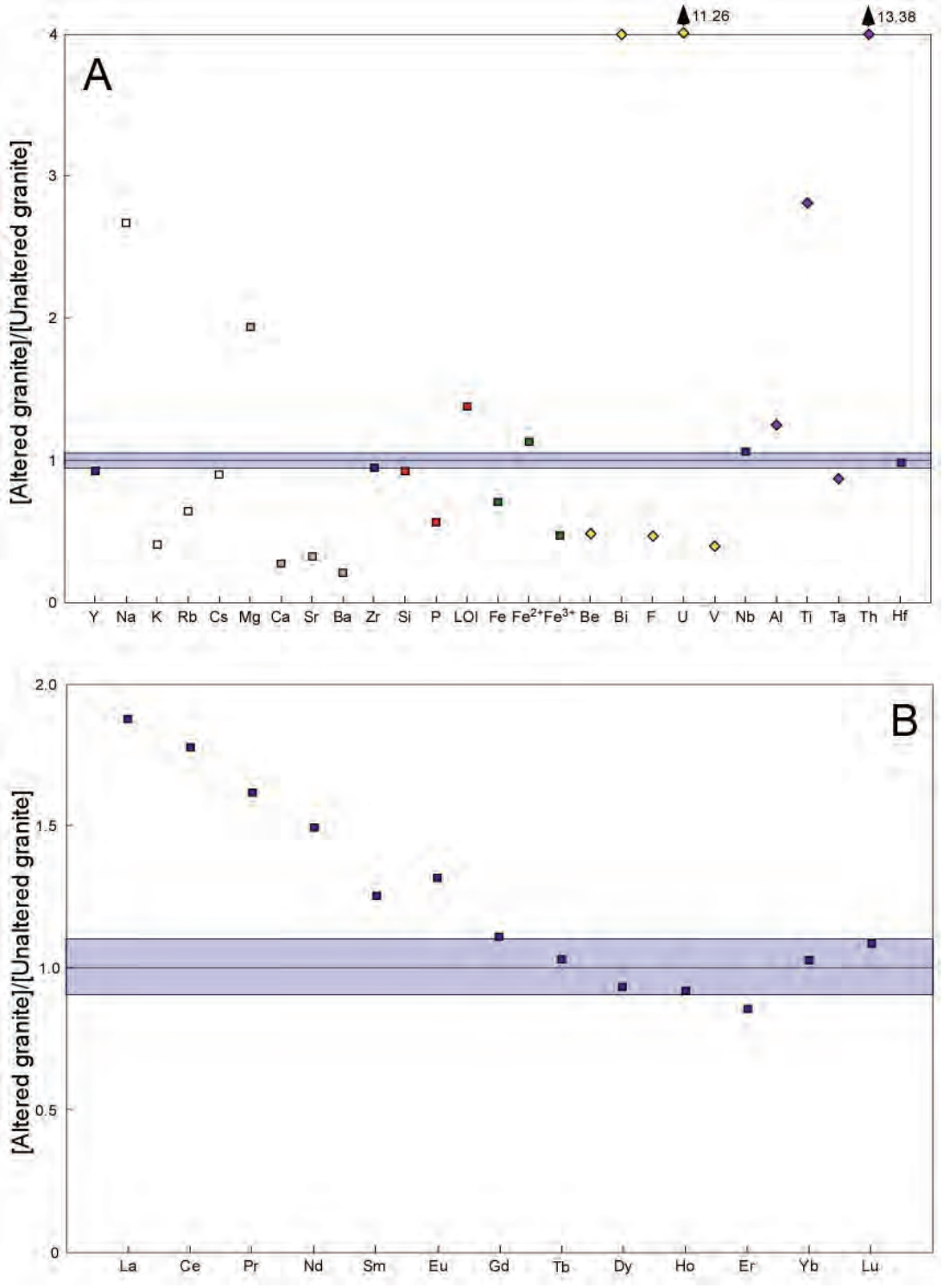

Figure 5.4: *Relative mass change diagrams showing the change in mass of albite-biotite altered granite (sample 2007167004-03) relative to least altered granite (sample 2007167004-02) at the Oasis uranium deposit: (A) major and selected trace elements; and (B) rare earth elements. The blue bands represent ±10% variation around unity, representing immobile behaviour.*

5.5 U-Pb ISOTOPE ANALYSES OF THE MYWYN GRANITE

To establish the age of the Mywyn Granite, and a maximum possible age of mineralisation, zircons were separated from sample 2007167004-01. A description of the separated zircons and the results of SHRIMP analysis of this sample are described separately by Neumann and Kositcin (in prep.). The data defined a discordia with an upper intercept of 1559 ± 3 Ma, which was interpreted as an igneous crystallisation age (Neumann and Kositcin, in prep.). A lower intercept of 582 ± 130 Ma was interpreted as an indication of Paleozoic isotopic disturbance.

5.6 ^{40}AR-^{39}AR ISOTOPE ANALYSIS OF MICA FROM MINERALISED MYLONITE ZONE

As described in Table 5.1 and shown in Figure 5.3, biotite defines the dominant fabric within the mylonitic biotite-quartz schist zone. Muscovite is present within the fabric, but also overprints it. The fabric is locally folded. As uranium minerals replace both biotite and muscovite the ages of these minerals define a maximum timing for mineralisation at the Oasis deposit.

5.6.1 Results

Figure 5.5 shows the results of laser step heating experiments of two aliquots each of four samples, for a total of eight analyses, from the mineralised shear. Results are summarised in Table 5-2. Complete analytical data are presented in Appendix 3.

Table 5.2: Summary of $^{40}Ar/^{39}Ar$ geochronology results from the Oasis uraniferous mylonitic biotite-quartz schist.

Sample	Mineral	Aliquot	Age[1] (Ma)	Uncertainty (2σ) (Ma)[2]
2007167005-03	Muscovite	1	N/A	N/A
		2	429.5	2.4
2007167005-03	Biotite	1	438.6	2.0
		2	439.0	1.9
2007167006-04	Muscovite	1	436.8	5.2
		2	435.8	2.6
2007167006-04	Biotite	1	434.0	2.0
		2	432.7	1.9

Notes: [1]ages are "plateau" ages. [2]uncertainties include 0.16% 1σ uncertainty on the J-parameter, but do not include uncertainty in the age of the reference material (Fish Canyon Sanidine, age 28.201 ± 0.046 Ma, Kuiper et al., 2008), or uncertainty in decay constants.

5.6.2 Discussion

With one exception, the step heating experiments yielded plateau ages of between 430 and 439 Ma. The exception yielded a pseudo-plateau age of 429 Ma, consistent with the age yielded by the second aliquot of the same sample. In each case the two aliquots of each sample yielded ages within 2σ uncertainty of each other (Table 5-2).

In sample 2007167005-03, biotite yielded an older age than muscovite (~439 Ma versus 429 Ma), consistent with the textural observation that some of the muscovite cross-cuts the mylonitic fabric defined by biotite. Preservation of biotite ages older than associated muscovite ages suggests late-stage muscovite growth took place at relatively low temperatures, not sufficient to isotopically reset the biotite. Muscovite growing at such temperatures is likely to preserve a crystallisation age rather than a cooling or closure age. The muscovite analysed from this rock is likely to have been a mixture between mylonitic muscovite and later-stage cross-cutting muscovite, and thus the age

of ~429 Ma from the muscovite is interpreted as a maximum age for this late-stage muscovite growth. The biotite ages of ~439 Ma might approximate the time of mylonitic deformation, but could also record post-deformational cooling and isotopic closure, and thus are conservatively interpreted as minimum ages for mylonitic deformation in this sample.

In sample 2007167006-04, muscovite and biotite yielded ages within uncertainty of each other, with the muscovite ages being, at face value, fractionally older than the biotite ages (~436 Ma versus ~434 Ma). This age relationship is at odds with the textural observation that muscovite overgrows the biotite fabric, and is more consistent with an interpretation that these ages represent cooling ages. Both the muscovite and biotite ages from this sample are, therefore, interpreted to represent minimum estimates for the timing of fabric-forming deformation in this rock, consistent with the minimum age estimate for mylonitic deformation obtained from sample 2007167005-03, as reported above.

In summary, the $^{40}Ar/^{39}Ar$ results from these samples are interpreted to provide a minimum age for mylonitic deformation of ~439 Ma, and an indication of a subsequent period of muscovite growth with a maximum age of ~429 Ma. Given the textural observation that uranium and related minerals replace biotite and, in some cases, muscovite, these mica ages are regarded as maximum ages for mineralisation.

5.7 CHEMICAL DATING OF URANINITE

Electron Probe Microanalysis (EPMA) chemical U-Th-Pb dating was carried out on uraninite from the Oasis uranium deposit to directly determine the age of uranium mineralisation (see Chapter 2 for details of analytical method). Sixty-three EPMA analyses were made on uraninite in two polished thin sections. Of these, 11 analyses were removed from further consideration as they either contained more than 1% FeO or have totals below 94% (Table 5.3). The remaining 52 analyses are however, slightly scattered beyond their analytical uncertainties (MSWD = 1.6). Without analytical grounds to reject any other analyses, we have used a robust median calculation (Ludwig, 2001) to estimate their age. This results in an age of 433.9 +3.4/-3.9 Ma (Fig. 5.6).

5.8 IMPLICATIONS OF THE ISOTOPIC DATA FOR THE TIMING OF THE EMPLACEMENT OF THE HOST GRANITE, MYLONITISATION AND MINERALISATION

As discussed by Neumann and Kositcin (in prep.), the Mywyn Granite, which hosts the Oasis deposit has a Mesoproterozoic emplacement age of ~1559 Ma, at least 1000 million years older than uranium mineralisation. The maximum age of uranium mineralisation is constrained between 440-430 Ma, the minimum age of mylonitic deformation and subsequent muscovite growth in the Oasis shear zone. This age is compatible with development during the Benambran deformational event, which has affected much of north Queensland, including the Camel Creek, Hodgkinson and Charters Towers regions (Champion et al., 2009). The minimum age of mineralisation is provided by the chemical age of ~433 Ma determined from wavelength dispersive electron microprobe analysis of uraninite. This age must be considered a minimum age as uraninite can be easily reset by later geological processes, although the consistency of the age result may support an interpretation that this age reflects the true age of mineralisation.

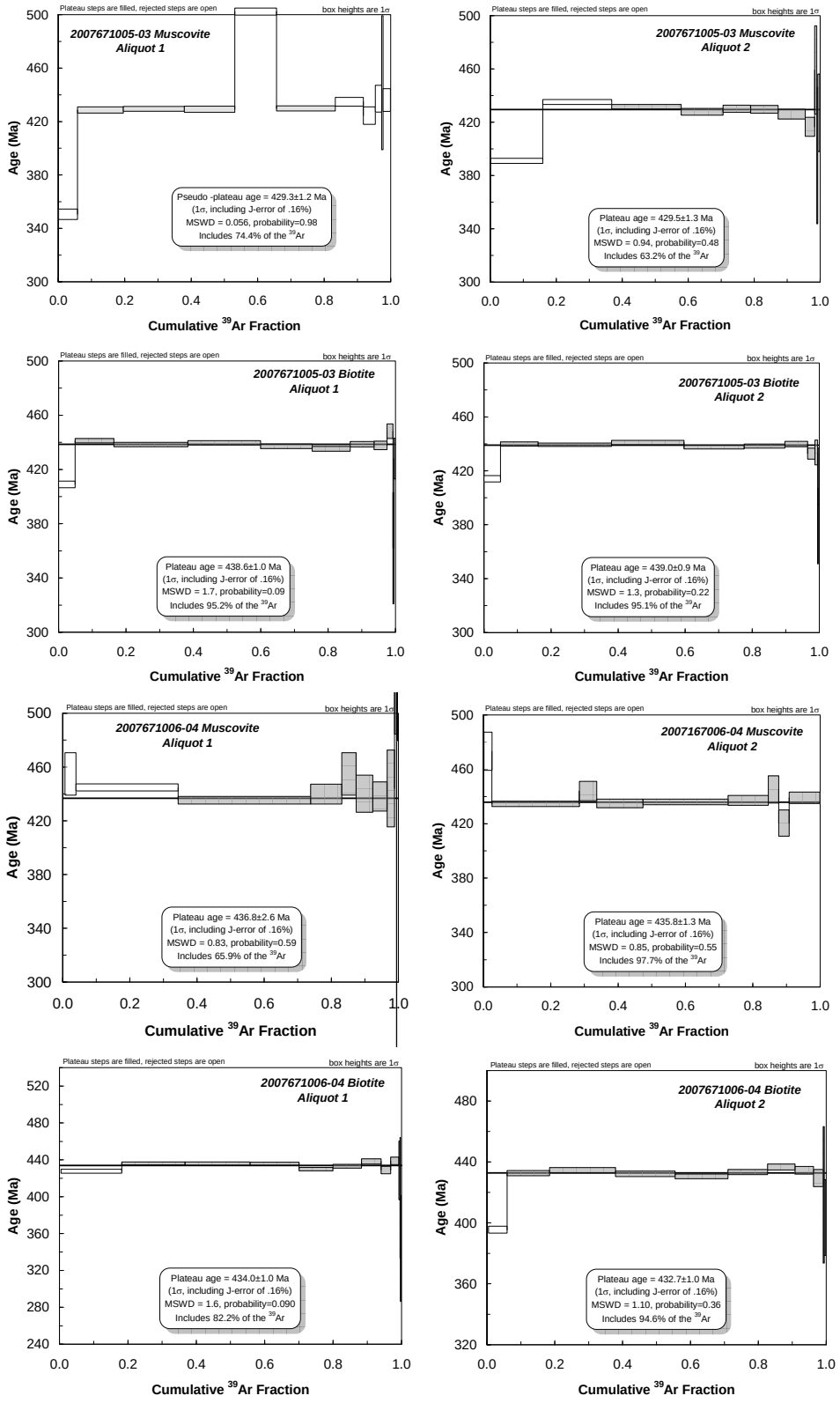

Figure 5.5: *$^{40}Ar/^{39}Ar$ age spectra for the samples discussed in the text, from the Oasis uranium deposit.*

Table 5.3: EPMA analyses and calculated chemical ages for uraninite from the Oasis deposit.

Grain.area	UO_2	ThO_2	PbO	SiO_2	CaO	Y_2O_3	FeO	TiO_2	total	Age (Ma)	± (2□)
oasis-a-uran-5	86.89	4.53	5.39	0.14	0.15	0.62	0.38	0.00	98.10	441.1	17.6
oasis-a-uran-6	91.78	0.06	5.70	0.06	0.37	0.56	0.63	0.00	99.16	448.5	18.0
oasis-a-uran-7	86.63	4.45	5.29	0.14	0.19	0.63	0.39	0.00	97.72	434.3	17.4
oasis-a-uran-8	91.95	0.35	5.68	0.05	0.29	0.57	0.60	0.00	99.50	445.7	17.8
oasis-a-uran-9	91.76	0.00	5.69	0.12	0.46	0.61	0.64	0.00	99.27	448.0	17.9
oasis-a-uran-11	90.77	1.82	5.61	0.56	0.20	0.66	0.88	0.00	100.49	443.6	17.7
oasis-a-uran-12	89.61	0.43	5.48	0.70	0.40	0.69	0.74	0.00	98.04	441.3	17.7
oasis-a-uran-13	90.31	1.45	5.48	0.14	0.25	0.64	0.72	0.00	98.99	436.3	17.5
oasis-a-uran-14	91.65	0.36	5.52	0.12	0.39	0.67	0.54	0.00	99.25	435.0	17.4
oasis-a-uran-17	87.25	0.29	5.15	0.36	0.21	0.52	1.00	0.00	94.77	426.6	17.1
oasis-a-uran-18	89.89	0.65	5.64	0.14	0.37	0.63	0.51	0.00	97.82	451.9	18.1
oasis-a-uran-19	91.98	0.41	5.72	0.04	0.35	0.53	0.44	0.00	99.47	448.1	17.9
oasis-a-uran-20	88.65	0.36	5.58	1.43	0.36	0.42	0.95	0.00	97.76	453.8	18.2
oasis-a-uran-21	89.89	1.47	5.47	0.10	0.29	0.79	0.46	0.00	98.47	438.0	17.5
oasis-a-uran-1.2	91.19	0.32	5.62	0.08	0.42	0.53	0.57	0.00	98.74	444.6	17.8
oasis-a-uran-22	89.91	0.01	5.36	0.07	0.35	0.59	0.63	0.00	96.92	431.1	17.3
oasis-a-uran-23	90.28	0.37	5.34	0.12	0.28	0.58	0.59	0.00	97.57	427.6	17.1
oasis-b-uran-1	88.91	0.00	5.07	0.30	0.64	0.37	0.23	0.04	95.56	413.1	16.5
oasis-b-uran-1.2	88.31	0.00	5.21	0.33	0.58	0.34	0.21	0.04	95.02	426.9	17.0
oasis-b-uran-3	90.66	0.30	5.45	0.12	0.39	0.55	0.57	0.00	98.04	433.9	17.4
oasis-b-uran-5	88.42	0.09	5.30	1.16	0.47	0.51	0.70	0.00	96.64	433.5	17.4
oasis-b-uran-6	89.62	0.51	5.42	0.57	0.24	0.51	0.51	0.00	97.38	436.1	17.5
oasis-b-uran-7	88.79	1.67	5.40	0.10	0.24	0.51	0.48	0.00	97.19	437.4	17.5
oasis-b-uran-8	88.72	0.00	5.25	0.34	0.67	0.34	0.16	0.13	95.61	427.9	17.1
oasis-b-uran-10	88.33	0.00	5.20	0.72	0.84	0.32	0.46	0.01	95.88	426.4	17.0
oasis-b-uran-11	89.06	0.00	5.23	0.38	0.78	0.34	0.12	0.08	96.00	424.9	16.9
oasis-b-uran-12	87.64	0.00	5.10	0.57	0.79	0.26	0.32	0.14	94.81	421.4	16.8
oasis-b-uran-13	87.20	0.00	5.05	1.08	0.54	0.36	0.61	0.11	94.96	419.3	16.7
oasis-b-uran-14	90.25	0.35	5.42	0.05	0.28	0.65	0.37	0.00	97.35	433.6	17.4
oasis-b-uran-15	90.04	0.24	5.54	0.06	0.31	0.48	0.33	0.00	97.00	444.0	17.8
oasis-b-uran-16	91.06	0.42	5.48	0.14	0.31	0.48	0.52	0.00	98.40	434.2	17.4
oasis-b-uran-17	89.72	0.10	5.40	0.09	0.36	0.60	0.61	0.00	96.88	434.9	17.4
oasis-b-uran-18	88.91	0.35	5.47	0.44	0.32	0.46	0.59	0.00	96.55	444.0	17.8
oasis-b-uran-20	85.88	0.00	4.88	1.46	0.67	0.32	1.08	0.09	94.38	412.1	16.5
oasis-b-uran-21	88.67	0.00	5.11	0.35	0.71	0.30	0.25	0.10	95.48	417.7	16.6
oasis-b-uran-22	90.70	0.01	5.44	0.18	0.34	0.43	0.55	0.00	97.63	433.5	17.3
oasis-b-uran-24	90.05	0.00	5.38	0.22	0.74	0.51	0.46	0.00	97.36	431.8	17.3
oasis-b-uran-25	89.25	0.00	5.30	0.16	0.74	0.31	0.07	0.04	95.88	430.1	17.1
oasis-b-uran-26	89.36	0.09	5.31	0.18	0.60	0.50	0.43	0.00	96.48	430.1	17.2
oasis-b-uran-28	90.84	0.00	5.07	0.21	0.86	0.27	0.16	0.00	97.40	404.8	16.1
oasis-b-uran-29	89.66	0.00	5.52	0.10	0.43	0.72	0.32	0.00	96.76	444.9	17.8
oasis-b-uran-30	87.28	0.00	5.03	1.08	0.69	0.29	0.76	0.06	95.20	417.4	16.6
oasis-b-uran-31	88.96	0.53	5.29	0.52	0.25	0.55	0.84	0.01	96.94	429.6	17.2
oasis-b-uran-32	89.47	0.00	5.33	0.33	0.77	0.34	0.08	0.06	96.36	431.2	17.2
oasis-b-uran-33	91.17	0.20	5.56	0.08	0.26	0.43	0.58	0.00	98.27	440.3	17.6
oasis-b-uran-34	89.69	0.00	5.22	0.31	0.77	0.31	0.06	0.01	96.37	421.2	16.8
oasis-b-uran-35	90.30	0.48	5.43	0.20	0.29	0.53	0.83	0.00	98.06	434.0	17.4
oasis-b-uran-37	86.32	0.00	4.96	1.04	0.62	0.33	0.64	0.17	94.06	416.5	16.6
oasis-b-uran-38	90.47	0.46	5.53	0.09	0.30	0.55	0.51	0.00	97.91	441.1	17.7
oasis-b-uran-39	89.72	0.00	5.33	0.16	0.84	0.29	0.08	0.02	96.46	430.0	17.1
oasis-a-uran-1.3	90.47	0.31	5.52	0.12	0.32	0.53	0.55	0.00	97.81	440.6	17.6
oasis-a-uran-5.2	84.91	4.49	5.27	0.16	0.16	0.65	0.41	0.00	96.05	440.9	17.6
rejected analyses											
oasis-a-uran-15	71.85	0.54	4.05	5.71	0.25	0.31	3.29	0.18	86.17	407.4	16.3
oasis-a-uran-16	83.74	0.08	4.85	0.81	0.38	0.42	0.87	0.01	91.15	419.1	16.8
oasis-b-uran-2	80.78	0.11	5.25	0.51	0.55	0.38	0.93	0.00	88.50	467.7	18.7
oasis-b-uran-4	87.27	0.12	5.00	0.19	0.39	0.39	0.49	0.00	93.84	415.0	16.6
oasis-b-uran-9	62.01	0.01	3.83	7.96	0.65	0.20	7.03	0.88	82.60	446.3	17.9
oasis-b-uran-19	81.15	0.00	4.64	2.67	0.81	0.27	2.03	0.17	91.74	414.0	16.5
oasis-b-uran-27	86.61	0.00	5.21	0.60	0.66	0.32	0.43	0.06	93.90	435.0	17.3
oasis-b-uran-36	84.48	0.00	4.72	0.35	0.60	0.33	0.17	0.10	90.77	405.5	16.1
oasis-a-uran-4	87.53	0.18	5.12	2.10	0.41	0.57	1.90	0.07	97.88	423.2	16.9
oasis-a-uran-10	84.08	0.74	5.01	3.49	0.25	0.53	2.16	0.06	96.33	430.2	17.2
oasis-b-uran-23	84.89	0.00	4.94	1.61	0.72	0.32	1.20	0.33	94.01	421.7	16.8

compositions reported in wt%

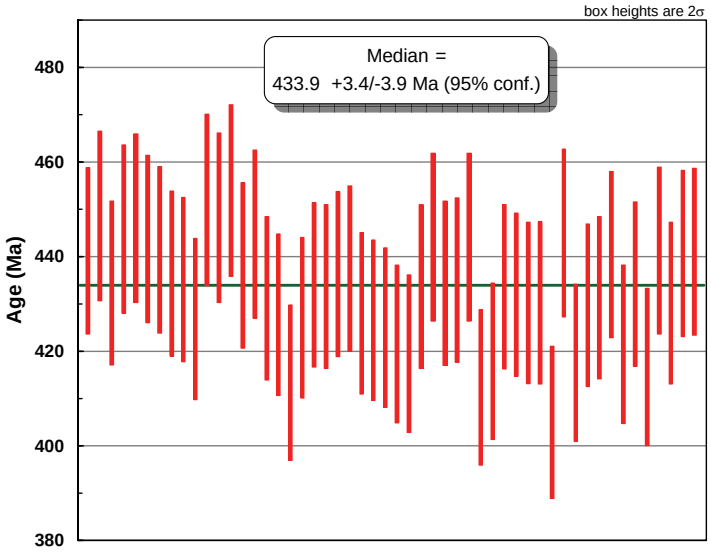

Figure 5.6: *Electron microprobe (EPMA) chemical U-Th-Pb ages for uraninite from the Oasis uranium deposit.*

6. Mt Gee-Armchair U-REE deposits, South Australia

Roger G. Skirrow[1], Robert Creaser[2], and Stephen B. Hore[3]

6.1 REGIONAL GEOLOGICAL SETTING

The Mt Gee and Armchair uranium deposits are situated in the Mt Painter Inlier, at the northeastern extremity of the Flinders Ranges of South Australia (Fig. 6.1). The Mt Painter Inlier forms the northwestern part of the Paleoproterozoic-Mesoproterozoic Curnamona Province, which includes the Willyama inliers. The Mt Painter Inlier comprises early Mesoproterozoic metasedimentary, felsic metavolcanic, and metagranitic units with SHRIMP U-Pb zircon ages of the igneous units between ~1600 Ma and ~1550 Ma (Fanning et al., 2003; Fraser and Neumann, 2010). There is evidence from zircon geochronology of a metamorphic event at ~1550 Ma (Fraser and Neumann, 2010). The early Mesoproterozoic A-type granites of this region are well known as some of the most uranium-rich igneous rocks in Australia (Neumann et al., 2000).

Early Mesoproterozoic rocks of the Mt Painter Inlier are unconformably overlain by Neoproterozoic sedimentary and minor mainly mafic volcanic sequences of the Adelaide Geosyncline (Fig. 6.1). The lower Paleozoic Arrowie Basin developed across the region with major depocentres to the east and west of the Adelaide Geosyncline. These basins and parts of the crystalline basement were in turn overlain by the Mesozoic Eromanga Basin and Cenozoic Lake Eyre Basin, the latter hosting the Beverley and Four Mile sandstone-type uranium deposits to the east of the Mt Painter Inlier (Fig. 6.1).

Early Mesoproterozoic rocks of the Mt Painter Inlier, and the Adelaide Geosyncline, were affected by the Delamerian Orogeny, which in the southern Adelaide Fold Belt has been constrained to ~515-490 Ma (Fig. 6.2; Foden et al., 1999). Peak metamorphic temperatures were at least 500ºC (McLaren et al., 2002). The timing of the metamorphic, deformational, and Paleozoic igneous events in the Mount Painter region has been debated in recent years. The available geological and geochronological data indicate that the Delamerian Orogeny resulted in large-scale folding, metamorphism and small volumes of pegmatite in the Mt Painter region (Fig. 6.2; Paul et al., 1999; Elburg et al., 2003). This was followed by a separate thermal event at ~440-460 Ma, including intrusion of a suite of leucogranites / pegmatites such as the S-type British Empire Granite (Elburg et al., 2003; McLaren et al., 2006), and relatively high temperature hydrothermal activity represented by diopside-titanite veins, dated at 439 ± 1 Ma (Elburg et al., 2003).

Three stages of cooling at ~430 Ma, ~400 Ma and ~330 Ma (Fig. 6.2) were attributed by McLaren et al. (2002) to exhumation during successive stages of the Alice Springs Orogeny. I-type granites intruding the Warburton Basin, which underlies the Cooper Basin in far northeast South Australia, have been dated at ~298 Ma to ~340 Ma (Gatehouse et al., 1995). These intrusions, which are significant for geothermal energy, may represent the effects of the final ‘movement’ of the Alice Springs Orogeny, or of the Kanimblan tectonic cycle of eastern Australia (Champion et al., 2009).

[1] Geoscience Australia, GPO Box 378, Canberra, ACT Australia 2601
[2] University of Alberta, Edmonton, Alberta, Canada T6G 2R3
[3] Primary Industries and Resources South Australia, Adelaide, South Australia

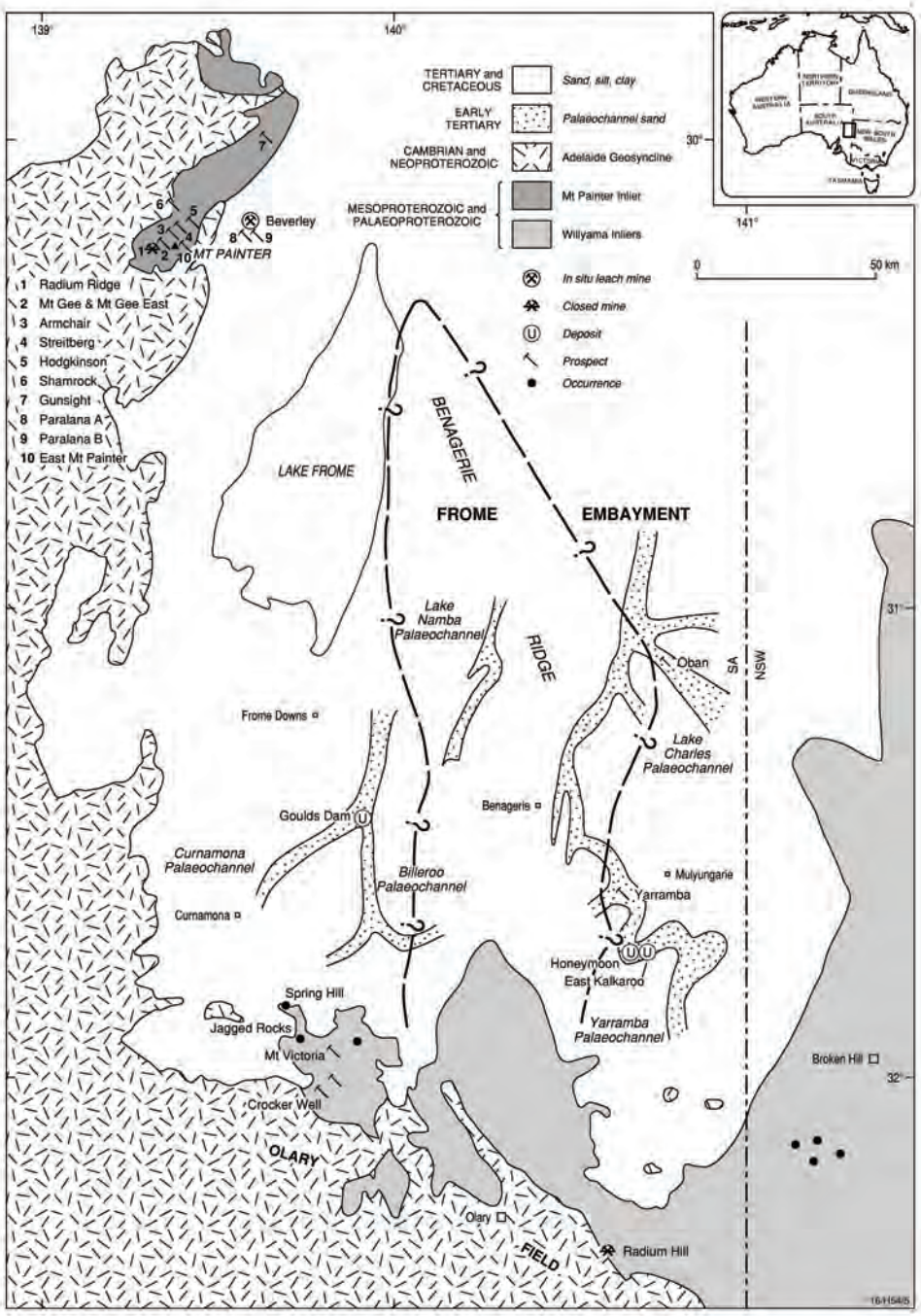

Figure 6.1: *Geological setting of the Mt Painter Inlier, and location of the Mt Gee and Armchair REE-U deposits in relation to other U deposits in the region. Source: McKay and Miezitis (2001).*

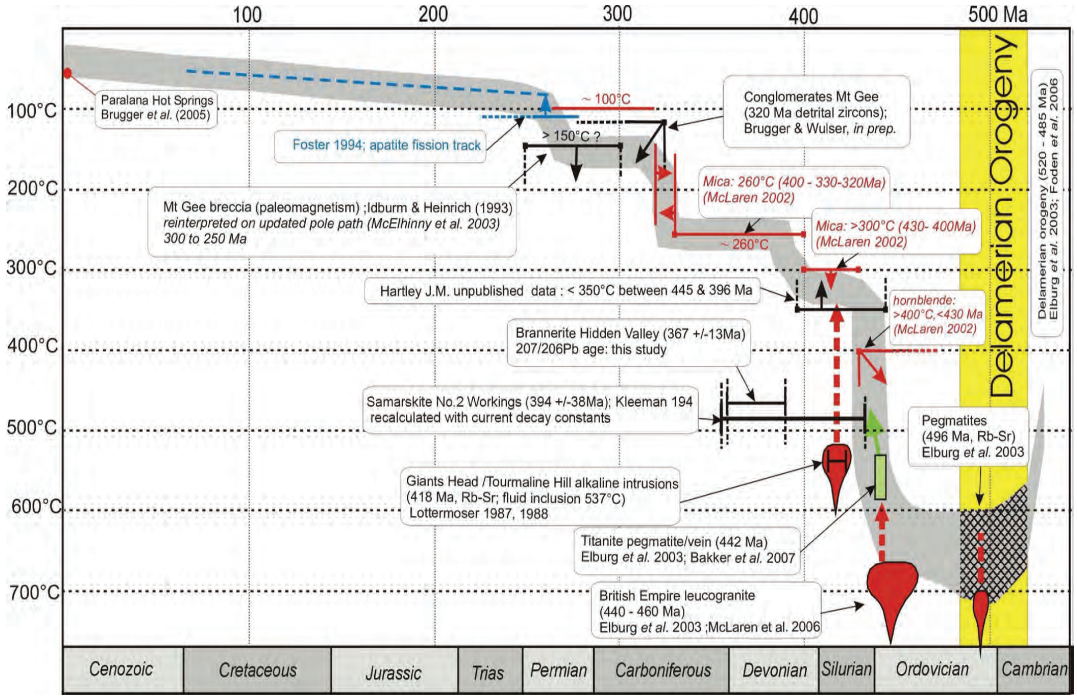

Figure 6.2: *Phanerozoic thermal history of the Mt Painter region. Source: Wülser (2009).*

6.2 GEOLOGY OF THE MOUNT GEE AREA

Crystalline basement in the Mount Gee – Mount Painter area of the Mount Painter Inlier comprises the early Mesoproterozoic Radium Creek Metamorphics and associated metagranitic rocks, intruded by the unmetamorphosed and undeformed Ordovician granites (Fig. 6.3). The area is characterised by the presence of extensive breccias and hydrothermal rocks, which are the host to uranium mineralisation at the Mt Gee deposit.

6.2.1 Mesoproterozoic rocks

The Radium Creek Metamorphics comprise strongly foliated quartz-feldspar-biotite gneisses and schists, in part migmatitic, representing metapelites, metapsammites and felsic metaigneous rocks. The uppermost sequence of these rocks, the Freeling Heights Quartzite, has a maximum depositional age of ~1600-1590 Ma (Fanning and Teale, 2003; Ogilvie, 2006; Fraser and Neumann, 2010), and were intruded by granitic gneisses which have been dated elsewhere in the Mt Painter Inlier with magmatic crytallisation ages of ~1580 Ma and ~1550 Ma metamorphic/recrystallisation ages (Fraser and Neumann, 2010). The nearby Hodgkinson Granodiorite (Hore and Neumann, in prep.), informally referred to as the Paralana Granodiorite, is of I-type composition consisting of plagioclase, quartz, biotite, with minor K-feldspar and amphibole, and has a magmatic crystallisation age of ~1550Ma (Fraser and Neumann, 2010).

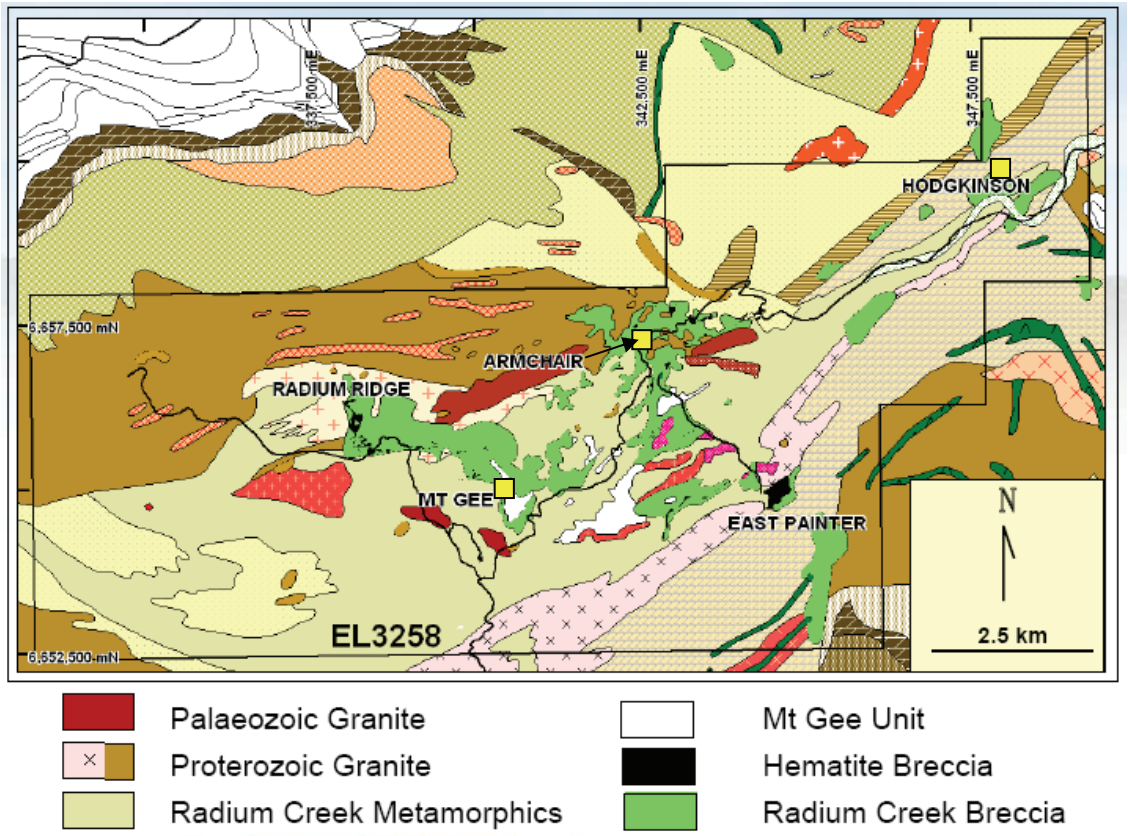

Figure 6.3: *Geology of the Mt Gee – Mt Painter area, and principal uranium deposits (yellow boxes). Note the Mt Gee Unit is also known as the Mt Gee Sinter, and the Radium Creek Breccia is also known as the Radium Ridge Breccias (Drexel and Major, 1987; see also text). Source: PIRSA and Marathon Resources.*

6.2.2 Ordovician intrusive rocks

The ~440 Ma British Empire Granite occurs ~12 km to the northeast of Mt Gee (not shown in Fig. 6.3), has an S-type composition, and contains K-feldspar, quartz, muscovite, garnet, and accessory tourmaline (Lambert et al., 1982; Elburg et al., 2003; McLaren et al., 2006). Several small intrusions of 'soda leucogranite' intrude Adelaidean rocks to the south of the Mt Gee area (Teale et al., 1987; Wülser, 2009, and references therein). Isochron Rb-Sr ages of 450 ± 4 Ma, 418 ± 2 Ma and 372 ± 2 Ma were reported for three of the intrusions (Teale et al., 1987). 'Paleozoic' granites or 'Younger Granites Suite' have been mapped in the Mt Gee - Radium Ridge – Armchair area (Fig. 6.3) and at Hidden Valley to the north-east. Although none of these intrusions in the Mt Gee and Hidden Valley areas have been dated, they have been mapped as part of the same suite as the British Empire Granite.

6.2.3 Breccias and hydrothermal rocks

Breccias are extensively developed in the Mt Gee – Mt Painter – Armchair area, with zones measuring up to ~3 km in length within a 12 km long northeast-trending zone from Radium Ridge to Hematite Hill, near the Hodgkinson prospect (Fig. 6.3). The breccias have been grouped into two major lithological types (Fig. 6.3; Lambert et al., 1982; Drexel and Major, 1987, 1990): (1) the Radium Ridge Breccias (also known as Radium Creek Breccia) including granitic breccia, hematite-rich breccia, and chlorite-rich breccia, which host most of the U-REE mineralisation, and (2) quartz±hematite-rich rocks of the Mt Gee Sinter (also known as the Mt Gee Unit) and quartz veins.

(1) Radium Ridge Breccias:
    - Breccias of local host rock are the most abundant breccia type, and form irregular masses that cross-cut the Mesoproterozoic units. Clasts up to several metres diameter occur in silt to sand sized matrix of the same material or are cemented by hydrothermal quartz, feldspar, hematite and/or chlorite. Clasts are of predominantly 'granitic' composition, with dominant quartz and feldspar, although Lambert et al. (1982), Drexel and Major (1990) and other authors note the widespread K-feldspar alteration in the area. They suggest this K-metasomatism occurred prior to and during the brecciation. Other clasts types include Radium Creek Metamorphics, and laminated and graded siltstone and sandstone lenses.
    - Hematitic breccias generally occur as lenses within the host rock breccia zones, and grade into these enclosing breccias, although hematitic breccia dykes without associated granitic breccia have been described (Lambert et al., 1982). The hematitic breccias contain a high proportion of crystalline (specular) hematite in the matrix, along with chlorite, Fe- and minor Cu-sulfides, and uranium mineralisation (see below). Clasts are dominantly of quartz-feldspar-rich 'granite' or gneiss and of earlier hydrothermal iron oxide rock.
    - Chloritic breccias occur topographically above some areas of hematitic breccia, or occur within the hematitic breccias. Host rock clasts are intensely chloritised, within a chlorite-rich matrix.

(2) The Mt Gee Sinter is at least 200 m thick in places, and is composed of discontinuous, and in places highly vughy, zones of banded quartz and hematite (overall ~60:40 volume ratio), alternating with layers of quartz that apparently supports clasts of coarse specular hematite, and finely laminated quartz-hematite (Lambert et al., 1982; Drexel and Major, 1990; Idnurm and Heinrich, 1993). Minor zeolites (laumontite, stilbite) are present although most have dissolved to form negative crystal cavities (Drexel and Major, 1987; Idnurm and Heinrich, 1993). Quartz in this unit, and also in widespread veins in the area, is characteristically crustiform, filling open spaces. According to published descriptions, later generations of silica of the Mt Gee Sinter cross-cut the Radium Ridge Breccias and its contained uranium mineralisation, for example filling large vughs in these breccias. The nature of this quartz, which clearly formed at very high crustal levels, may have given rise to the interpretation of this lithology as a 'sinter'. At Mt Painter, an unusual occurrence of native sulphur within the quartz-rich Mt Gee Unit was reported by Thomas and Walter (2002), and was interpreted to have formed in an epithermal system.

6.2.4 Diamictite / pebble dyke

A distinctive unit of 'diamictite' or 'pebble dyke' occurs as small outcrops and in drilling in the Mt Gee area. It is composed of well rounded, poorly sorted clasts of highly varied origins including local host rocks, which are set in unmetamorphosed matrix. Its timing and origin remain controversial. In cross sections from Marathon Resources it is shown cross-cutting hematitic breccia and mineralisation (see below). A maximum depositional age of ~320 Ma, based on detrital zircon dating, was reported by Brugger and Wülser (in prep, cited in Wülser, 2009). Paleomagnetic measurements indicate a Permo-Carboniferous age for the 'diamictite' (Idnurm and Heinrich, 1993), who suggested this was consistent with an origin as a Permian tillite deposit.

6.3 MT GEE AND ARMCHAIR U-REE DEPOSITS

6.3.1 Mt Gee resources

During 1969-70 drilling by Exoil NL established continuous mineralisation to the northwest of the Mt Gee topographic feature over an area of 400 m by 120 m with an average vertical thickness of 20 m (Fig. 6.4). Mineralisation generally strikes northwest and dips 30-40^{o} to the northeast and is also horizontal in some sections (PIRSA Open File Envelope 3633).

An indicated and inferred resource of 51 Mt at 615 ppm U_3O_8, yielding 31,300 tonnes of U_3O_8, at a 300 ppm cutoff, was reported by Marathon Resources (Fig. 6.5; 2009, Annual Report). Additionally, a resource of 44 Mt at 0.12% La + Ce was reported by Marathon Resources (2005, Annual Report).

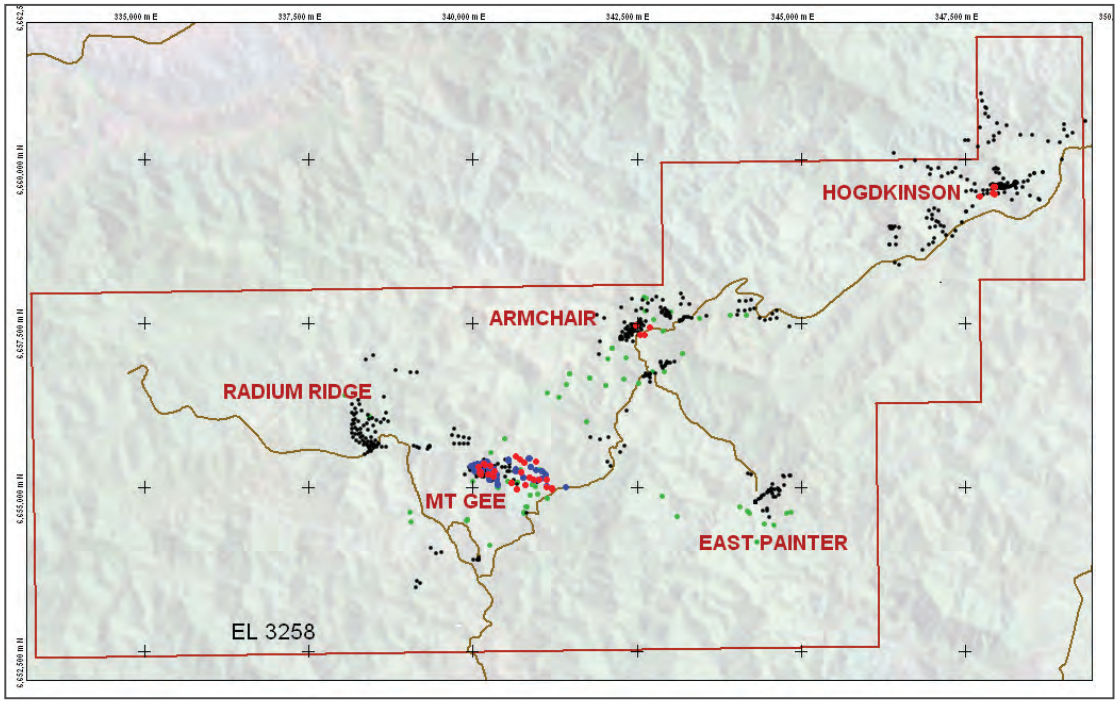

Figure 6.4: *Location of the Mt Gee and Armchair deposits, with drilling. Red: diamond holes drilled by Marathon Resources during 2005-2008, including the three holes studied from the Armchair deposit; blue - percussion holes by Marathon Resources, 2005-2007; green - CRA drill holes, 1991-1993; black - Exoil drill holes, 1968-1971. Source: Marathon Resources.*

The major uranium mineralisation at the Mt Gee deposit occurs as shallow-dipping zones within hematitic breccia (Fig. 6.6), which is itself generally enclosed within granitic breccia. Note that the grades are lower in the area where the Mt Gee Sinter (Mt Gee Unit in Fig. 6.6) appears to intersect the mineralised zone, possibly due to 'dilution' by the post-mineralisation quartz-rich Mt Gee Sinter. Some of the higher grade intersections occur on the flanks of this zone. In contrast, the Armchair deposit (Fig. 6.7) appears to have not been strongly affected by the late-stage Mt Gee Sinter. Nevertheless, the hematitic and chloritic breccias and mineralisation appear to be similar at Mt Gee and Armchair. This is in contrast to the Hodgkinson prospect where uranium mineralisation is hosted by sheared granitic rocks without abundant breccia or iron oxides (Youles, 1970; Phung Nguyen, pers. comm., 2010).

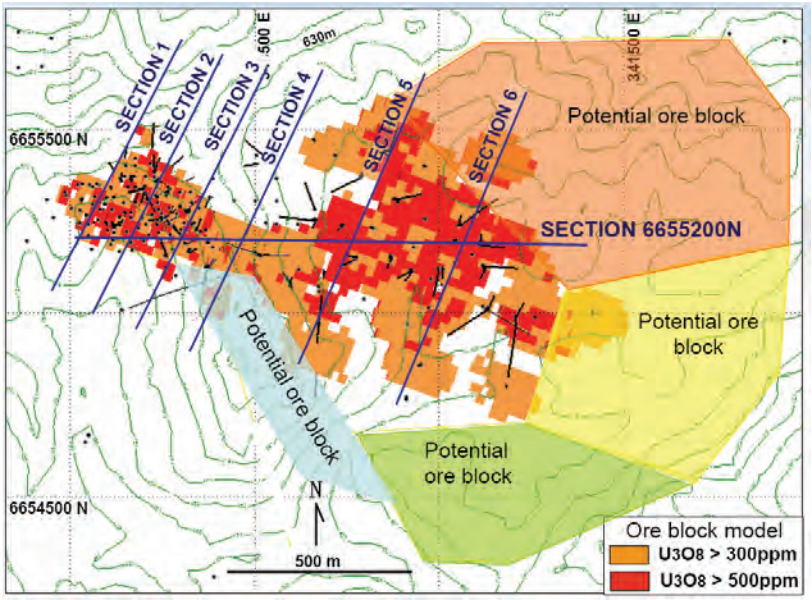

Figure 6.5: *Mt Gee U-REE deposit, plan view of ore block model projected to surface. Source: Marathon Resources (2010, www.marathonresources.com.au).*

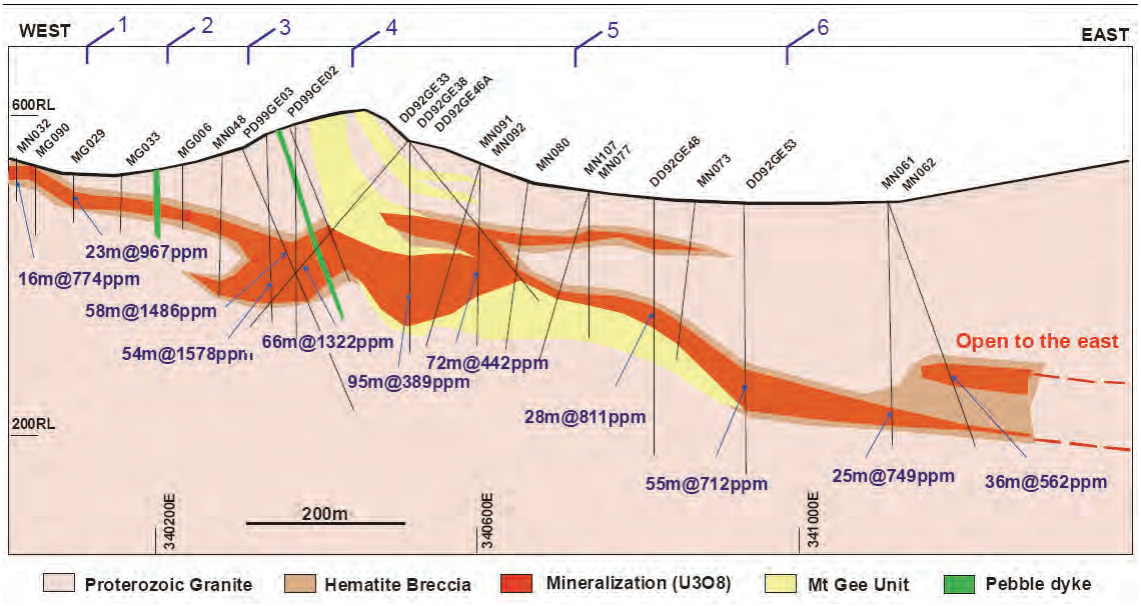

Figure 6.6: *Longitudinal cross section 6655200N (see Fig. 6.4), Mt Gee U-REE deposit. Note: Mt Gee Unit is equivalent to Mt Gee Sinter. Source: Marathon Resources (2010, www.marathonresouces.com.au).*

6.3.2 Armchair resources

Drilling in 1968-69 by Exoil NL established the Armchair deposit as a layer measuring 300 m by 120 m in width with an average vertical thickness of 6 m (Fig. 6.4). The uraniferous hematitic layer strikes northeast and dips 30-40° to the southeast – it crops out to the northwest and is cut off by a fault to the southeast (PIRSA Open File Envelope 3633). Initial drilling by Marathon Resources confirmed mineralisation at the Armchair deposit, although a full resource estimate awaits completion of further drilling. Exoil NL reported an indicative reserve of 680,000 tonnes at 1.0 kg/t (1,000 ppm) U_3O_8, equating to 680 tonnes of uranium oxide.

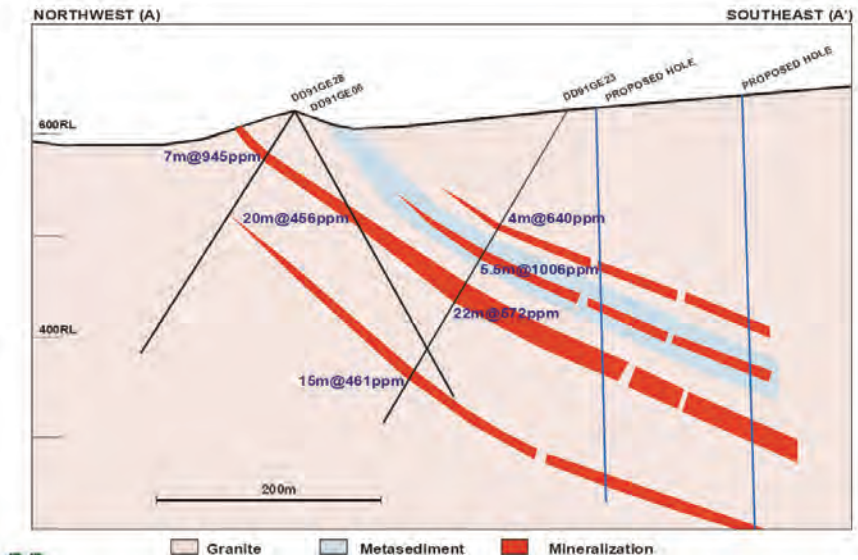

Figure 6.7: *Cross section, Armchair uranium deposit with CRA drillholes numbered. Drillhole MN102 is situated close to the northwestermost proposed hole. From Marathon Resources (website).*

6.3.3 Mt Gee and Armchair geochemistry and U-REE mineralisation

Drexel and Major (1990) reported geochemical results for 81 samples of hematitic breccia, chloritic breccia, Mt Gee Sinter, and local basement. Uranium values are up to 1900 ppm, averaging 660 ppm in hematitic breccias but only 60 ppm in the Mt Gee Sinter. In drill holes some of the better intersections reported by Marathon Resources include 54 m @ 1578 ppm at the Mt Gee deposit, and 16m @ 1169 ppm at the Armchair deposit.

The REE are highly enriched in the hematitic breccias, with up to 1.37% Ce and average values of 6100 ppm reported by Drexel and Major (1990). Although lower in REE, the Mt Gee Sinter is also very anomalous in REE with an average Ce content of 2500 ppm. Mineralogical studies indicate the REE are hosted mainly by monazite. Copper values average 1100 ppm in the hematitic breccias but only 250 ppm in the Mt Gee Sinter. Gold is weakly anomalous, up to 0.2 ppm, and molybdenum values up to 500 ppm were reported by Drexel and Major (1990).

Based on assay results from diamond and percussion drill holes (Marathon Resources, unpublished data), molybdenum is strongly correlated with uranium abundances at both the Mt Gee and Armchair deposits (Figs 6.8, 6.9).

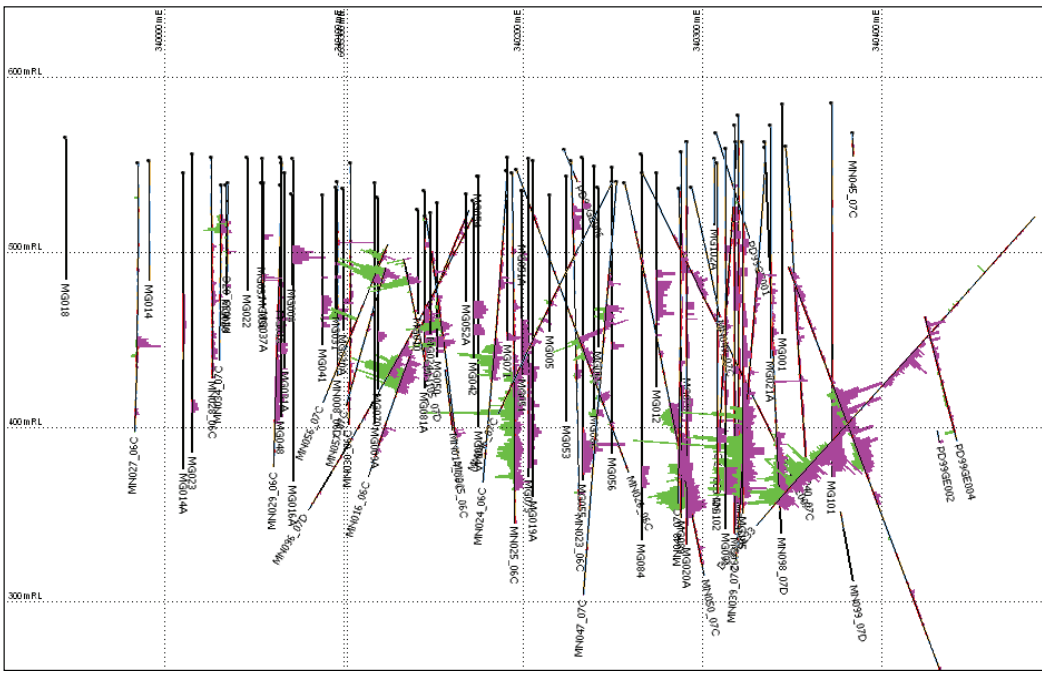

Figure 6.8: *Mt Gee drill hole cross section (NW-SE), showing down-hole uranium (magenta) and molybdenum (green) assays results. Source: Marathon Resources (unpublished data, 2010).*

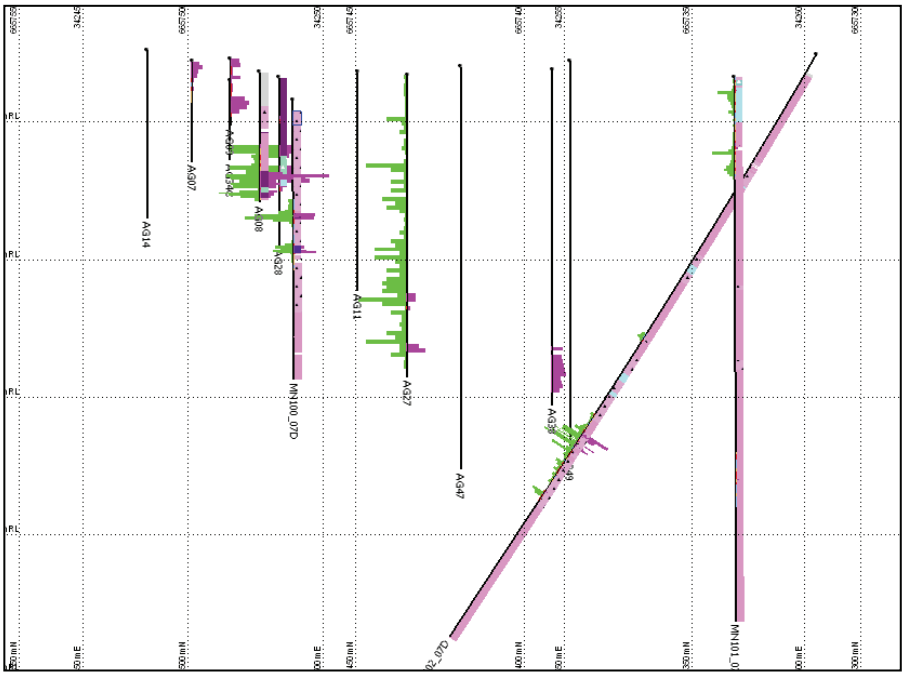

Figure 6.9: *Armchair drill hole cross section (NW-SE), showing uranium (magenta) and molybdenum (green) assays results, and lithology logs. Molybdenite samples were dated from drill hole MN102 at depths of 166m, 167m and 170m. Source: Marathon Resources (unpublished data, 2010).*

6.3.4 Paragenetic sequence and relative timing of molybdenite

Petrography of 11 samples from drill holes MN100, MN102 and MN103 from the Armchair deposit was undertaken to establish a preliminary paragenetic sequence of hydrothermal events including uranium mineralisation, and to determine the relative timing relationships of the molybdenite that was dated by the Re-Os method. A summary of the results is presented in Table 6.1. These findings in general corroborate the paragenetic sequence suggested by Lambert et al. (1982) and Drexel and Major (1990).

Table 6.1. Paragenetic sequence, Armchair deposit for samples from MN100, MN102 and MN103[1]. Wider and narrower bars represent main versus subordinate stages of growth for each mineral.

Mineral	Igneous	Pre-brecciation			Brecciation	Post-brecc.
		K-P-F	Fe; mag	Early hem		
Quartz	▬			▬	Corrosion	▬
K-feldspar	▬				chloritised	
Plag/albite	▬	?	?	?	?	
Muscovite	▬					
Zircon	▬					
Monazite	?	? ▬ ?			▬	
Magnetite	▬		▬			
Hematite				▬	▬	▬
Biotite	? ▬ ?	▬			chloritised	
Apatite	? ▬ ?	▬				
Fluorite	? ▬ ?	▬		▬	▬	
Pyrite			▬	▬	▬	
Molybdenite				?	▬	
Uraninite				? ▬ ?	▬	
Chlorite			?	?	▬	
Bornite			? ▬ ?	? ▬ ?		
Chalcopyrite			? ▬ ?	? ▬ ?		
Digenite						▬
Goethite						▬
Chalcedony						▬
Montmorill.						▬
Illite						▬

[1] Petrographic samples - MN100: 42.2m, 42.8m, 43.0m, 54.0. MN102 : 166.0m, 167.0m, 170.5m (A & B). MN103 : 144.8m, 145.3m (A & B).

All of the studied samples are hematite-rich breccias with rock and mineral clasts of predominantly quartz-feldspar composition, and subordinate clasts of iron oxides, and rare sedimentary(?) clasts. The breccias in drill hole MN100 samples are heterolithic, whereas those in MN102 and MN103 are monolithic. The breccias vary from clast-supported (including jig-saw style) to matrix-supported, and all clasts are angular. Clasts range continuously in size from several centimetres to less than one millimetre, at which point the clasts are equivalent in size to the matrix grain size.

Primary assemblages: The paragenetically earliest recognised mineral assemblages comprise primary igneous minerals in the granitic clasts, and detrital fragments in sedimentary clasts (Fig. 6.10). The granitic clasts contain magmatic quartz, K-feldspar (microcline), muscovite, magnetite, and zircon. Relict biotite in igneous quartz suggests it also was a primary phase. Smaller clasts in the breccia are commonly fragments of these primary magmatic minerals. The sedimentary clasts comprise fine-grained quartz, feldspar and minor hematite, in a chlorite-rich matrix, and display graded bedding (Fig. 6.10C). Igneous feldspar and quartz in granitic clasts show evidence of deformation: feldspar is fractured, and quartz is partially recrystallised and polygonised. Igneous magnetite has been partially to completely altered to martite (Figs 6.10D, 6.10E).

Pre-brecciation assemblages: The mineralogy and texture of clasts in the breccia indicates evidence for three types of hydrothermal alteration, prior to the main stage of brecciation. The relative timing of these three assemblages is not clear from this reconnaissance petrographic study.

- Pre-brecciation biotite-fluorite-apatite-(monazite?) alteration of granite: Several granite clasts have been observed with domains rich in biotite and intergrown fluorite, apatite and monazite(?) (Figs 6.11A, 6.11B). These domains have gradational contacts with less altered granite, and appear to represent veins or replacements of the granite. Biotite clasts of this origin are deformed and partly to completely replaced by chlorite (Fig. 6.11C).
- Pre-brecciation magnetite: Magnetite is rarely preserved in the breccias examined, and is almost entirely replaced by hematite / martite (Fig. 6.12A, 6.12B). Blocky aggregates of martite in the breccia most likely represent pseudomorphed magnetite, which may have once constituted at least 5-15 volume % of the iron oxides in the studied breccias. The origin of this magnetite is uncertain, and it may be of igneous or hydrothermal origin, or both. Rare euhedral magnetite is preserved within coarse hydrothermal pyrite crystals and within a subhedral quartz crystal (Figs 6.12C, 6.12D). Some of the coarse pyrite euhedra and subhedra within the breccia are intensely fractured (Fig. 6.12E), and appear to be clasts of pre-brecciation origin. Our preferred interpretation is that at least some of the magnetite was of hydrothermal origin, and formed part of an alteration assemblage with an early generation of pyrite prior to brecciation.
- Pre-brecciation hematite: Most samples of breccia contain clasts of coarse bladed hematite, set within a matrix rich in finer grained hematite and chlorite; these clasts are most common in samples from drill hole MN100. We interpret the coarse hematite to have formed prior to the main brecciation event, with further hematite growth during the brecciation event.

Syn-brecciation assemblages: The matrix of the breccias is composed almost entirely of hydrothermal minerals, dominated by hematite and chlorite in the studied samples (Fig. 6.13). Other associated minerals in the matrix are: pyrite, fluorite, uraninite, quartz, molybdenite and monazite. Hematite is typically bladed, randomly oriented, and in places constitutes up to 50% of the rock. As noted above, some hematite occurs as martite, replacing blocky magnetite aggregates. Chlorite is generally interstitial to hematite in the matrix, or replaces clasts minerals to varying extents (Figs 6.13A, 6.13B). In MN100 samples, the feldspar in clasts has been entirely replaced by chlorite, with only the quartz remaining. Almost all biotite, whether of primary igneous or hydrothermal origin, has been chloritised (Fig. 6.11C). Quartz displays some unusual textures in the breccia matrix. Whereas fragments of 'primary' quartz are generally irregular in shape and are aggregates of polygonal grains, other quartz crystals in the matrix are euhedral or subhedral, unstrained, and display growth zoning. Fragments of such quartz have not been observed, as might be expected if they were clasts of pre-brecciation material. Other euhedral quartz with growth zoning occurs intergrown with chalcedony in rare patches in the matrix, that are either clasts or late-stage (post-brecciation) infill of cavities in the breccia (our preferred interpretation; see below). The origin of the euhedral quartz is enigmatic. There appears to be some quartz that is transitional between these two end-member textural types, suggesting that the euhedral quartz is hydrothermal in origin and grew via recrystallisation of relict 'primary'

quartz, during the brecciation event. Nevertheless, in the studied hematitic breccia samples, the volume of hydrothermal quartz is relatively small.

Most breccia samples contain up to ~5 vol percent pyrite. It occurs as both coarse euhedra and subhedra (commonly 1-2 mm diameter, and up to 5 mm), and as finer grains in the matrix intergrown with hematite and chlorite. It is unclear whether the large pyrite crystals are clasts, or grew in the matrix during and after breccia formation. The presence of rare magnetite inclusions in large pyrite crystals suggests at least some of this pyrite formed in equilibrium with magnetite, and hence was formed prior to the hematite-forming event, that is, the pyrite was pre-brecciation. Other finer grained pyrite in the matrix may have grown during or soon after brecciation, in equilibrium with hematite and chlorite.

Uraninite is rare in the samples studied, and occurs as euhedral crystals and anhedral aggregates up to 0.5 mm length in the breccia matrix (Fig. 6.13C, 6.13D, 6.13E, 6.15A, 6.15D, 6.15E). One aggregate has a thin rim intergrown with very fine hematite, suggesting it grew in equilibrium with hematite. The euhedral form of some uraninite in the breccia matrix supports the proposal that uraninite formed during the syn-brecciation hydrothermal event, although we cannot rule out the possibility of pre-brecciation growth of some uraninite, and incorporation into the breccia as fragments.

Rare molybdenite is varied in grain size, ranging from fine (50-100 μm) in sample MN102 166.0 and 167.0 to coarse flakes up to 2 mm length in sample MN102 170.5A (Fig. 6.14, 6.15B, 6.15D). Most grains are bent or kinked, demonstrating evidence of weak deformation, and some molybdenite has been partially altered to a lower reflectivity mineral, possibly jordisite (Fig. 6.14B). It is intergrown with hematite, pyrite and chlorite in the matrix, and has not been observed within lithic clasts. The relative timing of molybdenite appears to be similar to uraninite, that is, during the syn-brecciation hydrothermal event, but the possibility of some pre-brecciation growth cannot be ruled out.

Monazite is relatively abundant in some of the samples, with up to 1-2% occurring in a wide range of grain sizes from ~0.5 mm diameter to a few tens of microns (Fig. 6.15). Some of the larger crystals are inclusion-ridden, and may have formed during pre-brecciation hydrothermal alteration events or during igneous events. The finer grained monazite is dispersed throughout the chlorite-hematite-rich breccia matrix, and is interpreted to have grown synchronously with the chlorite, hematite, uraninite and molybdenite. Fluorite is a widespread minor constituent (<1 vol. %) in the breccia matrix, intergrown with chlorite and hematite. It varies from colourless to purple, and is interpreted to have formed as part of the hydrothermal alteration assemblage during or after brecciation.

Post-brecciation assemblages: Bornite-chalcopyrite aggregates have been replaced by secondary copper sulfides, most likely mixtures of digenite and neodigenite. The timing of this alteration is unclear, and it could be related to the late stages of the hydrothermal events associated with brecciation, or recent supergene processes. As noted above, rare intergrowths of euhedral, growth-zoned, quartz and chalcedony within the breccia matrix (Figs 6.16A, 6.16B) are interpreted to represent infill of cavities in the breccia. It is possible that this silica represents the 'Mt Gee-type quartz' described by many authors in the Mt Gee area. In some areas of the Armchair deposit, hydrothermal chlorite has been altered to montmorillonite, and granite has been intensely altered to illite-kaolinite even at depths of >300 m (S. Hore, unpubl. data). This clay alteration is post-brecciation; its origin is presently unknown.

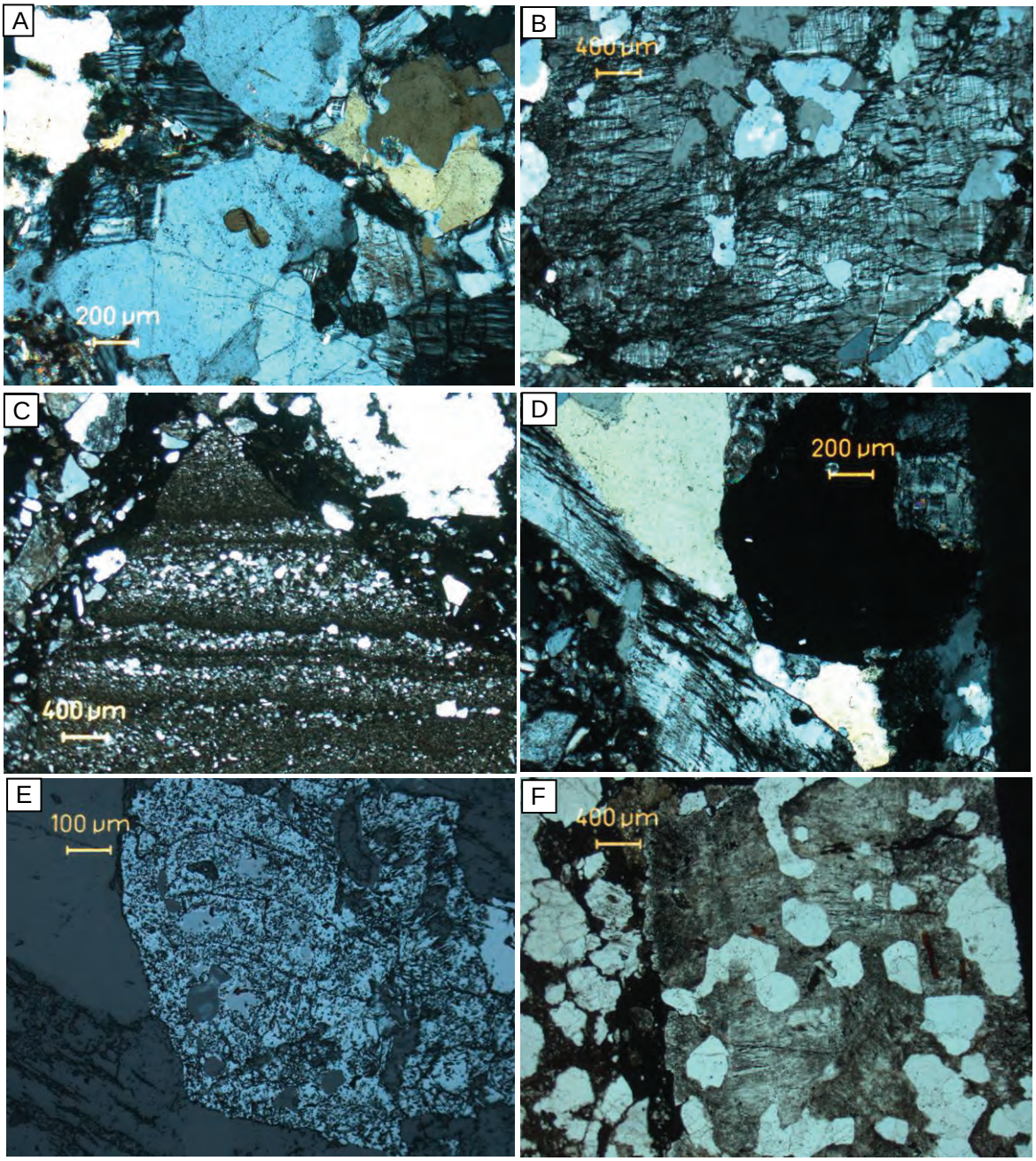

Figure 6.10: *Igneous stage: granitic and other clast types.*

A. Granite clast with quartz, feldspar and preserved biotite inclusion in quartz. Plane light, crossed polars.

B. Large K-feldspar (microcline) crystal, fractured and deformed. Plane light, crossed polars.

C. Clast of graded-bedded clastic rock, with quartz, feldspar grains, uncommon fine hematite laths, in a chloritic matrix. Plane light, uncrossed polars.

D. Quartz-microcline-magnetite in granitic clast. Plane light, crossed polars.

E. Close-up of magnetite in D, showing igneous magnetite partly replaced by hematite (martite). Reflected light.

F. Large K-feldspar crystal with graphic quartz intergrowths, some of subhedral shape. Plane light, uncrossed polars.

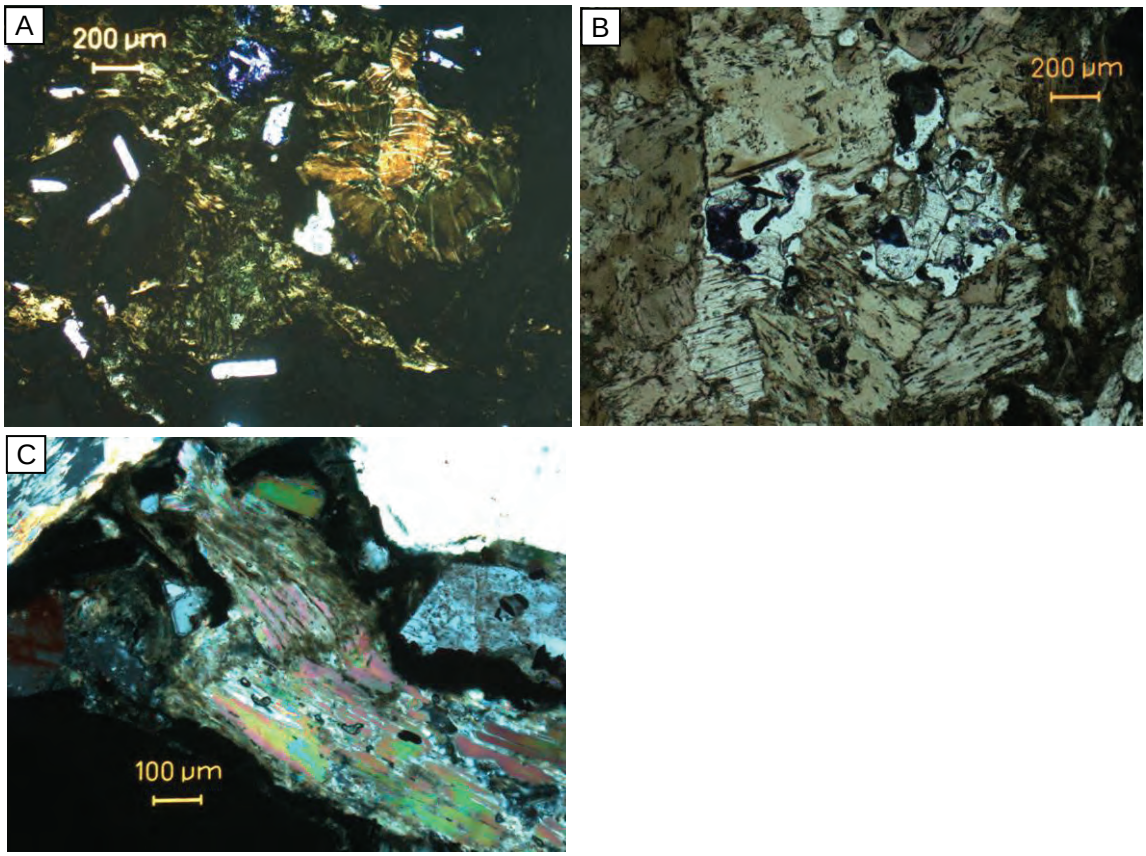

Figure 6.11: *Pre-brecciation stage: biotite-fluorite-apatite alteration.*

A. Biotite (partly chloritised) alteration of granitic rock, intergrown with fluorite (purple), monazite(?) prisms (left and bottom), and minor quartz (centre). Plane light, uncrossed polars.

B. Biotite alteration of granitic rock, intergrown with fluorite and apatite. Plane light, uncrossed polars.

C. *Biotite clast in breccia, partly veined and altered to chlorite. Plane light, crossed polars.*

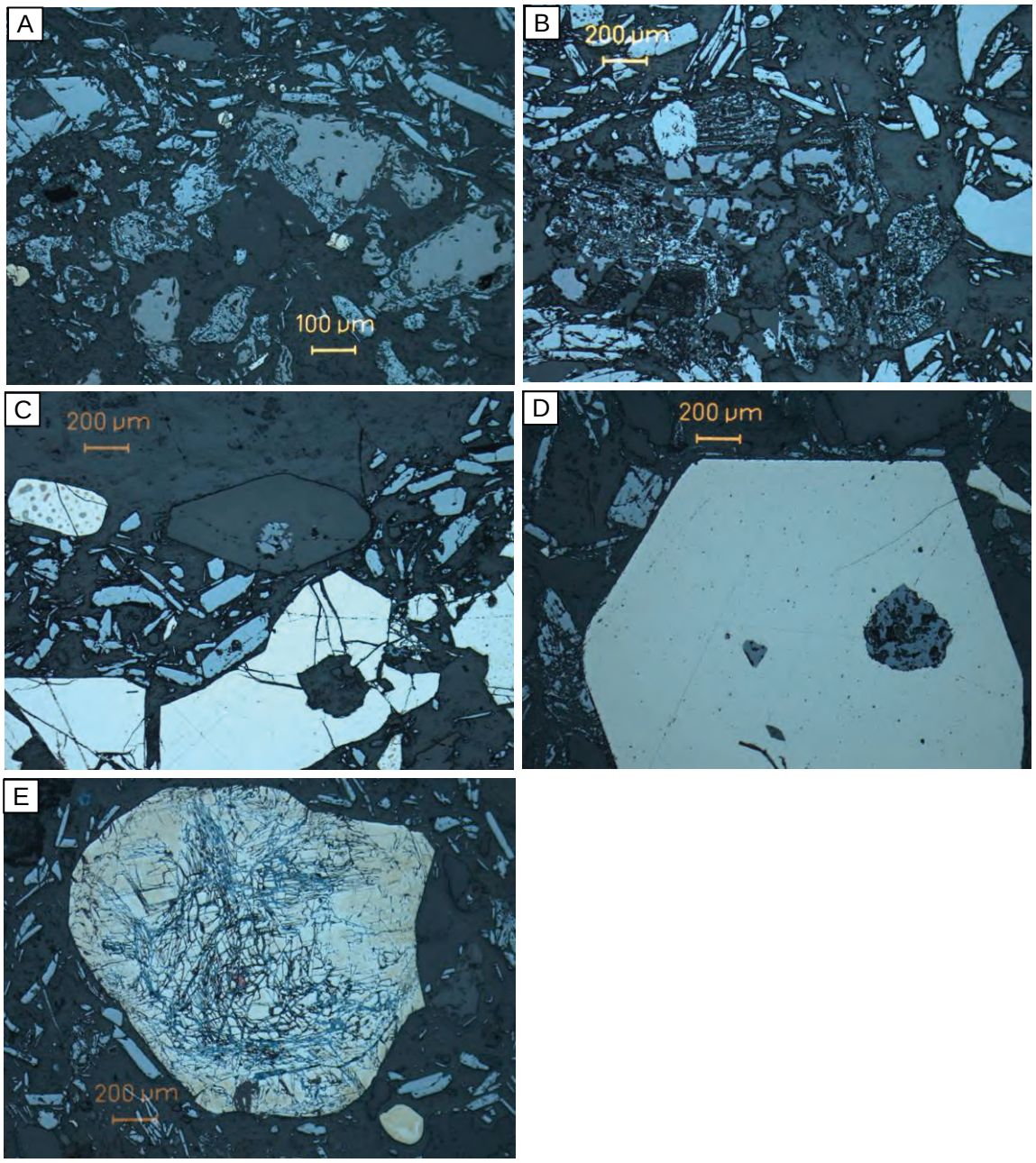

Figure 6.12: *Pre-brecciation stage: magnetite-pyrite alteration (all images reflected light).*

A. Clasts of hydrothermal magnetite, partly replaced by hematite (martite).

B. Clasts of hydrothermal magnetite, partly replaced by hematite (martite) and larger bladed hematite crystals.

C. Subhedral quartz crystal in breccia, with inclusion of magnetite. Hematite blades in breccia matrix and coarse fractured pyrite clasts?

D. Large pyrite euhedra with magnetite inclusion.

E. Large pyrite crystal, with cracks filled by copper sulfides (mainly digenite, neodigenite).

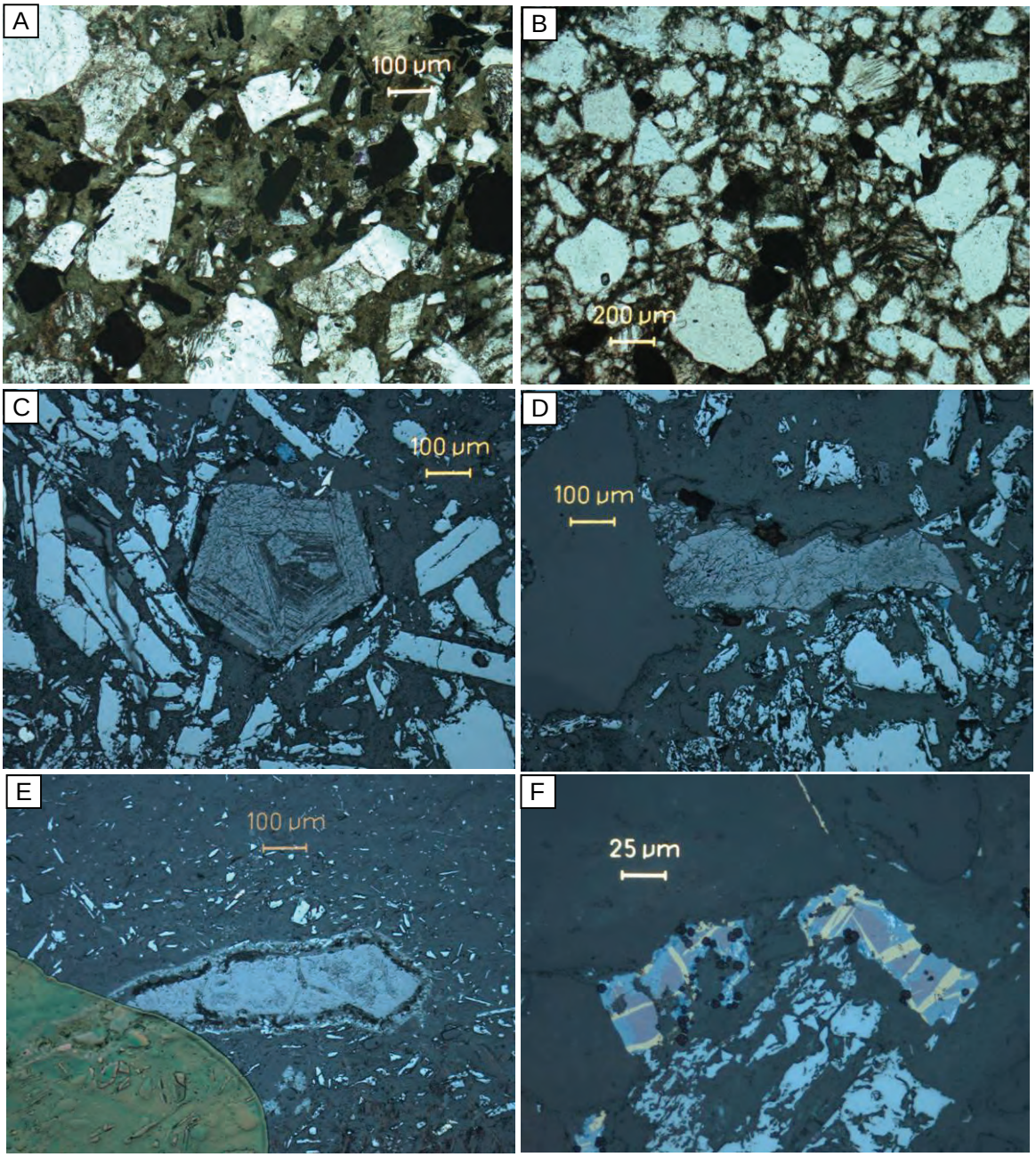

Figure 6.13: *Brecciation stage: hematite-chlorite alteration, uraninite, chalcopyrite.*

A. Breccia with chlorite-hematite-pyrite-fluorite matrix, and clasts of relict igneous quartz. Plane light, uncrossed polars.

B. Breccia with chlorite-rich matrix, minor hematite and pyrite, and clasts of relict igneous quartz. Plane light, uncrossed polars.

C. Uraninite euhedra, intergrown with hematite, in breccia matrix. Reflected light.

D. Uraninite in breccia matrix, intergrown with hematite. Reflected light.

E. Uraninite with rim intergrown with very fine hematite, in breccia matrix. Reflected light. Note pen surface marking at lower left.

F. Bornite with chalcopyrite exsolution lamellae; the bornite is partly replaced around margin by digenite/neodigenite, and appears to be intergrown with hematite. Reflected light.

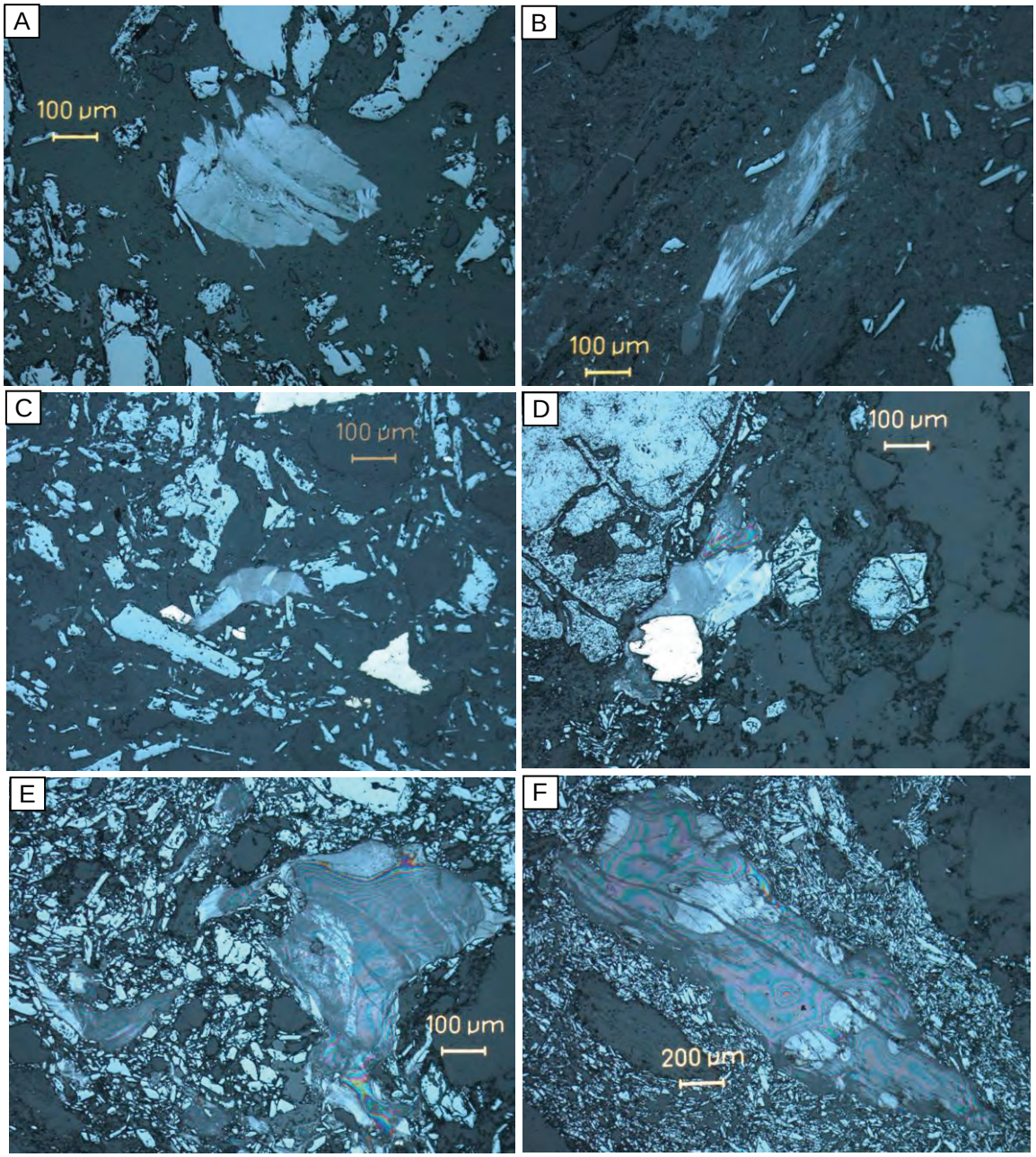

Figure 6.14: *Brecciation stage: molybdenite (all images reflected light).*

- *A. Molybdenite (centre, mid to light greys) and hematite (light grey).*
- *B. Large molybdenite crystal, partly altered to lower reflectivity mineral (jordisite?).*
- *C. Fine molybdenite, kinked (centre) with hematite and pyrite (white) in breccia matrix.*
- *D. Fine molybdenite, bent, and intergrown with block martite after magnetite and pyrite.*
- *E. Large deformed crystals of molybdenite intergrown with hematite (note surface tarnish).*
- *F. Very large weakly deformed crystal of molybdenite intergrown with fine hematite (note surface tarnish)*

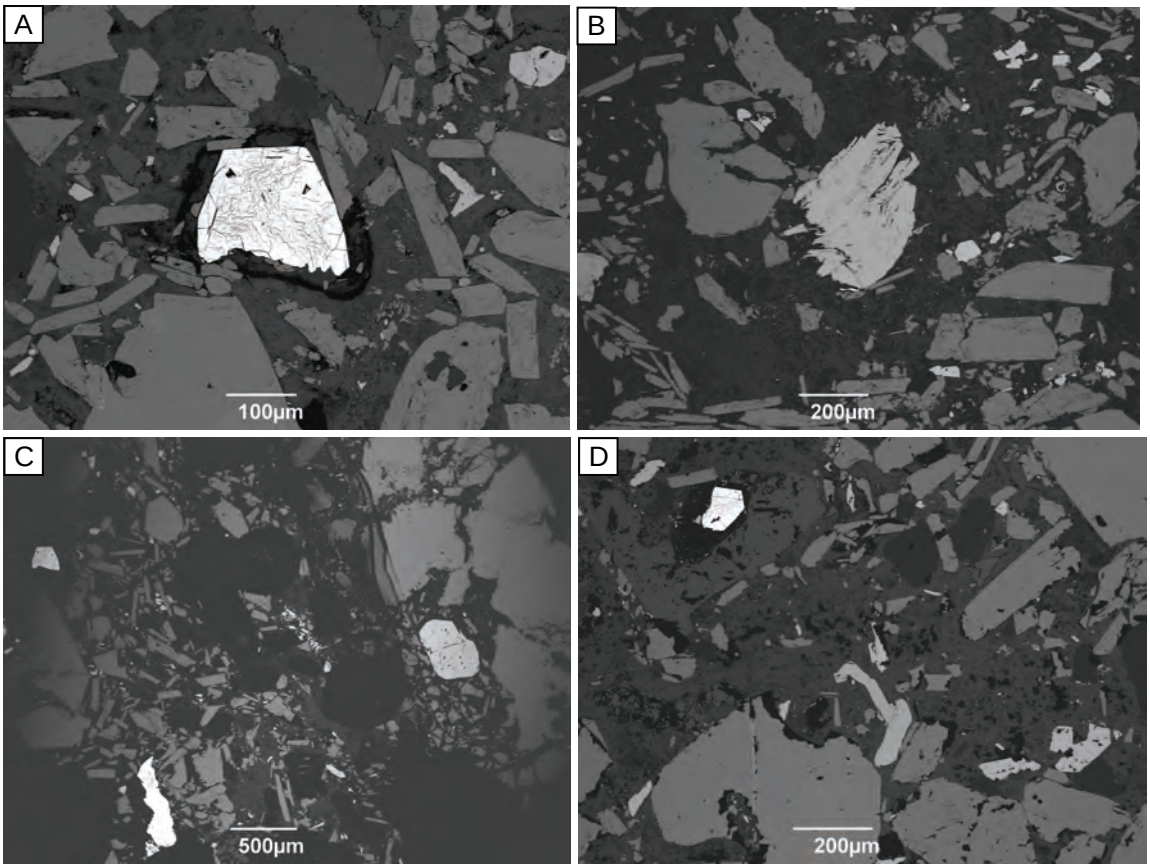

Figure 6.15: *Brecciation stage : SEM images.*

A. Uraninite subhedra (centre, white) within breccia matrix composed of hematite (mid grey), pyrite, monazite (light grey, right), chlorite, fluorite and quartz (darker greys). The dark rim around the uraninite may be due to radiation damage.

B. Molybdenite (centre, light grey) in matrix, together with hematite and pyrite (mid greys), monazite (small light grey crystals at right), and chlorite (dark grey).

C. Large monazite crystal (right, light grey) and fine monazite (light grey, e.g., centre), and uraninite (white, lower left and upper left), in matrix together with hematite and pyrite (mid greys) and chlorite and quartz (dark greys).

D. Uraninite (white, upper left) surrounded by fluorite, molybdenite (light grey, below centre), and monazite (light grey, e.g., lower right), in matrix together with pyrite and hematite (mid greys), chlorite and quartz (dark greys).

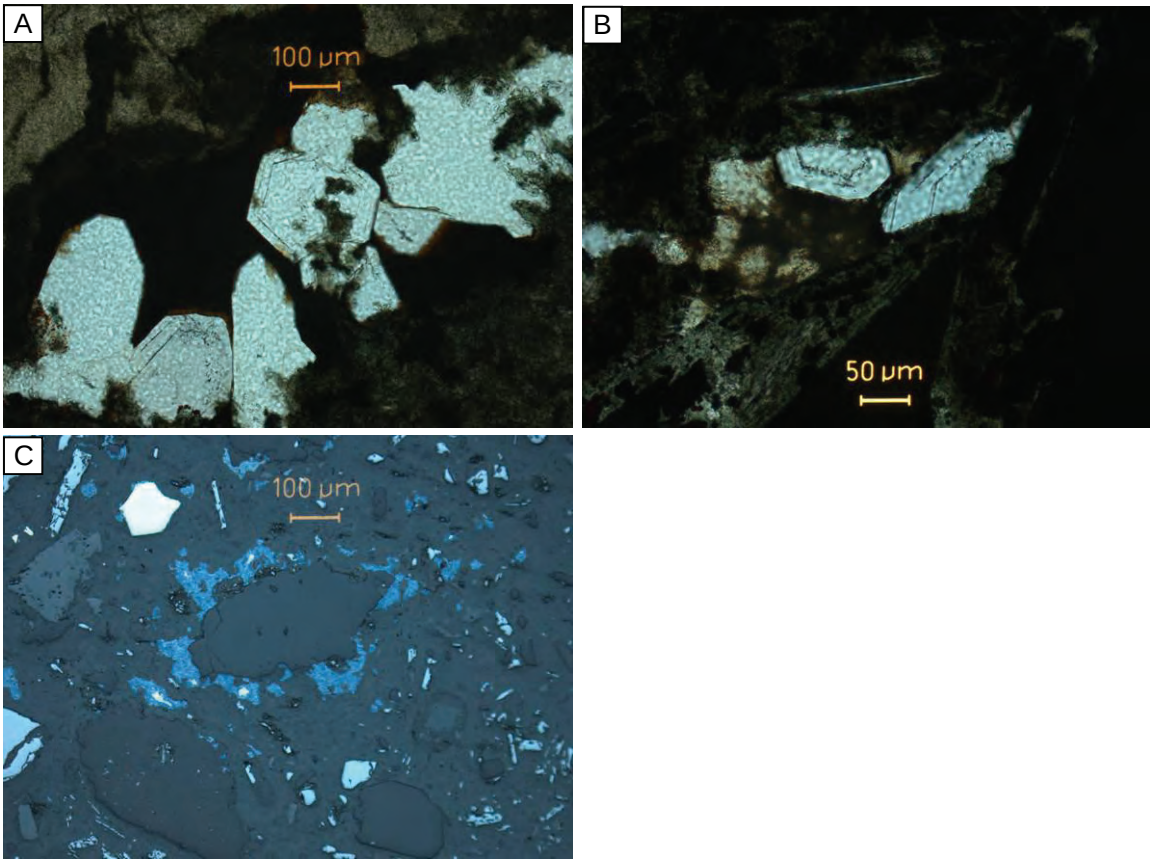

Figure 6.16: *Post-brecciation assemblages.*

A. Growth-zoned euhedral quartz, lining cavity(?) in breccia matrix. Plane light, uncrossed polars.

B. Growth-zoned euhedral quartz, lining cavity(?) with chalcedony, in breccia matrix. Plane light, uncrossed polars.

C. Relict chalcopyrite rimming a quartz clast in breccia, mostly replaced by digenite/neodigenite. Reflected light.

6.4 SAMPLE DESCRIPTIONS

Three samples with molybdenite suitable for Re-Os analysis were selected from the sample set from drill holes MN100, MN102 and MN103. Summary descriptions are presented in Table 6.2, and an image of the drill core from which one of the samples was collected is shown in Figure 6.17.

Table 6.2: Re-Os geochronology samples analysed from the Armchair deposit, drill hole MN102.

SAMPLE	LOCATION (HOLE, DEPTH, M)	DESCRIPTION	MINERAL SEPARATION AND ANALYTICAL METHODS
MN102 166.0	MN102 166.0	Breccia of altered granitic clasts and quartz and feldspar fragments within matrix of specular hematite, chlorite, pyrite, uncommon fine molybdenite, uraninite and monazite. Trace chalcopyrite replaced by digenite/neodigenite. Red very fine hematite present in patches in ~10% of rock.	Molybdenite separated using standard techniques. Re-Os isotope analysis (see Chapter 2)
MN102 167.0	MN102 167.0	Breccia of altered granitic clasts and quartz and feldspar fragments within matrix of specular hematite, chlorite, pyrite, uncommon fine molybdenite, uraninite and monazite. Trace chalcopyrite replaced by digenite/neodigenite. Minor goethite & red very fine hematite present in patches in ~20% of rock.	Molybdenite separated using standard techniques. Re-Os isotope analysis (see Chapter 2)
MN102 170.5	MN102 170.5	Part of breccia: altered granitic clast, partly brecciated, with matrix domain of specular hematite, chlorite, pyrite, monazite, and abundant coarse molybdenite up to 2mm length. Vughs and minor red very fine hematite present in matrix domain.	Molybdenite separated using standard techniques. Re-Os isotope analysis (see Chapter 2)

Figure 6.17: *Drill core from MN102, Armchair deposit, showing hematitic breccia within granitic breccia, and location of Re-Os sample MN102 170.5 (yellow outlined box). Depths of core in tray extend from 167.7m to 172.3 m. Scale bar beneath core tray in 10 cm intervals. Photo courtesy Marathon Resources.*

6.5 RE-OS ISOTOPE RESULTS – ARMCHAIR DEPOSIT

Three Re-Os ages have been obtained from molybdenite in three separate samples in drill hole MN102, between 166 m and 170 m depth. The ages of 360.8 ± 1.7 Ma, 361.6 ± 1.5 Ma, and 364.6 ± 1.5 Ma form a coherent dataset uncertainties just outside one another (Table 6.3). It should be noted that these 2σ uncertainties include the propagated analytical uncertainties and do not include the ~0.3% uncertainty in the decay constant for the Re-Os isotopic system.

Table 6.3: Re-Os results for molybdenite, Armchair U-REE deposit.

Sample	Re ppm	± 2σ	^{187}Re ppb	± 2σ	^{187}Os ppb	± 2σ	Total common Os pg	Model Age (Ma)	± 2σ (Ma)
MN 102-166	219.63	0.55	138044.41	345.77	832.25	2.04	1.51748	360.8	1.69
MN 102-167	718.20	1.83	451421.28	1148.56	2750.61	1.97	1.42789	364.6	1.49
MN 102-170	1449.80	3.63	911263.87	2280.01	5506.33	8.37	2.32656	361.6	1.54

6.6 DISCUSSION

6.6.1 Previous age constraints on uranium mineralisation and alteration

The first age determination on uranium mineralisation in the Mt Gee area was by U-Pb chemical methods yielding an age of 400 ± 50 Ma (Kleeman, 1946). Three monazite samples from the uraniferous hematitic breccias were dated by the U-Pb method by Pidgeon (1979), yielding a poorly defined discordia line interpreted in terms of a primary age of 440 ± 50 Ma and minor recent lead loss. Idnurm and Heinrich (1993) attempted to date the uraniferous hematitic and granitic breccias as well as the Mt Gee Sinter using paleomagnetic methods, but the results were generally of poor quality. Nevertheless, a Permo-Carboniferous age was suggested for the Mt Gee Sinter (Idnurm and Heinrich, 1993). These data were re-interpreted by Wülser (2009) using an updated pole path to give an age of ~300-250 Ma for the Mt Gee Sinter (Fig. 6.2).

Monazite from quartz-hematite alteration ~4.5 km to the south of Mt Gee was analysed by U-Pb isotope methods by Elburg et al. (2003). High common Pb contents prevented rigorous determination of age but the results were consistent with those of Pidgeon (1979). These authors also analysed monazite, as well as a euxenite-series mineral, and secondary torbernite from uranium mineralisation at the Number 2 and Number 6 Workings near Mt Gee. Again, the monazite and Nb-U mineral data show strong reverse discordance, but the ^{207}Pb/^{206}Pb ages are suggestive of monazite and Nb-U mineral formation at ~460 Ma (Elburg et al., 2003).

Wülser (2009) dated davidite (REE-Y-U-Ti-Fe oxide) from the Number 10 Workings at Mt Gee West, by the laser-ICPMS method. A U-Pb age of ~290 Ma was obtained, although the data show strong reverse discordance. Brannerite from pegmatite-hosted U mineralisation in Hidden Valley located between the Mt Neill Granite and British Empire Granite yielded a discordia line with an upper intercept at 367 ± 13 Ma (LA-ICPMS U-Pb data, Wülser, 2009).

Very coarse titanite intergrown with diopside in veins ~3 km south of Mt Gee was dated by Elburg et al. (2003). Voids between the titanite crystals are partly filled by 'Mt Gee type quartz', suggesting the titanite-diopside veins predated the Mt Gee Unit. U-Pb dating yielded an isochron age of 442 ± 4 Ma. Given the geological relationships, this provides a maximum age for Mt Gee type quartz.

6.6.2 Re-Os age interpretation

The three molybdenite Re-Os ages of 360.8 ± 1.7 Ma, 361.6 ± 1.5 Ma, and 364.6 ± 1.5 Ma (late Devonian) are interpreted to represent the age of molybdenite crystallisation, hematite breccia formation, and uranium mineralisation at the Armchair deposit. The molybdenite is interpreted to have grown in the breccia matrix with hematite and uraninite, during or shortly after breccia formation while permeabilities would have been relatively high. Although less likely, we cannot rule out the possibility of either pre-brecciation formation of molybdenite and uraninite, or formation of these minerals significantly later than the brecciation event.

The similarity in geology between the Armchair and Mt Gee U-REE deposits, and strong spatial association between molybdenum and uranium in both deposits (Figs 6.8, 6.9), both support the interpretation that the ages for molybdenite at Armchair are representative of a key uranium mineralising event in the Mt Gee area. However, the Mt Gee mineralisation appears to have been more intensely affected by the cross-cutting Mt Gee Sinter, 'diluting' the uranium grades in parts of the deposit, and possibly upgrading the mineralisation in other parts of the deposit (Fig. 6.5).

The closure temperature for the Re-Os system in molybdenite is approximately 500ºC (Suzuki et al., 1996). Given the low-temperature formation conditions of the Mt Gee Sinter (100-140ºC, Bakker and Elburg, 2006), it is unlikely that the molybdenite Re-Os would have been reset during this late-stage event. The coherence of the three new Re-Os ages within the narrow range of ~361-365 Ma supports this contention.

The Re-Os age results are consistent with:

- Post-Delamerian timing of hematite breccia formation, which is inferred from the lack of metamorphism of the breccia matrix;
- Maximum age of the 'diamictite' or 'pebble dyke' of ~320 Ma (Brugger and Wülser, in prep.), which cross-cuts the hematitic breccia and uranium mineralisation (Marathon Resources, 2010);
- Permo-Carboniferous paleomagnetic age of the Mt Gee Sinter (Idnurm and Heinrich, 1993), which post-dates the hematitic breccias.

The Re-Os ages are significantly younger than the ages of Ordovician S- and I-type intrusions in the region (~460-440 Ma, Elburg et al., 2003; McLaren et al., 2006), titanite-diopside veins (~440 Ma, Elburg et al., 2003), and some of the imprecise monazite ages from uranium mineralised breccias (e.g., 440 ± 50 Ma, Pidgeon, 1979; ~460 Ma, Elburg et al., 2003). The 367 ± 13 Ma brannerite age of Wülser (2009), however, is within uncertainty of the molybdenite ages, and points to a Devonian uranium mineralising event not only at Mt Gee but affecting other parts of the Mt Painter Province.

Younger regional events include the rapid cooling recorded in $^{40}Ar/^{39}Ar$ data around 330-320 Ma in the Mt Painter region (McLaren et al., 2002), and Carboniferous plutonism beneath the Cooper Basin around 340-300 Ma (Gatehouse et al., 1985), both of which are believed to correspond to the final stages of the Alice Springs Orogeny. It is noteworthy that the six biotite $^{40}Ar/^{39}Ar$ total fusion and plateau ages reported by McLaren et al. (2002) are in the range 401-365 Ma, suggesting that regional temperatures declined below the biotite closure temperature of ~300ºC at about the time of molybdenite formation. Thus, the hydrothermal system forming the molybdenite and uraninite may have cooled below ~300ºC soon after ~361-365 Ma. Further cooling at ~330-320 Ma was recorded by K-feldspar $^{40}Ar/^{39}Ar$ ages.

Although no magmatism is known from the Mt Painter region in the late Devonian, this period corresponds to the Kanimblan Cycle of eastern Australia, where there was extensive basin development and volcanism in the Thomson Orogen (e.g., Drummond Basin) and Lachlan Orogen (see Champion et al., 2009, and references therein).

It is interesting to note that in the Victorian Goldfields of the Lachlan Orogen the two major gold mineralisation periods were at ~440 Ma and ~380-365 Ma (Champion et al., 2009). The earlier event corresponds temporally with emplacement of the British Empire Granite and related thermal effects in the Mt Painter region (Vos et al., 2007). The later gold event in Victoria is spatially and temporally associated with felsic magmatism in that region, and is in part coeval with the proposed timing of uranium mineralisation in the Mt Painter Province. At approximately 360 Ma tectonism in the Paleozoic orogens of eastern Australia switched from broadly extensional to compressional, during the Kanimblan Orogeny (Champion et al., 2009). Whether these tectonic effects during the Kanimblan Cycle played a significant role in driving hydrothermal activity in the Mt Painter region remains to be established.

7. Maureen U deposit, Queensland

David Huston[1], Roland Maas[2], Natalie Kositcin[1], and Geoff Fraser[1]

7.1 INTRODUCTION

The Maureen deposit, located 35 km northwest of Georgetown (Fig. 5.1), is one of the largest known uranium deposits in northeast Queensland. Uncut NI43-101-compliant resources include 3.278 Mt grading 0.10% U_3O_8 and 0.07% Mo for a total of 3.31 kt U_3O_8 and 2.42 kt Mo. The Ben Lomond deposit (1.93 Mt grading 0.25% U_3O_8 and 0.15% Mo for 4.83 kt U_3O_8 and 2.90 kt Mo – NI43-101-compliant) west of Townsville, and the Maureen deposit have been considered examples of volcanic-associated deposits (Bain, 1977; Morrison and Beams, 1995). More recently, however, Wall (2006), Hurtig (2008) and Mathison and Hurtig (2009) have interpreted the Maureen deposit as an unconformity-related style. The deposit has diagnostic characteristics of both volcanic-associated and unconformity-related types, being associated with volcanic rocks that form part of a Paleozoic stratigraphic package that unconformably overlies Mesoproterozoic basement rocks (Fig. 7.1). In an effort to clarify the origin of mineralisation at Maureen, this study was initiated to provide firm age constraints for the deposit and its host rocks. If the deposit is syn-volcanic, the ages of host volcanics and mineralisation should be the same. By contrast, if U-Mo mineralisation is unconformity-related, i.e. epigenetic, it could be considerably younger than its host rocks.

To constrain the age of the host rocks, a sample of interpreted felsic volcanic rock within the succession overlying the unconformity was submitted for SHRIMP U-Pb zircon dating. Attempts to determine the age of U-Mo mineralisation involved four different methods: (1) Re-Os dating of jordisite (amorphous MoS_2), (2) ^{40}Ar-^{39}Ar dating of sericite, (3) U-Pb dating of fluorite, and (4) Rb-Sr dating of sericite and fluorite. Somewhat unexpectedly, dating the mineralisation was not straightforward: the Re-Os dating was unsuccessful because the jordisite contained insufficient Re and Os for analysis, while the ^{40}Ar-^{39}Ar and Rb-Sr isotope systematics for sericite contain a substantial inherited component. For this reason, the ^{40}Ar-^{39}Ar and Rb-Sr analyses are not reported herein; they will be reported elsewhere. However, U-Pb dating of fluorite produced robust and geologically meaningful results which are presented below.

7.2 GEOLOGICAL SETTING

Numerous small U-F-Mo prospects along with the larger Maureen and Ben Lomond deposits are present in the Townsville hinterland, and have a spatial association with Permo-Carboniferous felsic volcanics and sediments of the Kennedy magmatic province. However, in most cases these deposits are also localised along the unconformity with Proterozoic basement (Fig. 5.1).

[1] Geoscience Australia, GPO Box 378, Canberra, A.C.T. Australia 2601
[2] University of Melbourne, Victoria 3010, Australia

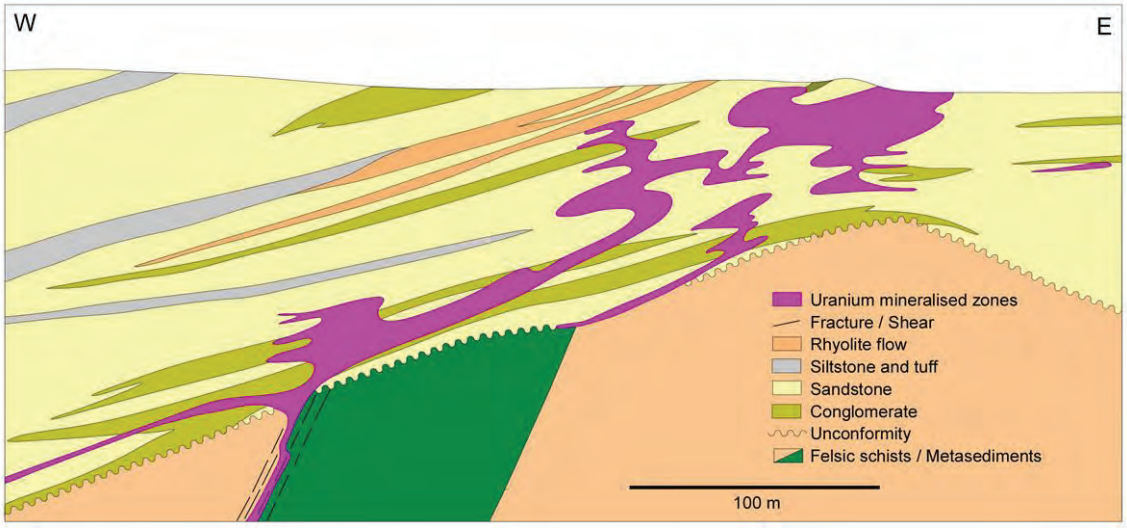

Figure 7.1: *Schematic longitudinal section of the Maureen deposit (modified from Jones, 2006).*

7.3 MAUREEN U DEPOSIT

The Maureen deposit and nearby prospects are localised near the unconformity between Mesoproterozoic sedimentary rocks and dolerites and Paleozoic sedimentary rocks that grade upwards into volcaniclastic sandstone, tuffaceous rocks and rhyolitic ignimbrite. Mathison and Hurtig (2009) interpreted the Paleozoic rocks to be part of the Late Carboniferous to Early Permian Maureen Volcanic Group rather than the Devonian Gilberton Formation, as suggested by Denaro et al. (1997).

The Mesoproterozoic Lane Creek Formation forms the basement below the Maureen unconformity (Fig. 7.1). The original sediments consisted of laminated, highly carbonaceous mudstone and siltstone, interbedded with pale grey to white mudstone and siltstone. Thin, relatively pure recrystallised limestone beds occur locally. Metamorphism of the Lane Creek Formation has produced mainly mica schists with some quartzite and calc-silicate rocks (Withnall et al., 1997). Carbonaceous schists are generally finer grained than non-carbonaceous schists. Andalusite and cordierite occur in rocks of higher metamorphic grade (amphibolite facies). Locally these rocks are migmatitic.

The unconformity above the Lane Creek Formation metasediments is overlain by a basal conglomerate. Locally, the lower part of the basalt conglomerate is a thin bed of black or dark grey carbonaceous and pyritic siltstone. The basal conglomerate is overlain by a lower clastic sequence (up to 150 m thick) composed of variably micaceous conglomerate, pebbly sandstone, muddy feldspathic sandstone and hematitic fine grained sandstone and siltstone. The lower clastic sequence grades upwards into an upper clastic sequence of volcaniclastic sandstone with rhyolite clasts, red, micaceous and muddy sandstone and tuffaceous siltstone and hematitic mudstone.

Replacement-style U-Mo mineralisation is hosted in volcanogenic rocks close to the unconformity (generally within 100 m stratigraphically). Mineralised zones are commonly roughly parallel to

bedding but can also form vertical zones that plunge westwards along the unconformity. Locally, shear-hosted sulphide-rich U-Mo veins extend below the unconformity into the underlying metamorphic basement. U-Mo mineralisation ranges from partial replacement, disseminations and thin veins to total replacement of the original host rock by fluorite, clays, and sulphides (including molybdenite and uranium). Mo and U generally occur together but patches of uranium- and molybdenum-only mineralisation also occur (Mathison and Hurtig, 2009).

Sulphide assemblages in primary mineralised zones are dominated by jordisite, with additional arsenopyrite, arsenian pyrite and minor sphalerite. Associated minerals include fluorite, dickite, chamosite, goyazite, anatase, and carbon. The main primary uranium mineral is very fine grained uraninite (Mathison and Hurtig, 2009). In the oxidised zone, the uranium minerals are mainly complex uranium phosphates, including saleeite, renardite, meta-uranocircite, autunite and meta-autunite (Bain, 1977). Minor primary and secondary molybdenum-bearing minerals include ferrimolybdite, umohoite, wolfenite, powellite, ilsemannite and iriginite (Bain, 1977). Alteration halos around higher grade zones contain fluorite, dickite, chamosite and disseminated pyrite.

Interpretation of U mineralisation at Maureen and similar deposits nearby has been controversial because the deposits exhibit characteristics that can be assigned to two major classes of U mineralisation: they are spatially associated with felsic volcanics and they occur close to a major unconformity (Mathison and Hurtig, 2009). Hence, the deposits have characteristics of both volcanic and unconformity-related deposits using the IAEA classification (McKay and Miezitis, 2001). The available evidence favours classification as an unconformity-related deposit: (i) the vast bulk (98%) of the uranium at Maureen occurs within the lower part of the conglomerate (within 100 m of the basal unconformity), and the rest is in the underlying basement (Miller and Mortimer, 1974); (ii) petrographic and fluid inclusion studies suggest U mineralisation occurred via mixing of descending or laterally moving, oxidised U-rich fluids with ascending, methane-bearing fluids (Hurtig, 2008; Mathison and Hurtig, 2009). The uranium-bearing fluids were interpreted to have moderate salinities (3-16 eq wt % NaCl) and temperatures between 210 and 300°C. These fluid characteristics are very similar to those known from unconformity-related deposits (e.g. Wilde et al., 1989; Komninou and Sverjensky, 1995; Alexandre et al., 2005).

7.4 SAMPLE DESCRIPTIONS AND PETROLOGY

Samples for this study were collected from diamond drill holes 9205 and 9206. Table 7.1 summarises the characteristics of each sample analysed in this study.

Table 7.1: Samples analysed from the Maureen deposit.

SAMPLE	LOCATION (HOLE, DEPTH)	DESCRIPTION	MINERAL SEPARATION AND ANALYTICAL METHODS
2007167002-08	9205, 32.68-32.70 m	Interlayered very fine grained sandstone and siltstone. The sample is cut by chlorite-sericite-carbonate veins at a high angle to bedding. The sandy part contains minor carbonate. This sample is from the unit overlying the unconformity.	Zircon was separated using standard techniques. Analysed using SHRIMP U-Pb
2007167003-05	9206, 152.3-152.5 m	Fluorite-muscovite-clay-sericite veins cutting and replacing sericite-altered quartzose sandstone. In places the veins appear to be replacive of the wall rock, with the margins corroding the wall rock. The clay largely occurs as irregular clots up to 1 mm that are surrounded by fluorite and replaced by fluorite-muscovite intergrowths (see below). This muscovite is recrystallised to finer-grained sericite in places.	Fluorite and muscovite were separated using standard techniques. Muscovite was analysed using laser ^{40}Ar-^{39}Ar step heating. Muscovite and fluorite were analysed using ICP-MS Rb-Sr. Fluorite was also analysed using ICP-MS U-Pb.

7.5 U-Pb ISOTOPE ANALYSIS OF ZIRCON FROM THE PALEOZOIC HOST ROCK

Sample 2007167002-08 was collected in order to determine the emplacement age of the host unit. A detailed description of the zircons and analytical results are presented in Neumann and Kositcin (in prep.). U-Pb data for seven spots on six grains yield predominantly Proterozoic ages. Only one grain has a Paleozoic Pb/U age (2 spots, 335.5 ± 3.1 and 342.3±2.9 Ma, 1σ). The Paleozoic grain could represent the age of volcanic activity coeval with the host sediment, but given the reconnaissance nature of this data set, the ~340 Ma age should be considered a maximum deposition age. This age would allow correlation of the unit with the Carboniferous Gilberton Formation (i.e., Denaro et al., 1997) or the Permo-Carboniferous Maureen Volcanic Formation (i.e., Mathison and Hurtig, 2008).

7.6 U- Pb ISOTOPE ANALYSIS OF FLUORITE AND MUSCOVITE FROM A URANIFEROUS FLUORITE-MUSCOVITE VEIN

Sample 2007167002-05 is an arkosic sandstone cut by a fluorite vein. This sample was selected for Ar-Ar, Rb-Sr, U-Pb and Sm-Nd isotopic work because it contains hydrothermal fluorite and muscovite. Only the fluorite U-Pb isotope data are reported herein; the Ar-Ar and Rb-Sr isotope data will be reported elsewhere.

7.6.1 Petrography of sample 2007167002-05

Figure 7.2A illustrates the general relationship between the vein and the wall rock in sample 2007167002-05. Fluorite progressively replaces the wall rock, initially by replacement of K-feldspar along cleavage planes (Figs. 7.2A and 7.2G), and then by the replacement of quartz grains. The vein itself consists of intimately intergrown fluorite and well-crystallised muscovite. This muscovite appears to be the alteration product of the K-feldspar in the wall rock. The muscovite is commonly altered to poorly crystallised, very fine grained sericite, which paragenetically is the latest hydrothermal mineral.

Monazite (Fig. 7.2B), xenotime (Fig. 7.2C), and zircon are present as trace minerals in the section. Textural relationships suggest that these minerals predated mineralisation. However, monazite and zircon have been extensively altered as a consequence of fluorite alteration. Monazite is partially (Figs. 7.2C and 7.2D) to totally (Fig. 7.2E) replaced by fluorite, with the rare earth elements recrystallised to form florencite (Fig. 7.2E). In Figure 7.2D, the outline of the former monazite grains is partially demarcated by truncation of hydrothermal muscovite. This relationship is taken to indicate that muscovite and associated fluorite replace K-feldspar that enveloped a monazite grain. Zircon contains numerous cracks filled with U-enriched, possibly hydrated secondary zircon. Commonly these composite zircon grains are replaced by fluorite (Fig. 7.2F). These observations may account for some of the isotopic disturbance identified in zircons from sample 2007167002-08 (Neumann et al., 2011). Minor quantities of pyrite are present, both paragenetically associated with fluorite and as late, crosscutting veins (Fig. 7.2G).

Even though sample 2007167002-05 is from an interval averaging only 14 ppm U, it contains a number of uranium minerals. Scanning electron microscopy identified uraninite (Figs. 7.2H, 7.3A, 7.3B, 7.3F and 7.3G), Zr-rich uranium minerals tentatively identified as coffinite (Fig. 7.4C) and soddyite (Figs. 7.2E, 7.2H and 7.4D), an unidentified U-Zr silicate with a uniform molar U:Zr:Si of ~ 4:2:3 (Fig. 7.3E), and U-rich, hydrothermal zircon (Fig. 7.2F). These minerals are most commonly associated with pyrite (Figs. 7.2H, 7.3A, 7.3B, 7.3D and 7.3E), but can also be associated with replaced monazite (Fig. 7.3F) and with anatase (Fig. 7.3G). In many instances, the uranium minerals appear to replace, at least in part, the associated pyrite (Figs. 7.3A and 7.3B), anatase (Fig. 7.3G) and monazite (Fig. 7.3F). Trace sulfide minerals also include chalcopyrite and sphalerite (Fig. 7.2C) as well as galena (Fig. 7.3G) and arsenopyrite (Fig. 7.3H). Other trace minerals include apatite and fluorcaphite ($SrCaCa_3(PO_4)_3F$) (Fig. 7.3C). Primary REE carbonates, which are common in the Nolans Bore and Oasis deposits, were not identified at Maureen.

7.6.2 U-Pb and Sm-Nd analysis of fluorite

Fluorite is associated with uranium minerals at both the meso- and microscopic scales. It was found to have favourable U/Pb and Sm/Nd ratios, and was therefore selected for isotope dilution U-Pb and Sm-Nd isotope work to determine the age of cogenetic uranium mineralisation.

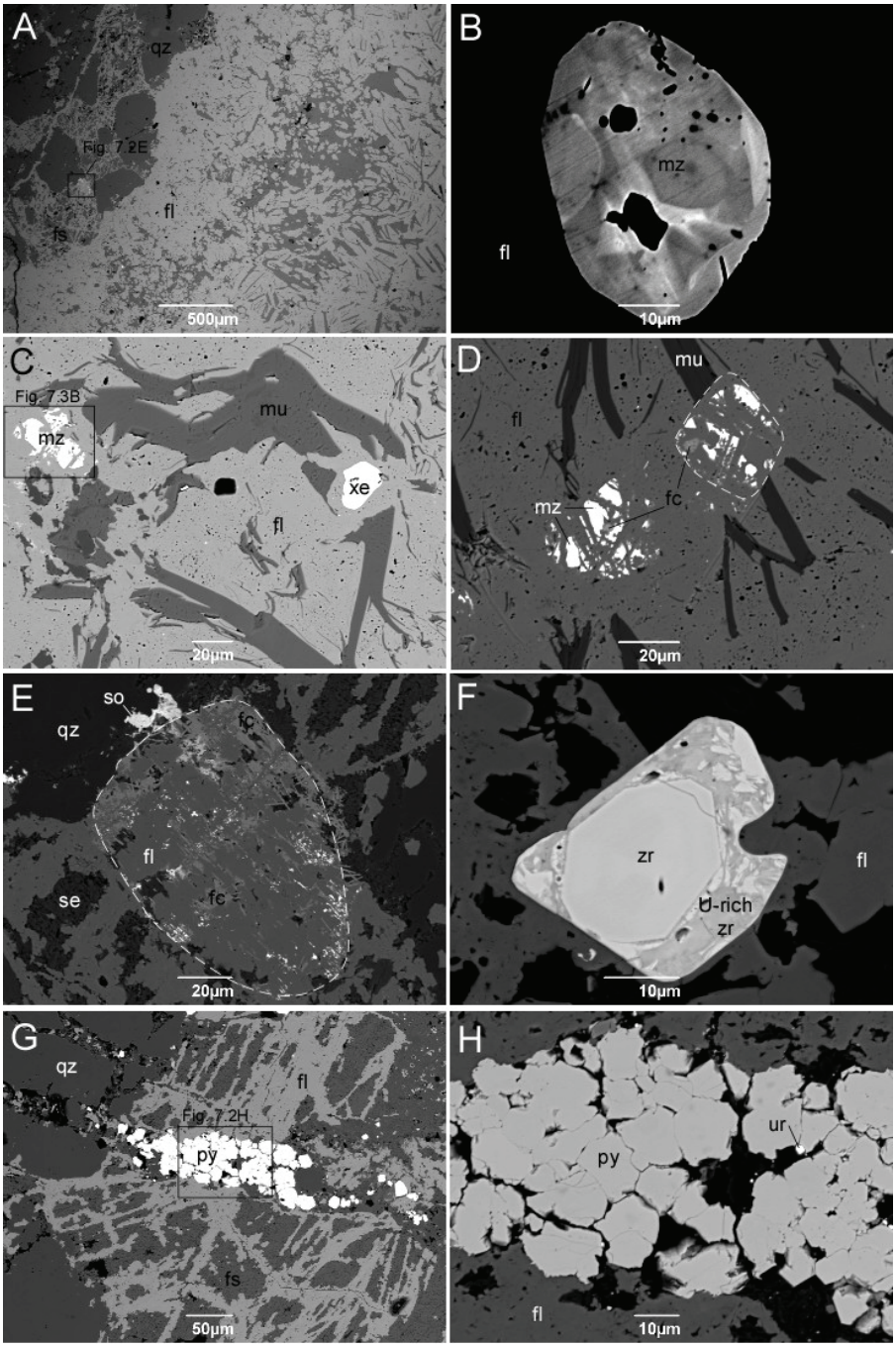

Figure 7.2: *Scanning electron microscope images showing mineral relationships at the Maureen deposit. (A) Fluorite (fl)-muscovite (Mu) assemblage replacing quartz (qz)-K-feldspar (fs) sandstone. (B) Zoned monazite (mz) grain surrounded by fluorite. (C) Xenotime (xe) and extensively replaced monazite grain enclosed by fluorite-muscovite assemblage. (D) Monazite grains extensively replaced by fluorite with lesser florencite (fc). The white dashed line indicates the likely outline of on of the original monazite grains. (E) Monazite grain completely replaced by fluorite, florencite and Zr-rich soddyite (so). (F) Brecciated zircon (zr) grain infilled by U-rich, hydrothermal zircon and embayed by fluorite. (G) Pyrite (py) in late fracture cutting quartz and fluorite-replaced K-feldspar. (H) Enlargement of G showing association of small grain of uraninite (ur) with pyrite.*

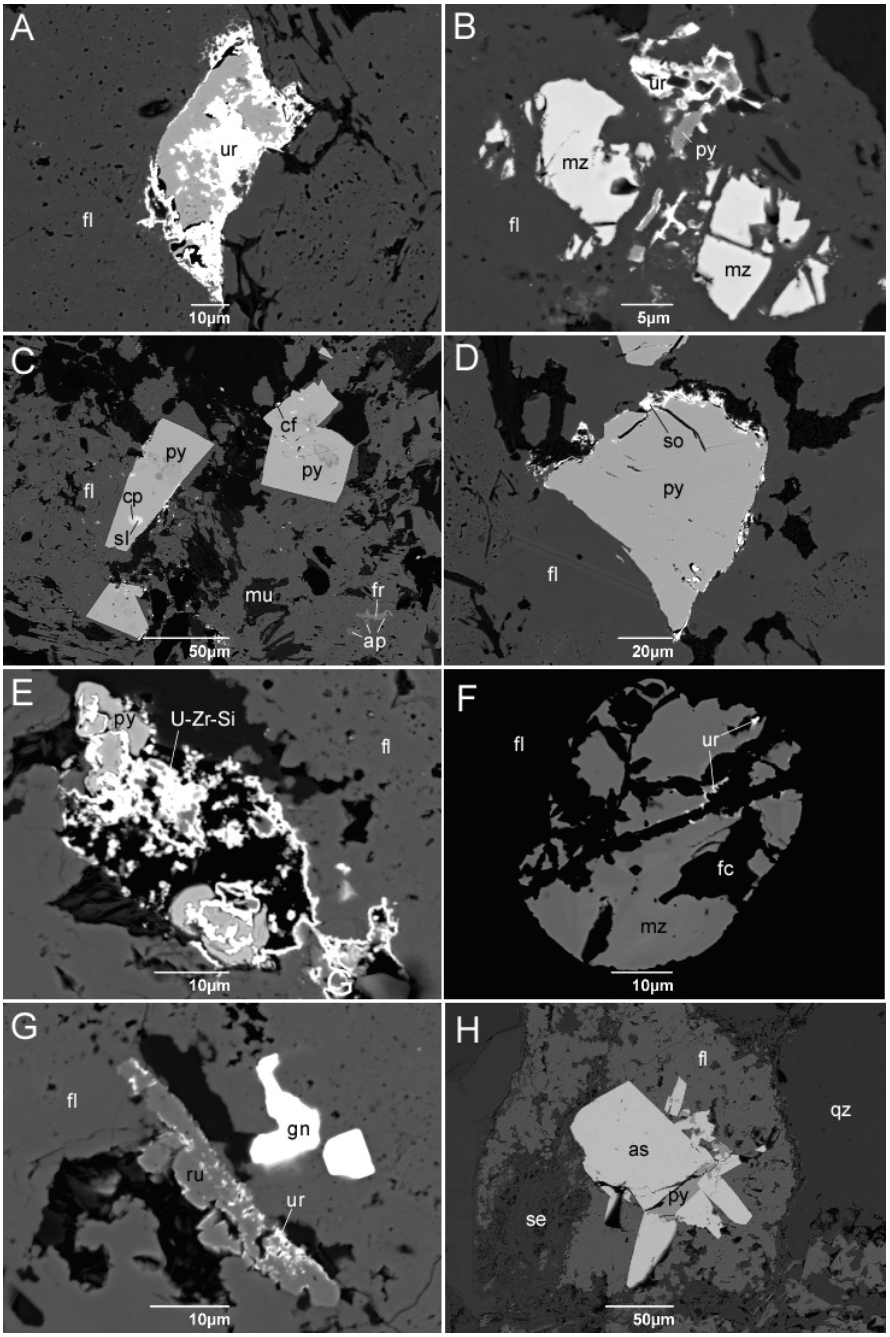

Figure 7.3: *Scanning electron microscope images showing mineral relationships at the Maureen deposit. (A) Uraninite (ur) replacing pyrite (py) within fluorite (fl). (B) Uraninite replacing pyrite, which is associated with fluorite-replaced monazite (mz). (C) Euhedral pyrite grains with inclusions of chalcopyrite (cp) and sphalerite (sl) intergrown. The pyrite is intergrowth with fluorite which also contains muscovite (mu), apatite (ap) and fluorcaphite (fr). (D) Soddyite (so) along the margins of a pyrite grain encapsulated by fluorite. (E) Unidentified U-Zr silicate (U-Zr-Si) associated with pyrite within fluorite. (F) Uraninite associated with monazite where it has been veined by fluorite. The monazite is partly replaced by florencite (fc). (G) Urananite replacing anatase (an), which is enveloped by fluorite and spatially associated with galena (gn). (H) Arsenopyrite (as) associated with pyrite in an assemblage of fluorite-quartz (qz)-sericite (se).*

7.6.2.1 Results

Two fluorite fractions of variable purity contain 24-27 ppm Nd and define an imprecise 2-point Sm-Nd age of 367±83 Ma (Table 7.2, initial ε_{Nd} -14.7). Although too imprecise for our purposes, this apparent age is geologically realistic (within its uncertainty limits) which suggests the fluorites and their impurities are in broad Nd isotopic equilibrium. Three fluorite fractions (159-180 ppm U, 10-15 ppm total Pb, Th/U 0.15-0.2, $^{206}Pb/^{204}Pb$ 96-672) define imprecise ~320 Ma ^{238}U-^{206}Pb and ^{235}U-^{207}Pb isochrons. The radiogenic U-Pb data (after common Pb correction with a 320 Ma growth curve for Pb) are slightly reversely discordant near 320 Ma (Fig 7.4). The most radiogenic analysis (with a $^{206}Pb/^{204}Pb$ of 641) has a nominal $^{206}Pb^*/^{238}U$ age of 330 ± 0.5 Ma and this is taken here as a preliminary age for U-Mo mineralisation at Maureen; however, to account for the observed scatter, we assign an age uncertainty of ±10 Ma.

Table 7.2: Sm-Nd isotopic results for fluorite, Maureen U-Mo deposit

Sample	05 fl #1	05 fl#3
Sm ppm	9.81	8.67
Nd ppm	24.31	27.39
$^{147}Sm/^{144}Nd$	0.2437	0.1912
$^{143}Nd/^{144}Nd$	0.511998	0.511872
e_{Nd0}	-12.48	-14.94
e_{Ndi}	-14.5	-14.7

$^{143}Nd/^{144}Nd$ reported relative to La Jolla=0.511860; internal precision (2sd) ≤±0.000010, external precision (2sd) ±0.000020.

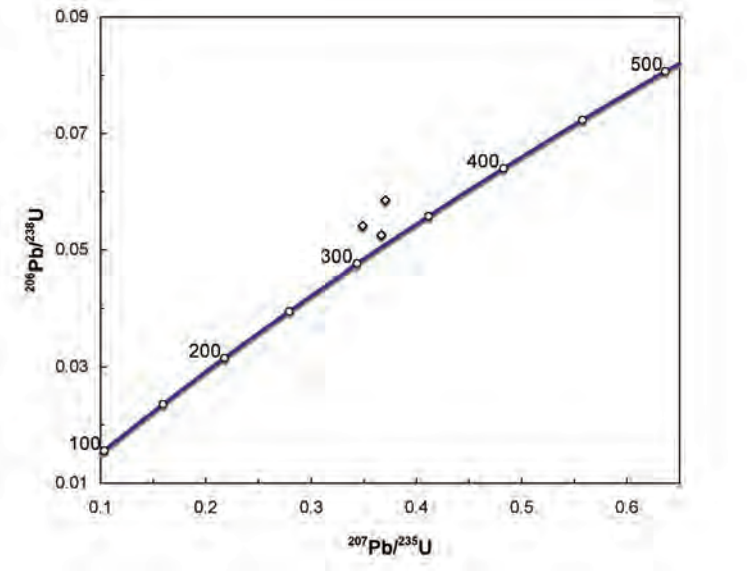

Figure 7.4: *Wetherill Concordia diagram for three isotope dilution analyses of Maureen fluorite. $^{206}Pb/^{204}Pb$ ratios are 96-641. Data corrected for common Pb using 320 Ma Pb from the Stacey-Kramers growth curve. $^{206}Pb^*/^{238}U$ ages for the two most radiogenic data fractions are 330 and 339 Ma, suggesting a Pb/U age of ~330 ± 10 Ma.*

7.7 IMPLICATIONS OF ISOTOPIC RESULTS FOR THE TIMING AND ORIGIN OF THE MAUREEN DEPOSIT

The U-Pb zircon and fluorite results bracket deposition of the Maureen sedimentary package in the interval ~340 to ~330 Ma, i.e Visean. This allows correlation of the local sediment sequence with the Devonian to Carboniferous Gilberton Formation (Denaro et al., 1997). However, the zircon dataset for the host sequence (1 grain) is too small, and the fluorite U-Pb insufficiently precise, to draw more than preliminary conclusions on the exact chronology of sediment deposition and U-Mo mineralisation at Maureen. Most importantly, we are unable to conclusively distinguish between a syngenetic (volcanic-related) and an epigenetic unconformity-style model. In a generic model, glassy felsic volcanic rocks in the Gilberton Formation may have provided a source of easily leached uranium for oxidised brines flowing along the unconformity between the Gilberton Formation and basement. Involvement of basement or basement-derived detritus is indicated by the low ε_{Nd} (~ -14.5 at 330 Ma) of the hydrothermal fluorite.

7.8 CONCLUSIONS

U-Pb ages for syn-mineralisation gangue fluorite from the Maureen deposit indicate a mineralisation age of ~330 ± 10 Ma. Mineralisation is hosted in volcanogenic sandstone and conglomerate currently believed to be ~340 Ma old and possibly correlative with parts of the volcanogenic Devonian-Carboniferous Gilberton Formation. The available age data do not allow differentiation between the alternative volcanic-associated and unconformity-related origins to mineralisation.

8. Summary and conclusions: uranium mineralisation timing in five Australian deposits

Roger Skirrow, David Huston, Geoff Fraser, Andrew Cross, Subhash Jaireth

Results of the current geochronological study of the Nolans Bore, Kintyre, Oasis, Mt Gee-Armchair, and Maureen uranium deposits are summarised in Table 8.1, in order of age of uranium mineralisation.

Table 8.1: Age results for five uranium deposits in Australia.

Deposit, metals	[2]Mineral system	[1]Deposit type	Age (Ma) ± error (2σ)	Method	Interpretation
Nolans Bore, REE-U-Th	Magmatic-related	Intrusive	377.4 ± 1.7 374.4 ± 1.7 368.1 ± 1.7 366.3 ± 1.7	^{40}Ar-^{39}Ar biotite	Cooling ages of biotite in host granite and in shear zone
			345.8 ± 1.7 344.8 ± 1.7	^{40}Ar-^{39}Ar muscovite	Muscovite growth in shear zone
			1244 ± 10	U-Pb apatite TIMS	Minimum age of REE-U mineralisation
Kintyre, U	Basin-related	Unconformity-related	837 +35/-31	U-Th-Pb uraninite, electron microprobe	Age of uranium mineralisation
Oasis, U	'Metamorphic'-related	Vein or metasomatic or metamorphic	1558 ± 4	U-Pb zircon, SHRIMP	Emplacement age of host granite; maximum age of U mineralisation
			~439	^{40}Ar-^{39}Ar biotite	Minimum age of biotite formation in mylonite hosting U mineralisation
			~429	^{40}Ar-^{39}Ar muscovite	Maximum age of muscovite in mylonite zone
			433 ± 3	U-Th-Pb uraninite, electron microprobe	Age of uranium mineralisation
Mt Gee/ Armchair, U-REE	Hybrid - IOCGU	Breccia complex	360.8 ± 1.7 361.6 ± 1.5 364.6 ± 1.5	Re-Os molybdenite	Age of U mineralisation; molybdenite associated with uraninite
Maureen, U-Mo	Basin-related or magmatic-related?	Volcanic or unconformity-related	~335-342	U-Pb zircon, SHRIMP, youngest grain	Maximum depositional age of volcaniclastic rock in host sequence
			~330 ± 10	U-Pb TIMS fluorite	Possible age of fluorite and assoc uraninite
			Older than host rock	^{40}Ar-^{39}Ar muscovite	Excess Ar; age result not geologically meaningful

8.1 NOLANS BORE REE-U-TH DEPOSIT

The Nolans Bore deposit in the Aileron Province ~160km northwest of Alice Springs in the Northern Territory, is a major new REE deposit with significant U, Th and P resources, hosted mostly by fluorapatite-rich veins within Paleoproterozoic granitic gneiss which has an age of ~1806 Ma (Worden et al., 2008). The gneiss has a high grade tectonic fabric, attributed to the ~1590 Ma Chewings Orogeny, and also contains biotite-muscovite-rich mylonitic shear zones that appear to truncate mineralisation in places. Hypogene fluorapatite veins cut the high grade tectonic fabric, implying a maximum age of ~1590 Ma, but relative timing of the veins and mylonitisation is not yet well understood. An affinity of the REE-rich fluorapatite veins with alkaline magmatism is suggested, based on limited available data.

Fluorapatite-associated mineralisation has grades of 4-6 wt % rare earth oxides, whereas subordinate very high grade (7-10 wt % REO) mineralisation is associated with kaolinite in near-surface zones and is interpreted to be of secondary (surface-related) origin. Most of the REE content is hosted by cheralite and 30-40% is hosted within fluorapatite. Associated minerals include allanite, calcite, thorite, Th-Ce silicates, REE-bearing fluorocarbonates, barite, uranium silicates, and monazite.

Dating of fluorapatite by the U-Pb TIMS method has yielded an age of 1244 ± 10 Ma. This is the first age determination on mineralisation at Nolans Bore, and the result is tentatively interpreted to represent the minimum age of REE-U-Th mineralisation. Although further data are required to confirm this age, it is suggestive of a link with several other alkaline igneous events in Australia and globally during the period 1300-1130 Ma.

The micas in mylonitic shear zones within the granitic gneiss host rock yield latest Devonian to early Carboniferous ^{40}Ar-^{39}Ar ages. The biotite and muscovite ages are believed to represent mica growth during the Pertnjara Movement and Mount Eclipse Movement, respectively, of the Alice Springs Orogeny. This deformation is interpreted to have post-dated the REE-U-Th mineralisation.

8.2 KINTYRE U DEPOSIT

The timing and origins of the Kintyre U deposit in the Paterson Province of northern Western Australia have been debated since its discovery in the 1980s. Uranium mineralisation occurs as pitchblende within chlorite-carbonate-rich veins, and is associated with minor Bi, Cu, Pb, Au and PGE mineralisation. The veins are hosted by carbonaceous metasedimentary rocks of the Paleoproterozoic Rudall Complex, some tens of metres below the unconformity with the Neoproterozoic Yeneena Basin. Deposition of this basin is constrained between ~910 Ma and ~830 Ma. The Rudall Complex, mineralisation and Yeneena Basin all have been affected by the Paterson Orogeny (~650 Ma).

The uraninite age of 837 $^{+35}/_{-31}$ Ma, determined in this study by electron microprobe (EPMA) analysis of U-Th-Pb contents in the uraninite, is considered to be a reconnaissance result requiring confirmation from other methods. To our knowledge this is the first direct age determination to be published on mineralisation in the Kintyre deposit. It is widely known that the U-Pb system in uraninite is susceptible to resetting and hence this EPMA age likely represents a minimum age of uranium introduction in the deposit. Interestingly, the uraninite age of 837 $^{+35}/_{-31}$ Ma is within uncertainty of the inferred age of copper mineralisation at the Nifty deposit (~815 Ma, Huston et al., 2009), and overlaps with both the possible period of Yeneena Basin deposition and with the ~850-800 Ma Miles Orogeny (Huston et al., 2009). An age of ~840 Ma for uranium mineralisation at Kintyre is also consistent with previous proposals that this is an unconformity-related deposit,

because the Yeneena Basin would appear to have been present at the time of mineralisation. However, the data are permissive of other possible origins, and tighter age constraints are necessary before further conclusions can be drawn on the relative timing of mineralisation and regional basin and deformation events.

8.3 OASIS U DEPOSIT

The Oasis U deposit is situated in the Etheridge Province of northern Queensland, hosted by the Mesoproterozoic Mywyn Granite. Mineralisation occurs within a mylonitic biotite-rich shear zone that cuts the granite, and comprises uraninite with traces of coffinite, thorite, allanite, apatite, pyrite, hematite, Ca-REE-fluorocarbonates, zircon and galena. The uraninite appears to have overgrown and replaced the biotite in places. Whole rock geochemistry and mass-balance calculations indicate net gains of U, Na, Mg, Ti, Th, Bi and LREE, with concomitant losses of K, Ca, Rb, Sr and Ba in the mineralisation and adjacent alteration zones.

No previous age determinations have been reported for the Oasis deposit. The newly determined U-Pb SHRIMP age of igneous zircons in the Mywyn Granite (1559 ± 3 Ma, Neumann and Kositcin, in prep.) provides a maximum age of uranium mineralisation at the Oasis deposit. However, the consistency of the EPMA chemical age of uraninite reported herein (433 ± 3 Ma) with the ^{40}Ar-^{39}Ar ages of micas in the host shear zone (~429-439 Ma) strongly suggests that uranium mineralisation was formed in the mid-Silurian, or was at least reconstituted at this time during a significant thermal and deformation event. It is possible this event corresponds to the Benambran Orogeny (Champion et al., 2009). The proposed age for the Oasis deposit is significantly older than that of the Maureen U-Mo deposit in the same geological region (Table 8.1).

8.4 MT GEE-ARMCHAIR U-REE DEPOSITS

Iron oxide-rich hydrothermal alteration and U-REE mineralisation in the Mt Gee – Armchair – Mt Painter district is hosted by mainly Mesoproterozoic meta-igneous rocks of the Mt Painter Inlier, northeastern South Australia. Ordovician intrusive rocks are also present but the relationship with U mineralisation has not been understood. Uraninite is intimately associated with monazite (the main REE host) and minor molybdenite in some parts of the hydrothermal system (e.g., Armchair deposit). The primary U-REE-Mo mineralisation is closely associated with chlorite-hematite alteration and brecciation that overprinted early hydrothermal magnetite at the Armchair deposit. Although this mineralogy is similar to that in some iron-oxide Cu-Au systems (Williams et al., 2005), the Mt Gee – Armchair – Mt Painter district appears to lack significant Cu-Au mineralisation as far as is known.

Three Re-Os ages for molybdenite in the Armchair deposit are just outside analytical uncertainty of one another, between 360.8 ± 1.7 Ma and 364.6 ± 1.5 Ma. Textural relationships suggest the molybdenite formed synchronously with uraninite and hence these ages are interpreted to represent the age of uranium mineralisation. These late Devonian ages are at variance with the ages of any known magmatism in the Mt Painter Province, and postdate the known Ordovician magmatism by ~80 m.y. They are also younger than imprecise ages on uraninite (400 ± 50 Ma, Kleeman 1946) and on monazite (440 ± 50 Ma, Pidgeon, 1979), but are supported by a U-Pb age for brannerite of 367 ± 13 Ma from the Hidden Valley prospect elsewhere in the Mt Painter Province (Wülser, 2009).

If U-REE mineralisation at Mt Gee-Armchair formed in the late Devonian as proposed herein, it may be partly synchronous with the Kanimblan Orogeny and associated thermal effects, which are known to have affected wide regions of eastern Australia (Champion et al., 2009). Effects of this orogeny have not been previously recognised in the Mt Painter Province. If the Mt Gee-Armchair U-REE deposits have affinities with the IOCG deposit class, these would represent the first known IOCG-related mineralisation recognised in the Paleozoic of eastern Australia.

8.5 MAUREEN U-MO DEPOSIT

Uranium mineralisation at the Maureen deposit is hosted mainly by Paleozoic fluvial sandstones and conglomerates in the lower ~100m of a basin sequence including tuffs and volcaniclastic rocks. The basin unconformably overlies Mesoproterozoic basement comprising metasedimentary rocks and dolerite. Uranium (uraninite) and Mo (jordisite) mineralisation occurs as replacements and veins in the Paleozoic clastic rocks, and to a much lesser extent within shears in the basement immediately below the unconformity. Associated minerals include fluorite, arsenopyrite, arsenian pyrite, sphalerite, dickite, chamosite, goyazite, anatase and carbon (Mathison and Hurtig, 2009; this study).

No previous dating has been undertaken on the Maureen deposit. The current study was carried out to compare the age of mineralisation with that of the host rocks, thereby shedding light on the origin of the deposit. Only limited U-Pb zircon data were obtained on the sedimentary host rocks, and a maximum depositional age of ~342-335 Ma was determined (full results reported by Neumann and Kositcin, in prep.). Fluorite yielded a TIMS U-Pb age of ~330 ± 10 Ma which is interpreted to represent a possible age of the U-Mo mineralisation associated with the fluorite. These age constraints do not discriminate between alternative volcanic-associated and unconformity-related models of mineralisation origin.

8.6 IMPLICATIONS

New constraints on the age of magmatic-related REE-U-Th mineralisation in the Nolans Bore deposit indicate a minimum age of 1244 ± 10 Ma and a maximum age of ~1590 Ma. Further work is in progress to tighten these constraints. Nevertheless, this result opens the possibility of undiscovered U and related mineralisation elsewhere in the North Australian Craton, associated with alkaline(?) igneous activity in the early to mid Mesoproterozoic. Given the current exploration interest in REE, U and Th resources, the new age constraints should be of use in developing regional exploration targeting criteria.

Unconformity-related U deposits are best known globally where they are spatially associated with early Mesoproterozoic clastic basins in Saskatchewan, Canada (Athabasca Basin) and in the Pine Creek region of the Northern Territory (Kombolgie Basin; Cuney and Kyser, 2008). The new results from the Kintyre deposit in the Paterson Province of Western Australia show that deposits of this general style are not restricted to early Mesoproterozoic settings. However, it should be noted that comprehensive descriptions of the Kintyre deposit and its setting are not yet available in the public domain, and hence its affinity with unconformity-related deposits remains to be clarified. Neoproterozoic settings comparable to that at Kintyre are present in other parts of Australia including the Adelaide Geosyncline, and the potential for uranium here is significant. An assessment of this potential will be reported elsewhere (Huston et al., in prep.).

The Maureen U-Mo deposit is an example of mineralisation not easily ‘pidgeon holed’ into conventional classification schemes, as it shares characteristics of both ‘volcanic’ and ‘unconformity-related’ deposit types. Although the new age constraints reported herein do not allow

us to distinguish between these two deposit types, the results do point to the potential for Paleozoic uranium deposits with characteristics similar to those of the better known Proterozoic unconformity-related deposits. Many of the same processes may have been shared in the Maureen system and the older unconformity-related deposits and indeed with other basin-related uranium systems (Skirrow et al., 2009). The factors that control the size and grade of such deposits arguably are still not well understood, but the age of the system may not be as important as previously assumed.

True 'metamorphic' uranium deposits appear to be rare (Cuney and Kyser, 2008), and many of the uranium deposits that formed in metamorphic rocks at elevated pressure-temperature conditions are most likely the products of fluids of exotic origin, such as modified magmatic-hydrothermal or basinal fluids. This was probably the case at the Oasis deposit where a syn-Benambran orogeny age has been determined in this study. Clearly this mineralisation is different in style and age to that at the Maureen deposit.

The Mt Gee-Armchair U-REE deposits probably have affinities with iron oxide-Cu-Au (IOCG) systems, representing a possible iron oxide-uranium (IOU) end-member within the IOCG deposit family which is itself a hybrid class (Skirrow et al., 2009). Hitzman and Valenta (2005) alluded to this possibility although Mt Gee was not mentioned. The reason for the apparent lack of significant copper and gold mineralisation in the Mt Gee and Armchair systems is not understood. Our dating of molybdenite associated with uraninite at the Armchair deposit indicates a late Devonian age, more than 1 billion years younger than IOCG systems in the Gawler Craton and Curnamona Province. At this time, there was apparently no active magmatism in the Mt Painter Inlier, perhaps influencing the metal contents of the IOU deposits.

ACKNOWLEDGEMENTS

Arafura Resources, Marathon Resources, Cameco Australia, and Mega Uranium are thanked for providing access to sample material, discussions, and for permission to publish the results.

Staff in the Geoscience Australia mineral separation laboratory, led by Chris Foudoulis, are thanked for providing high quality mineral separates for geochronology. The SEM work was carried with assistance from the Geochronology Laboratory staff at Geoscience Australia, and in particular we wish to thank Patrick Burke. Paulo Vasconcelos and David Thiede are thanked for sample handling and analyses of the $^{40}Ar/^{39}Ar$ geochronology samples at the University of Queensland AGES laboratory.

REFERENCES

Alexandre, P., Kyser, K. and Polito, P., 2005. Alteration mineralogy and stable isotope geochemistry of Paleoproterozoic basement-hosted unconformity-type uranium deposits in the Athabasca basin. *Economic Geology* **100**, 1547-1563

Bagas, L., and Nelson, D.R., 2007. Provenance of Neoproterozoic sedimentary rocks in the northwest Paterson Orogen, Western Australia. *Central Australian Basins Symposium Special Publication*. Northern Territory Geological Survey.

Bain, J.H.C., 1977. Uranium mineralisation associated with late Palaeozoic acid magmatism in northeast Queensland. *Bureau of Mineral Resources Journal of Geology and Geophysics*, **1**, 137-147.

Bakker, R.J. and Elburg, M.A., 2006. A magmatic-hydrothermal transition in Arkaroola (northern Flinders Ranges, South Australia): from diopside-titanite pegmatites to hematite-quartz growth. *Contributions to Mineralogy and Petrology*, doi: 10.1007/s00410-006-0125-0.

Bendall, B., Hand, M. and Foden, J., 1998. Sm-Nd evidence for mid-Paleozoic regional amphibolite facies metamorphism in the Strangways Range, central Australia. *Geological Society of Australia Abstracts,* **49**, 27.

Bowles, J.F.W., 1990. Age dating of individual grains of uraninite in rocks from electron microprobe analysis. *Chemical Geology*, **83**, 47-53.

Cartwright, I., Buick, I. S., Foster, D. A. and Lambert, D. D., 1999. Alice Springs age shear zones from the southeastern Reynolds Range, central Australia. *Australian Journal of Earth Sciences*, **46**, 355 – 363.

Champion, D.C., Kositcin, N., Huston, D.L., Mathews, E. and Brown, C. 2009. Geodynamic Synthesis of the Phanerozoic of eastern Australia and Implications for metallogeny. *Geoscience Australia Record* **2009/18**, 255pp.

Claoué-Long, J., Edgoose, C. and Worden, K., 2008. A correlation of Aileron Province stratigraphy in central Australia. *Precambrian Research,* **166**, 230-245.

Collins, W.J. and Williams, I.S., 1995. SHRIMP ion probe dating of short-lived Proterozoic tectonic cycles in the northern Arunta Inlier, central Australia. *Precambrian Research,* **71**, 69-83.

Cuney, M. and Kyser, K., 2008. Recent and not-so-recent developments in uranium deposits and implications for exploration. *Mineralogical Association of Canada Shortcourse Series*, Quebec City, May 2008, **39**.

Cuney, M., 2009. The extreme diversity of uranium deposits. *Mineralium Deposita*, **44**, 3-9, DOI: 10.1007/s00126-008-0223-1.

Denaro, T.J., Withnall, I.W., Bain, J.H.C., and Mackenzie, D.E., 1997. Mineral resource assessment, Georgetown-Croydon area. *Queensland Minerals and Energy Review Series* 1997, 228pp.

Drexel, J.F. and Major, R.B., 1987. Geology of the uraniferous breccias near Mount Painter, South Australia, and revision of rock nomenclature. *Quarterly Geological Notes of the Geological Survey of South Australia* ,**104**, 14-24.

Drexel, J.F. and Major, R.B., 1990. Mount Painter uranium – rare earth deposits. *In:* Hughes, F.E. (ed.), Geology of the Mineral Deposits of Australia and Papua New Guinea, p. 993-998. *Australian Institute of Mining and Metallurgy*, Melbourne.

Elburg, M.A., Bons, P.D., Foden, J. and Brugger, J., 2003. A newly defined Late Ordovician magmatic-thermal event in the Mount Painter Province, northern Flinders Ranges, South Australia. *Australian Journal of Earth Sciences*, **50**, 611-631.

Fanning, C.M., Teale, G.S., and Robertson, R.S., 2003. Is there a Willyama Supergroup sequence in the Mt Painter Inlier? In: Peljo, M. (compiler), Broken Hill Exploration Initiative: Abstracts from the July 2003 conference. *Geoscience Australia Record* **2003/13**, 38-41.

Foden, J., Sandiford, M., Dougherty-Page, J. and Williams, I., 1999. Geochemistry and geochronology of the Rathjen gneiss: implications for the early tectonic evolution of the Delamerian Orogen. *Australian Journal of Earth Sciences*, **46**, 377-389.

Förster, H.-J., 1999. The chemical composition of uraninite in Variscan granites of the Erzgebirge, Germany. *Mineralogical Magazine*, **63**(**2**), 239-252.

Fraser, G.L. and Neumann, N.L., 2010. New SHRIMP U-Pb zircon ages from the Gawler Craton and Curnamona Province, South Australia, 2008-2010. *Geoscience Australia Record* **2010/16**, 256p.

Gatehouse, C.G., Fanning, C.M. and Flint, R.B., 1995. Geochronology of the Big Lake Suite, Warburton Basin, northeastern South Australia. *Queensland Geological Notes*, **128**, 8-16.

Hitzman, M.W. and Valenta, R.K., 2005. Uranium in iron oxide-copper-gold (IOCG) systems. *Economic Geology*, **100**, 1657-1661.

Hurtig, N., 2008. Maureen, a Paleozoic unconformity-related U-Mo-F deposit, Queensland, Australia. Unpublished M.Sc. thesis, ETH Zurich.

Huston D. L., Maas R. & Czarnota K. 2007. The age and genesis of the Nifty copper deposit: back to the future. *Geoscience Australia Professional Opinion 2007/03*, 26 pp.

Huston, D.L., Maas, R., Miggins, D., Maidment, D.W., Czarnota, K., Preiss, W. & Cassidy, K., 2009. Neoproterozoic mineralisation in Australia: timing and geodynamic setting. Proceedings of the 10th Biennial SGA Meeting. *In: Proceeding of the 10th Biennial SGA Meeting of the Society for Geology Applied to Mineral Deposits*, Townsville, Australia, 285-287.

Idnurm, M. and Heinrich, C.A., 1993. A paleomagnetic study of hydrothermal activity and uranium mineralization at Mt Painter, South Australia. *Australian Journal of Earth Sciences*, **40**, 87-101.

Jackson, D.J. and Andrew, R.L., 1990. Kintyre uranium deposit. *In:* Hughes FE. (ed.), *Geology of the Mineral Deposits of Australia and Papua New Guinea*. The Australasian Institute of Mining and Metallurgy**,** 653-658.

Jaques, A.L., 2008. Australian carbonatites: their resources and geodynamic setting. 9th International Kimberlite Conference, extended abstract No. 9IKC-A-00347.

Kempe, U., 2003. Precise electron probe age determination in altered uraninite: consequences on the intrusion age and the metallogenic significance of the Kirchberg granite (Erzgebirge. Germany). *Contributions to Mineralogy and Petrolog,y* **145**, 107-118.

Kleeman, A.W., 1946. An age determination on samarskite from Mount Painter, South Australia. *Transactions of the Royal Society of South Australia*, **70**, 175-177.

Komninou, A. and Sverjensky, D.A., 1995. Hydrothermal alteration and the chemistry of ore-forming fluids in an unconformity-type uranium deposit. *Geochimica et Cosmochimica Acta* **59**, 2709-2723.

Kuiper, K.F., Deino, A., Hilgen, F.J., Krijgsman, W., Renne, P.R. and Wijbrans, J.B., 2008. Synchronizing Rock Clocks of Earth History. *Science*, **320**, 500-504.

Lambert, I.B., Drexel, J.F., Donnelly, T.H. and Knutson J., 1982. Origin of breccias in the Mount Painter area, South Australia. *Journal of the Geological Society of Australia*, **29**, 115-125.

Maas, R., Kamenetsky, M.B., Sobolev, A.V., Kamenetsky, V.S. and Sobolev, N.V., 2005. Sr-Nd-Pb isotopic evidence for a mantle origin of alkali chlorides and carbonates in the Udachnaya kimberlite, Siberia. *Geology* **35**, 549-552.

Marathon Resources, 2009. Annual Report, www.marathonresources.com.au.

Markey, R., Stein, H.J., Hannah, J.L., Selby, D. and Creaser, R.A., 2007. Standardizing Re-Os geochronology: A new molybdenite Reference Material (Henderson, USA) and the stoichiometry of Os salts. *Chemical Geology*, **244**, 74-87.

Mathison, I. and Hurtig, H.C., 2009. The Maureen U-Mo-F deposit. *Australian Institute of Geoscientists Bulletin*, **49**, 85-88.

McKay, A.D. and Miezitis, Y., 2001. Australia's uranium resources, geology and development of deposits. *AGSO-Geoscience Australia, Mineral Resource Report* **1**, 184 pp.

McLaren, S., Dunlap, W.J., Sandiford, M. and McDougall, I., 2002. Thermochronology of high heat-producing crust at Mount Painter, South Australia: implications for tectonic reactivation of continental interiors. *Tectonics*, **21(4)**, doi: 10.1029/2000TC001275.

McLaren, S., Sandiford, M., Powell, R., Neumann, N. and Woodhead, J., 2006. Paleozoic intraplate crustal anatexis in the Mount Painter Province, South Australia: Timing, thermal budgets and the role of crustal heat production. *Journal of Petrology*, doi: 10.1093/petrology/eg1044.

Montel, J.-M., Foret, S., Veschambre, M., Nicollet, C. and Provost, A., 1996. Electron microprobe dating of monazite. *Chemical Geology*, **131**, 37–53.

Morrison, G.W. and Beams, S.D. 1995. Geological setting and mineralisation style of ore deposits of Northeast Queensland. *In:* Beams, S.D. (ed/compiler), Mineral Deposits of Northeast Queensland: Geology and Geochemistry. 17th International Geochemical Exploration Symposium Exploring the Tropics. James Cook University of North Queensland, *Contributions of the Economic Geology Research Unit*, **52**, 1-32.

Neumann, N. and Kositcin, N., in prep. New SHRIMP U-Pb zircon ages from North Queensland 2007 – 2010. *Geoscience Australia Record*.

Neumann, N.L., Sandiford, M. and Foden, J., 2000. Regional geochemistry and continental heatflow: Implications for the origin of the South Australian heat flow anomaly. *Earth & Planetary Science Letters*, **183**, 107-120.

Ogilvie, J.M., 2006. U-Pb detrital zircon dating of structural and stratigraphic relationships within Hidden Valley, Mount Painter Inlier, Northern Flinders Ranges: Implications for Proterozoic crustal evolution of Eastern Australia. Honours Thesis, Monash University, unpublished.

Page, R.W., Compston, W. and Needham, R.S., 1980. Geochronology and evolution of the late-Archean basement and Proterozoic rocks in the Alligator Rivers uranium field, Northern Territory, Australia. *In:* Ferguson, J. and Goleby, A.B. (eds.), Uranium in the Pine Creek Geosyncline. *Proceedings of the International Uranium Symposium on the Pine Creek Geosyncline*. International Atomic Energy Agency, Vienna, 39–68.

Paul, E.G., Flottmann, T. and Sandiford, M., 1999. Structural geometry and controls on basement-involved deformation in the northern Flinders Ranges, Adelaide fold belt, South Australia. *Australian Journal of Earth Sciences*, **46**, 343-354.

Pidgeon, R.T., 1979. Report on the U-Pb age of monazite samples 930, 931 and 932 (from the Mount Painter area). South Australian Department of Mines and Energy, Open File Envelope.

Pidgeon, R.T., Smith, C.B., and Fanning, C.M., 1989. Kimberlite and lamproite emplacement ages in Western Australia. *Geological Society of Australia Special Publication* **14**, 369-381.

Plant, J.A., Simpson, P.R., Smith, B. and Windley, B.F., 1999. Uranium ore deposits: products of the radioactive earth. *Reviews in Mineralogy and Geochemistry*, **38**, 255-319.

Polito, P.A., Kyser, T.K., Thomas, D., Marlatt, J. and Drever, G., 2005. Re-evaluation of the petrogenesis of the Proterozoic Jabiluka unconformity-related uranium deposit, Northern Territory, Australia. *Mineralium Deposita*, **40**, 257-288.

Pommier, A., Cocherie, A. and Legendre, O., 2002. EPMA Dating User's Manual: Age calculation from Electron Probe Microanalyser Measurements of U–Th–Pb. BRGM, France, 9 pp.

Ren, Y., Zhan, Y. and Zhan, Z., 1994. Study on the heat events of ore-forming Bayan Obo deposit. *Acta Geoscientia Sinica*, **1**, 95-101.

Renne, P.R., Cassata, W.S. and Morgan, L.E., 2009. The isotope composition of atmospheric argon $^{40}Ar/^{39}Ar$ geochronology: Time for a change? *Quaternary Geology*, **4,** 288 – 298.

Richards, D., 2006. Significant new uranium drill intersections at Oasis. Glengarry Resources Report to the Australian Stock Exchange, 3rd August 2006, 5 pp.

Rubatto, D., Williams, I.S. and Buick, I.S., 2001. Zircon and monazite response to prograde metamorphism in the Reynolds Range, central Australia. *Contributions to Mineralogy and Petrology*, **140**, 458–468.

Scrimgeour, I. and Raith, J., 2001. Tectonic and thermal events in the northeastern Arunta Province. *Northern Territory Geological Survey, Report* 12.

Selby, D. and Creaser, R.A., 2004. Macroscale NTIMS and microscale LA-MC-ICP-MS Re-Os isotopic analysis of molybdenite: Testing spatial restrictions for reliable Re-Os age determinations, and implications for the decoupling of Re and Os within molybdenite. *Geochimica et Cosmochimica Acta*, **68**, 3897-3908.

Smith, J., 2001. Joint NTGS-AGSO age determination program 1999-2001. *Northern Territory Geological Survey Record* **2001-007**.

Smith, M. and Wu, C.-Y., 2000. The geology and genesis of the Bayan Obo Fe-REE-Nb deposit: a review. *In:* Porter, T. M. (ed.), Hydrothermal iron oxide copper-gold and related deposits: a global perspective. Adelaide, Australian Mineral Foundation, 271-281.

Smoliar, M.I., et al., 1996. Re–Os isotope constraints on the age of Group IIA, IIIA, IVA, and IVB iron meteorites, *Science*, **271**, 1099 – 1102.

Steiger, R.H. and Jaeger, E., 1977. Subcommission on geochronology: Convention on the use of decay constants in geo- and cosmochemistry. *Earth and Planetary Science Letters*, **36**, 359 – 362.

Stewart, A.J., 1981. 1:100 000 geological map commentary, Reynolds Range region, Northern Territory. Canberra, Bureau of Mineral Resources, Geology and Geophysics, 12 p.

Suzuki, K. and Adachi, M., 1991. Precambrian provenance and Silurian metamorphism of the Tsubonnsawa paragneissin the South Kitakami terrane, Northeast Japan, revealed by the chemical Th–U–total–Pb isochron ages of monazite, zircon and xenotime. *Geochemical Journal*, **25**, 357–376.

Suzuki, K., Shimizu, H. and Masuda, A., 1996. Re-Os dating of molybdenites from ore deposits in Japan: Implications for the closure temperature of the Re-Os system for molybdenite and the cooling history of molybdenum ore deposits. *Geochimica et Cosmochimica Acta*, **60(16)**, 3151-3159.

Teale, G.S., and Lottermoser, B.G., 1987. Paleozoic granites of the Umberatana region, South Australia: the role of volatiles in the crystallization of some alkaline-peralkaline granites. *Geologische Rundschau*, **76(3)**, 857-868.

Thomas, M. and Walter, M.R., 2002. Application of hyperspectral infrared analysis of hydrothermal alteration on Earth and Mars. *Astrobiology*, **2(3)**, 335-351.

Vos, I.M.A., Bierlein, F.P. and Heithersay, P.S., 2007. A crucial role for slab break-off in the generation of major mineral deposits: insights from central and eastern Australia. *Mineralium Deposita*, **42**, 515-522, doi: 10.1007/s00126-007-0137-3.

Vry, J., Compston, W. and Cartwright, I., 1996. SHRIMP II dating of zircons and monazites: reassessing the timing of high-grade metamorphism and fluid flow in the Reynolds Range, north Arunta block, Australia. *Journal of Metamorphic Geology*, **14**, 335-350.

Wall, V.J., 2006. Unconformity-related uranium systems: Downunder and over the top. *Geological Society of Australia Abstracts*, **82**, 4.

Wilde, A.R., Mernagh, T.P., Bloom, M.S. and Hoffmann, C., 1989. Fluid includion evidence on the origin of some Australian unconformity-related uranium deposits. *Economic Geology* **84**, 1627-1642.

Williams, I.S., Buick, I.S., and Cartwright, I., 1996. An extended episode of early Mesoproterozoic metamorphic fluid flow in the Reynolds Range, central Australia. *Journal of Metamorphic Geology*, **14**, 29-47.

Withnall, I.W., Mackenzie, D.E., Denaro, T.J., Bain, J.H.C., Oversby, B.S., Knutson, J., Donchak, P.J.T., Champion, D.C., Wellman, P., Cruikshank, B.I., Sun, S.S. and Pain, C.F. 1997. Georgetown Region. *In:* Bain, J.H.C. and Draper, J.J. (eds) North Queensland Geology. Australian Geological Survey Organisation Bulletin 240 and Queensland Department of Mines and Energy Geology 9, 19-69.

Woodhead, J.D., Hellstrom, J., Maas, R., Drysdale, R., Zanchetta, G., Devine, P. and Taylor, E., 2006. U-Pb geochronology of speloethems by MC-ICPMS. *Quaternary Geochronology* 1, 208-221.

Worden, K.E., Carson, C.J., Close, D.F., Donnellan, N. and Scrimgeour, I.R., 2008. Summary of results. Joint NTGS-GA geochronology: Tanami Region, Arunta Region, Pine Creek Orogen and Halls Creek Orogen correlatives, January 2005 – March 2007. *Northern Territory Geological Survey Record*, **2008-003**.

Wülser, P.-A., 2009. Uranium metallogeny in the north Flinders Ranges region of South Australia. Unpublished Ph.D. thesis, Department of Geology and Geophysics, The University of Adelaide, South Australia.

Youles, I.P., 1970. Report on SML 145A for six months ending January 16th, 1970. Department of Mines and Energy South Australia, Open File Envelope 3633, unpublished.

Youles, I.P., 1975. Comparison of Olympic Dam copper-uranium deposit and Mount Painter uranium deposits. *Department of Mines and Energy South Australia, Report Book* **78/85**, unpublished.

Young, D.N., Fanning, C.M., Shaw, R.D., Edgoose, C., Blake, D.H., Page, R.W. and Camacho, A., 1995. U-Pb zircon dating of tectonomagmatic events in the northern Arunta Inlier, central Australia. *Precambrian Research*, **71**, 45-68.

Zachariáš J., Adamovič J. and Konečny P. 2008. The uraninite-pyrite association, a sensitive indicator of changes in Paleofluid composition: An example from the Ohre (Eger) Graben, Bohemian Massif, Czech Republic. *The Canadian Mineralogist* **46**, 1159-1172.

Zhang, Z., Tang, S. and Wang, J., 1994. New data for ore-forming age of the Bayan Obo REE ore deposit, Inner Mongolia. *Acta Geoscientia Sinica*, **1**, 85-94.

Appendix 1. U-Pb isotope results for Nolans Bore apatite sample #25.

sample	weight (mg)	U (ppm)	Pb (ppm)	$^{232}Th/^{238}U$	Pb_{tot} (ng)	Pb_c (ng)	206/204 (a)	207/204 (a)	208/204 (a)	206/238 (b)	± (2σ)	207/235 (b)	± (2σ)	207/206 (b)	± (2σ)	$^{206}Pb/^{238}U$ Age (Ma)	± (2σ)	$^{207}Pb/^{235}U$ Age (Ma)	± (2σ)	$^{207}Pb/^{206}Pb$ Age (Ma)	± (2σ)	Disc. (c) %	rho 6-8 vs 7-5
NB25.5 ap	0.39	376.3	429.3	17.4	167.4	22.0	88.44	21.36	408.8	0.18219	0.186	2.0616	0.67	0.08207	0.61	1078.9	2.0	1136.1	7.6	1247	12	13.5	0.46
NB25.6 ap	0.28	505.0	411.1	17.3	115.1	16.0	87.77	21.31	402.3	0.13041	0.188	1.4789	0.68	0.08225	0.61	790.2	1.5	921.8	6.2	1251	12	36.8	0.46
NB25.7 ap	0.22	688.9	766.5	17.4	168.6	23.0	88.43	21.35	407.8	0.17774	0.238	2.0093	0.69	0.08199	0.61	1054.6	2.5	1118.6	7.7	1245	12	15.3	0.48
NB25.8 ap	0.22	224.6	266.0	17.3	58.5	7.9	88.27	21.33	405.5	0.18970	0.179	2.1438	0.67	0.08196	0.61	1119.7	2.0	1163.0	7.8	1245	12	10.1	0.46

Notes

Data reduction done using PBDAT 1.24 (Ludwig, 1993)

model $^{232}Th/^{238}U$ estimated from radiogenic 208/206 and upper intercept age of 1240 Ma

Pb_{tot} is total Pb, Pb_c is common Pb; in nanogram

(a) corrected for mass bias, spike and blank

(b) corrected for mass bias, blank and common Pb; errors in %

errors for Pb/U and Pb/Pb ages in Ma

(c) degree of discordance (normal) expressed as % (Disc% = 100*(207/206age - 206/238age) / 207/206age)

blank: 50±25 pg Pb, 5 ±2.5 pg U, blank isotopic composition: $^{206}Pb/^{204}Pb$ 17.05±0.2, $^{207}Pb/^{204}Pb$ 15.50±0.20, $^{208}Pb/^{204}Pb$ 36.82±0.20; errors 2sigma absolute

common Pb correction: 1200 Ma Pb from Stacey-Kramers Pb growth curve

Appendix 2. Tabulated $^{40}Ar/^{39}Ar$ data for samples from the Nolans Bore deposit, Northern Territory.

Step #	$^{36}Ar/^{39}Ar$	± (1σ)	$^{37}Ar/^{39}Ar$	± (1σ)	$^{38}Ar/^{39}Ar$	± (1σ)	$^{40}Ar/^{39}Ar$	± (1σ)	$^{40}Ar^*/^{39}Ar$	± (1σ)	$\%^{40}Ar^*$	± (1σ)	Age (Ma)	± (1σ)	^{39}Ar Moles	^{40}Ar Moles
2007080001-10 Biotite, J = 0.011009 ± 0.000018 (1σ)																
Aliquot 1																
1	0.00239	0.00012	0.0074	0.0071	0.00729	0.00044	20.732	0.08	20.018	0.087	96.56	0.29	359.3	1.4	4.24E-16	8.79E-15
2	0.000258	0.000059	-0.001	0.0031	0.00605	0.00052	21.114	0.068	21.035	0.07	99.63	0.15	375.8	1.1	9.16E-16	1.93E-14
3	0.00046	0.000091	0.0097	0.0046	0.0059	0.00044	21.298	0.084	21.16	0.088	99.36	0.21	377.8	1.4	5.72E-16	1.22E-14
4	0.00009	0.00011	0.0002	0.0066	0.00784	0.00036	21.354	0.076	21.328	0.083	99.88	0.24	380.5	1.3	3.84E-16	8.19E-15
5	0.00035	0.00012	0.0069	0.0064	0.00606	0.00069	21.246	0.084	21.142	0.091	99.51	0.26	377.5	1.5	4.07E-16	8.64E-15
6	0.00008	0.00019	0.0045	0.0058	0.00781	0.00046	21.065	0.083	21.04	0.1	99.88	0.35	375.8	1.6	4.14E-16	8.72E-15
7	0.0005	0.00014	0.002	0.008	0.008	0.00049	21.213	0.09	21.061	0.099	99.29	0.29	376.2	1.6	3.37E-16	7.16E-15
8	0.0002	0.00017	0.016	0.0094	0.00939	0.00045	21.09	0.11	21.03	0.12	99.72	0.29	375.7	1.9	2.52E-16	5.30E-15
9	0.00008	0.00024	0.007	0.012	0.00537	0.00065	21.36	0.12	21.34	0.14	99.88	0.4	380.7	2.2	2.21E-16	4.73E-15
10	0.0008	0.00047	0.006	0.016	0.00413	0.00059	21.48	0.14	21.23	0.2	98.88	0.7	379	3.2	1.60E-16	3.44E-15
Aliquot 2																
1	0.00183	0.00012	0.0015	0.0055	0.01352	0.00028	20.273	0.076	19.725	0.084	97.3	0.25	354.5	1.4	4.62E-16	9.37E-15
2	0.000095	0.000098	0.0015	0.0037	0.01383	0.00022	20.941	0.072	20.912	0.077	99.87	0.2	373.8	1.2	9.53E-16	2.00E-14
3	0.00005	0.00015	0.0025	0.0047	0.01308	0.00026	20.952	0.079	20.936	0.09	99.93	0.3	374.2	1.5	5.31E-16	1.11E-14
4	0.00045	0.00011	0.0002	0.0062	0.01348	0.0003	21.234	0.083	21.099	0.089	99.37	0.23	376.8	1.4	4.55E-16	9.66E-15
5	0.00035	0.00011	-0.002	0.0099	0.01309	0.00022	21.085	0.09	20.979	0.095	99.5	0.31	374.9	1.5	4.28E-16	9.03E-15
6	0.00005	0.00014	-0.0066	0.0076	0.01275	0.00031	20.984	0.094	20.97	0.1	99.93	0.28	374.7	1.6	3.50E-16	7.34E-15
7	0.00012	0.00015	-0.0048	0.0074	0.01348	0.00035	20.929	0.087	20.893	0.097	99.83	0.31	373.5	1.6	3.16E-16	6.61E-15
8	0.00002	0.0002	-0.002	0.012	0.01397	0.0005	20.973	0.098	20.97	0.11	99.98	0.33	374.7	1.8	2.12E-16	4.45E-15
9	0.00028	0.00026	-0.019	0.014	0.01271	0.00054	20.871	0.095	20.78	0.12	99.59	0.41	371.7	2	1.93E-16	4.03E-15
10	0.00074	0.00047	-0.021	0.015	0.01415	0.00061	21.09	0.13	20.86	0.19	98.94	0.71	373	3	1.67E-16	3.52E-15
2007080001-11 Biotite, J = 0.011009 ± 0.000018 (1σ)																
Aliquot 1																
1	0.00048	0.00017	0.0037	0.0032	0.00811	0.00047	20.455	0.073	20.312	0.089	99.31	0.29	364.1	1.4	7.14E-16	1.46E-14
2	0.000199	0.000036	0	0.0017	0.00737	0.00028	20.601	0.058	20.54	0.059	99.71	0.13	367.78	0.96	1.49E-15	3.06E-14
3	0.000196	0.000074	0.0035	0.0036	0.00589	0.00054	20.669	0.091	20.609	0.093	99.72	0.2	368.9	1.5	6.24E-16	1.29E-14
4	0.00033	0.00017	0.002	0.0058	0.0076	0.0003	20.769	0.074	20.67	0.091	99.53	0.31	369.9	1.5	4.39E-16	9.12E-15
5	0.00038	0.00011	0.0011	0.0057	0.00678	0.00049	20.632	0.084	20.517	0.09	99.44	0.27	367.4	1.5	4.39E-16	9.07E-15
6	0.0003	0.00012	0.0073	0.0061	0.00674	0.00053	20.667	0.085	20.577	0.092	99.57	0.27	368.4	1.5	3.78E-16	7.81E-15
7	0.00002	0.00016	0.0008	0.0097	0.00609	0.00059	20.595	0.086	20.588	0.098	99.97	0.3	368.6	1.6	2.68E-16	5.51E-15
8	0.00054	0.00022	0.007	0.012	0.00372	0.00066	20.45	0.11	20.29	0.13	99.22	0.4	363.7	2	1.91E-16	3.90E-15
9	0.00015	0.00022	-0.005	0.013	0.00662	0.00049	20.54	0.1	20.49	0.12	99.78	0.37	367	1.9	1.99E-16	4.09E-15
10	0.00008	0.00014	-0.0164	0.0088	0.00737	0.00046	20.707	0.099	20.68	0.11	99.88	0.28	370.1	1.7	2.92E-16	6.05E-15
Aliquot 2																
1	0.0003	0.00019	0.0089	0.0091	0.00718	0.0005	20.51	0.11	20.42	0.12	99.56	0.34	365.8	1.9	2.28E-16	4.67E-15
2	0.000238	0.000075	0.0051	0.0031	0.00676	0.00053	20.533	0.085	20.461	0.088	99.65	0.17	366.5	1.4	6.37E-16	1.31E-14
3	0.0002	0.00015	0.0263	0.0092	0.00688	0.0005	20.563	0.092	20.5	0.1	99.72	0.26	367.2	1.7	2.43E-16	4.99E-15
4	0.00062	0.00014	0.013	0.0073	0.00683	0.00046	20.708	0.091	20.52	0.1	99.11	0.35	367.5	1.6	3.02E-16	6.26E-15
5	0.00032	0.00012	0.0177	0.0055	0.00949	0.00043	20.428	0.084	20.334	0.091	99.54	0.28	364.4	1.5	3.43E-16	7.00E-15
6	0.00062	0.00021	0.032	0.011	0.00649	0.00043	20.84	0.12	20.65	0.14	99.12	0.38	369.6	2.2	2.15E-16	4.48E-15
7	0.00083	0.00028	0.048	0.015	0.00813	0.00074	20.61	0.12	20.37	0.15	98.81	0.48	364.9	2.4	1.54E-16	3.17E-15
8	0.00066	0.00028	0.027	0.016	0.00924	0.0007	20.34	0.15	20.14	0.17	99.04	0.48	361.4	2.8	1.38E-16	2.81E-15
9	0.00148	0.00062	0.061	0.034	0.0057	0.0012	21.4	0.24	20.97	0.3	97.96	0.98	374.7	4.8	6.19E-17	1.33E-15
10	-0.00041	0.0007	-0.033	0.04	0.0077	0.0014	21.08	0.29	21.2	0.36	100.6	1.1	378.5	5.7	5.48E-17	1.16E-15
2007080001-11 Muscovite, J = 0.011009 ± 0.000018 (1σ)																
Aliquot 1																
1	0.001	0.001	-0.023	0.053	0.0063	0.0013	19.7	0.22	19.38	0.37	98.4	1.6	348.9	6	4.33E-17	8.53E-16
2	0.00077	0.00016	0.005	0.011	0.00735	0.00046	19.78	0.079	19.55	0.093	98.84	0.29	351.7	1.5	2.54E-16	5.03E-15
3	0.000738	0.000083	0.0041	0.0036	0.00574	0.00036	19.395	0.085	19.173	0.088	98.86	0.19	345.5	1.4	6.17E-16	1.20E-14
4	0.000169	0.00007	0.0026	0.0034	0.00703	0.00043	19.28	0.084	19.228	0.086	99.74	0.2	346.4	1.4	6.61E-16	1.27E-14
5	0.00046	0.00013	0.0005	0.0066	0.00696	0.00029	19.3	0.079	19.162	0.087	99.29	0.29	345.3	1.4	3.47E-16	6.70E-15
6	0.00056	0.00014	0.0151	0.0079	0.00582	0.00041	19.185	0.084	19.019	0.094	99.14	0.29	343	1.5	2.94E-16	5.64E-15
7	0.00008	0.00014	0.0008	0.009	0.00637	0.00051	19.132	0.074	19.105	0.085	99.87	0.31	344.4	1.4	3.10E-16	5.93E-15
8	0.000264	0.000082	0.0091	0.0051	0.00703	0.00033	19.168	0.074	19.089	0.078	99.59	0.21	344.1	1.3	5.89E-16	1.13E-14
9	0.00031	0.00011	0.0118	0.0056	0.00654	0.00045	19.196	0.072	19.103	0.079	99.52	0.25	344.4	1.3	3.67E-16	7.04E-15
10	0.00079	0.00032	0.005	0.016	0.00544	0.00068	19.47	0.11	19.23	0.14	98.79	0.53	346.5	2.3	1.37E-16	2.67E-15
11	0.002	0.0013	0.095	0.068	0.0019	0.0016	19.15	0.26	18.57	0.47	97	2.1	335.6	7.7	3.26E-17	6.25E-16
12	0.00144	0.00071	0.032	0.04	0.00884	0.00093	19.81	0.18	19.38	0.27	97.8	1.1	348.9	4.5	6.14E-17	1.22E-15
Aliquot 2																
1	0.00255	0.00099	0.007	0.056	0.0103	0.0016	20.74	0.27	19.98	0.4	96.3	1.5	358.7	6.5	3.93E-17	8.16E-16
2	0.00224	0.00017	0.0001	0.0062	0.00823	0.00054	20.299	0.077	19.631	0.092	96.71	0.32	353	1.5	3.49E-16	7.09E-15
3	0.000502	0.000067	-0.0028	0.0032	0.00644	0.00046	19.299	0.069	19.147	0.071	99.22	0.17	345.1	1.2	6.76E-16	1.31E-14
4	0.000416	0.000093	0.0052	0.0066	0.00809	0.00038	19.252	0.071	19.127	0.076	99.36	0.24	344.7	1.2	5.13E-16	9.87E-15

Step #	$^{36}Ar/^{39}Ar$	± (1σ)	$^{37}Ar/^{39}Ar$	± (1σ)	$^{38}Ar/^{39}Ar$	± (1σ)	$^{40}Ar/^{39}Ar$	± (1σ)	$^{40}Ar^*/^{39}Ar$	± (1σ)	$\%^{40}Ar^*$	± (1σ)	Age (Ma)	± (1σ)	^{39}Ar Moles	^{40}Ar Moles
5	0.00075	0.00019	0.0228	0.0096	0.00766	0.00061	19.534	0.091	19.31	0.11	98.86	0.34	347.8	1.7	2.38E-16	4.65E-15
6	0.000471	0.000085	0.004	0.0036	0.00682	0.00028	19.383	0.074	19.241	0.078	99.27	0.22	346.6	1.3	6.10E-16	1.18E-14
7	0.00019	0.00013	0.005	0.013	0.00624	0.0006	19.265	0.087	19.208	0.095	99.71	0.33	346.1	1.6	3.36E-16	6.47E-15
8	0.00036	0.00012	0.0007	0.0081	0.00706	0.00037	19.319	0.071	19.21	0.079	99.44	0.25	346.1	1.3	3.81E-16	7.36E-15
9	0.00032	0.00011	-0.0005	0.0081	0.00847	0.00027	19.295	0.075	19.199	0.082	99.51	0.26	345.9	1.3	4.28E-16	8.26E-15
10	0.00118	0.00031	0.015	0.021	0.00606	0.00053	19.43	0.11	19.08	0.14	98.19	0.52	343.9	2.3	1.45E-16	2.81E-15
11	0.00008	0.00045	0	0.024	0.00599	0.0007	19.6	0.15	19.57	0.2	99.87	0.74	352.1	3.3	1.11E-16	2.17E-15

Appendix 3. Tabulated $^{40}Ar/^{39}Ar$ data for samples from the Oasis deposit, Queensland.

Step #	$^{36}Ar/^{39}Ar$	± (1σ)	$^{37}Ar/^{39}Ar$	± (1σ)	$^{38}Ar/^{39}Ar$	± (1σ)	$^{40}Ar/^{39}Ar$	± (1σ)	$^{40}Ar^*/^{39}Ar$	± (1σ)	$\%^{40}Ar^*$	± (1σ)	Age (Ma)	± (1σ)	^{39}Ar Moles	^{40}Ar Moles
2007167006-04 Biotite, J = 0.011009 ± 0.000018 (1σ)																
Aliquot 1																
1	0.00115	0.00017	-0.006	0.0035	0.00702	0.00044	24.6	0.12	24.26	0.13	98.6	0.25	427	2	5.57E-16	1.37E-14
2	0.000699	0.00008	0	0.003	0.00712	0.00023	25.02	0.11	24.81	0.11	99.16	0.17	435.6	1.7	5.81E-16	1.45E-14
3	0.00068	0.00011	0.001	0.0033	0.00688	0.00031	25	0.11	24.8	0.11	99.19	0.21	435.4	1.8	5.99E-16	1.50E-14
4	0.00061	0.00013	-0.0016	0.0051	0.00639	0.00031	24.97	0.11	24.79	0.11	99.27	0.24	435.3	1.7	4.50E-16	1.12E-14
5	0.00075	0.00016	0.0093	0.0063	0.00506	0.0005	24.64	0.1	24.42	0.11	99.1	0.28	429.5	1.8	3.11E-16	7.67E-15
6	0.00041	0.00016	0.0017	0.0083	0.00673	0.00034	24.72	0.13	24.6	0.13	99.51	0.32	432.3	2.1	2.62E-16	6.47E-15
7	0.00069	0.0003	-0.004	0.018	0.00758	0.00052	25.15	0.16	24.94	0.18	99.18	0.41	437.7	2.9	1.80E-16	4.52E-15
8	0.00115	0.0005	0.029	0.034	0.00819	0.0008	24.69	0.22	24.35	0.26	98.61	0.67	428.4	4.1	8.77E-17	2.17E-15
9	-0.00012	0.00054	0.004	0.024	0.00686	0.00085	24.94	0.2	24.98	0.26	100.14	0.68	438.3	4.1	7.70E-17	1.92E-15
10	-0.0018	0.0049	0.12	0.25	0.0078	0.0074	23.7	1.4	24.3	2	102.3	6.3	428	32	8.50E-18	2.02E-16
11	0.011	0.01	0.48	0.84	0.02	0.014	25.8	3.3	22.4	4.2	87	12	398	66	3.87E-18	9.98E-17
12	0.0006	0.0097	0.41	0.58	0.004	0.01	19.2	2.1	19	3.6	99	15	343	58	4.57E-18	8.76E-17
Aliquot 2																
1	0.00067	0.00027	0.008	0.012	0.00791	0.00064	22.44	0.12	22.24	0.15	99.11	0.42	395	2.3	1.64E-16	3.68E-15
2	0.00064	0.00013	0.0095	0.0049	0.00773	0.00026	24.78	0.1	24.59	0.11	99.23	0.24	432.3	1.7	3.80E-16	9.41E-15
3	0.000359	0.000089	0.008	0.0029	0.00671	0.00034	24.83	0.11	24.72	0.11	99.57	0.17	434.3	1.7	5.90E-16	1.47E-14
4	0.0003	0.00009	0.0129	0.0045	0.00828	0.00023	24.66	0.11	24.57	0.11	99.64	0.18	431.9	1.8	5.32E-16	1.31E-14
5	0.00033	0.00011	0.0078	0.0039	0.00606	0.00044	24.549	0.093	24.452	0.098	99.61	0.23	430.1	1.5	4.73E-16	1.16E-14
6	0.00049	0.00013	0.0151	0.0056	0.00707	0.00035	24.79	0.1	24.64	0.11	99.41	0.25	433	1.7	3.55E-16	8.80E-15
7	0.00056	0.0002	0.0191	0.0081	0.00703	0.00041	25.02	0.11	24.86	0.13	99.33	0.34	436.4	2	2.45E-16	6.13E-15
8	0.00054	0.00028	0.024	0.012	0.00766	0.00062	24.88	0.14	24.72	0.16	99.35	0.4	434.2	2.6	1.65E-16	4.10E-15
9	0.00048	0.00096	0.066	0.024	0.0046	0.001	24.53	0.23	24.39	0.36	99.4	1.2	429	5.7	8.77E-17	2.15E-15
10	0.0003	0.0073	0.82	0.25	0.0081	0.0073	23.7	1.9	23.7	2.9	99.9	9.4	418	45	7.72E-18	1.83E-16
11	0.0008	0.004	0.35	0.15	0.0189	0.0046	22.9	1.1	22.7	1.6	99	5.3	403	25	1.24E-17	2.85E-16
2007167006-04 Muscovite, J = 0.011009 ± 0.000018 (1σ)																
Aliquot 1																
1	0.0017	0.0024	-0.32	0.12	0.0025	0.0029	26.62	0.74	26.1	1	98	2.7	455	16	1.84E-17	4.91E-16
2	0.00138	0.00031	-0.013	0.012	0.00772	0.00051	25.82	0.14	25.4	0.17	98.4	0.4	444.9	2.6	1.71E-16	4.43E-15
3	0.00241	0.00042	0.008	0.016	0.00584	0.00036	25.5	0.14	24.78	0.19	97.17	0.53	435.2	2.9	2.21E-16	5.63E-15
4	0.0025	0.0014	-0.113	0.038	0.0104	0.0013	25.84	0.27	25.08	0.48	97.1	1.6	439.8	7.5	5.24E-17	1.35E-15
5	-0.0008	0.003	-0.1	0.13	0.009	0.0024	25.84	0.51	26.1	1	100.9	3.5	455	16	2.40E-17	6.21E-16
6	0.0024	0.0028	-0.14	0.084	0.0082	0.0019	25.82	0.42	25.1	0.92	97.2	3.2	440	14	2.79E-17	7.20E-16
7	-0.001	0.0018	-0.14	0.14	0.009	0.002	24.65	0.49	24.94	0.72	101.2	2.2	438	11	2.38E-17	5.87E-16
8	-0.0003	0.0055	-0.24	0.19	0.0115	0.0038	25.32	0.87	25.4	1.8	100.2	6.5	444	29	1.21E-17	3.07E-16
9	-0.026	0.011	-0.3	1.2	-0.018	0.012	25	2.7	32.7	4.7	131	13	554	69	3.54E-18	8.84E-17
10	0.015	0.056	-7.1	4.6	0.072	0.069	35	17	29	22	85	48	500	320	6.79E-19	2.35E-17
11	-0.092	0.077	-9.1	5	0.011	0.073	30	15	57	33	188	63	880	400	6.59E-19	2.01E-17
12	-0.086	0.075	-11.9	7	-0.052	0.072	38	20	63	37	165	47	950	430	6.25E-19	2.40E-17

Step #	$^{36}Ar/^{39}Ar$	± (1σ)	$^{37}Ar/^{39}Ar$	± (1σ)	$^{38}Ar/^{39}Ar$	± (1σ)	$^{40}Ar/^{39}Ar$	± (1σ)	$^{40}Ar^*/^{39}Ar$	± (1σ)	$\%^{40}Ar^*$	± (1σ)	Age (Ma)	± (1σ)	^{39}Ar Moles	^{40}Ar Moles
Aliquot 2																
1	0.0037	0.0021	-0.049	0.098	0.0009	0.0023	28.38	0.66	27.25	0.89	96	2.3	473	14	2.15E-17	6.09E-16
2	0.0014	0.0002	0.0014	0.0086	0.00676	0.00043	25.15	0.11	24.73	0.13	98.34	0.33	434.5	2	2.39E-16	6.01E-15
3	0.0009	0.00099	-0.02	0.044	0.0042	0.0013	25.61	0.35	25.34	0.45	98.9	1.2	443.9	7.1	4.75E-17	1.22E-15
4	0.00249	0.00037	0.01	0.016	0.00641	0.00064	25.5	0.18	24.75	0.2	97.08	0.48	434.8	3.2	1.27E-16	3.23E-15
5	0.00111	0.0002	0.0011	0.0095	0.00616	0.00059	25.17	0.12	24.83	0.14	98.68	0.33	436	2.1	2.32E-16	5.83E-15
6	0.00136	0.0004	0.006	0.023	0.00531	0.00071	25.31	0.2	24.9	0.23	98.39	0.52	437.1	3.6	1.11E-16	2.80E-15
7	0.0013	0.0016	-0.094	0.076	0.0051	0.0018	25.78	0.47	25.39	0.66	98.5	1.9	445	10	2.79E-17	7.19E-16
8	0.0042	0.0015	0.054	0.067	0.0055	0.0019	25.1	0.45	23.84	0.61	95	1.8	420.5	9.6	2.84E-17	7.13E-16
9	0.00074	0.00051	-0.031	0.023	0.00655	0.0007	25.25	0.22	25.03	0.27	99.12	0.64	439	4.2	8.43E-17	2.13E-15
2007167005-03 Biotite, J = 0.011009 ± 0.000018 (1σ)																
Aliquot 1																
1	0.00132	0.00028	0.036	0.014	0.0051	0.00046	23.51	0.13	23.12	0.15	98.33	0.4	409	2.4	1.62E-16	3.81E-15
2	0.0017	0.00013	0.0091	0.0051	0.00711	0.00029	25.677	0.096	25.17	0.1	98.03	0.24	441.3	1.6	3.88E-16	9.97E-15
3	0.000391	0.000067	0.0103	0.003	0.006	0.00026	25.1	0.1	24.99	0.1	99.54	0.18	438.4	1.6	7.36E-16	1.85E-14
4	0.000286	0.000071	0.0036	0.0037	0.00743	0.00038	25.156	0.098	25.07	0.1	99.66	0.18	439.7	1.6	7.28E-16	1.83E-14
5	0.00021	0.00018	0.0014	0.0044	0.00786	0.00034	24.973	0.097	24.91	0.11	99.75	0.27	437.2	1.7	5.14E-16	1.28E-14
6	0.00051	0.00013	0.0195	0.0058	0.00549	0.00056	24.94	0.1	24.79	0.11	99.4	0.27	435.3	1.7	3.77E-16	9.41E-15
7	0.00059	0.00019	0.01	0.01	0.00574	0.00051	25.18	0.11	25.01	0.13	99.3	0.33	438.7	2	2.39E-16	6.01E-15
8	0.00032	0.00031	0.028	0.018	0.00579	0.00063	25.04	0.18	24.95	0.2	99.62	0.43	437.8	3.1	1.26E-16	3.16E-15
9	-0.00081	0.00071	0.012	0.031	0.0082	0.0011	25.38	0.28	25.62	0.35	100.95	0.89	448.3	5.5	6.14E-17	1.56E-15
10	0.0078	0.0067	0.13	0.39	0.007	0.0073	22.5	1.7	20.2	2.5	89.7	9	362	41	6.44E-18	1.45E-16
11	-0.0003	0.0022	0.01	0.12	0.0057	0.0029	24.23	0.7	24.33	0.96	100.4	2.7	428	15	1.78E-17	4.31E-16
Aliquot 2																
1	0.00315	0.00025	0.02	0.012	0.00584	0.00055	24.39	0.13	23.44	0.15	96.14	0.34	414.2	2.3	2.00E-16	4.88E-15
2	0.00078	0.00011	0.0072	0.0056	0.00604	0.00045	25.316	0.094	25.084	0.1	99.08	0.22	439.9	1.6	4.54E-16	1.15E-14
3	0.000447	0.000061	0.0034	0.0025	0.00655	0.00041	25.182	0.076	25.048	0.079	99.47	0.13	439.4	1.2	8.85E-16	2.23E-14
4	0.000517	0.000073	0.0051	0.0029	0.00734	0.00035	25.32	0.1	25.16	0.1	99.39	0.17	441.1	1.6	8.75E-16	2.22E-14
5	0.000498	0.000081	0.0015	0.0037	0.00505	0.00034	25.094	0.086	24.945	0.089	99.41	0.17	437.7	1.4	7.20E-16	1.81E-14
6	0.00041	0.000098	-0.0078	0.0053	0.00691	0.00036	25.104	0.094	24.979	0.098	99.51	0.2	438.3	1.5	4.95E-16	1.24E-14
7	0.0006	0.00017	0.0273	0.0086	0.00792	0.00032	25.26	0.12	25.08	0.13	99.3	0.33	439.9	2	2.72E-16	6.87E-15
8	0.00238	0.00052	-0.015	0.029	0.00715	0.00097	25.34	0.21	24.63	0.25	97.19	0.67	432.8	4	8.86E-17	2.24E-15
9	0.0033	0.0014	-0.07	0.078	0.0071	0.0016	25.67	0.42	24.68	0.59	96.1	1.8	433.6	9.2	3.19E-17	8.20E-16
10	0.0134	0.0047	0.25	0.26	0.0145	0.0049	25.2	1.2	21.2	1.7	84.2	5.6	379	28	8.84E-18	2.23E-16
11	0.0058	0.0035	-0.07	0.21	0.0166	0.004	25.32	0.91	23.6	1.3	93.2	4.2	416	21	1.18E-17	2.99E-16
2007167005-03 Muscovite, J = 0.011009 ± 0.000018 (1σ)																
Aliquot 1																
1	0.00209	0.00054	0.05	0.026	0.00713	0.00088	20.12	0.18	19.5	0.24	96.91	0.87	350.8	3.9	8.54E-17	1.72E-15
2	0.00069	0.00022	0.039	0.011	0.00542	0.00053	24.56	0.13	24.35	0.15	99.18	0.32	428.5	2.3	2.07E-16	5.07E-15
3	0.0008	0.00017	0.0149	0.0077	0.00691	0.00035	24.65	0.11	24.41	0.12	99.03	0.27	429.4	1.8	2.76E-16	6.80E-15
4	0.00065	0.0002	0.016	0.011	0.00707	0.00048	24.59	0.13	24.39	0.14	99.22	0.33	429.2	2.3	2.27E-16	5.59E-15

Step #	$^{36}Ar/^{39}Ar$	± (1σ)	$^{37}Ar/^{39}Ar$	± (1σ)	$^{38}Ar/^{39}Ar$	± (1σ)	$^{40}Ar/^{39}Ar$	± (1σ)	$^{40}Ar^*/^{39}Ar$	± (1σ)	$\%^{40}Ar^*$	± (1σ)	Age (Ma)	± (1σ)	^{39}Ar Moles	^{40}Ar Moles
5	0.0007	0.00026	0.205	0.013	0.00646	0.00054	29.33	0.16	29.14	0.17	99.34	0.35	502	2.6	1.89E-16	5.55E-15
6	0.00016	0.00018	0.0236	0.01	0.00742	0.0005	24.47	0.11	24.43	0.12	99.81	0.29	429.7	1.9	2.64E-16	6.46E-15
7	-0.00005	0.00033	0.048	0.017	0.00538	0.00059	24.74	0.19	24.76	0.21	100.08	0.45	434.8	3.3	1.28E-16	3.17E-15
8	0.0008	0.00081	0.09	0.048	0.0023	0.0012	24.32	0.33	24.09	0.4	99	1.1	424.4	6.4	5.40E-17	1.31E-15
9	0.0002	0.0015	0.163	0.081	0.0018	0.0015	24.96	0.49	24.92	0.66	99.8	1.9	437	10	2.88E-17	7.19E-16
10	-0.007	0.008	0.85	0.43	0.0016	0.0078	23.5	2	25.6	3.2	109	10	449	50	5.27E-18	1.24E-16
11	0.0001	0.0013	0.146	0.061	0.0084	0.0013	24.85	0.39	24.84	0.54	99.9	1.6	436	8.5	3.43E-17	8.52E-16
Aliquot 2																
1	0.0003	0.00018	-0.003	0.01	0.00452	0.00049	22.07	0.11	21.98	0.12	99.59	0.33	391	1.9	2.63E-16	5.81E-15
2	0.00018	0.00014	-0.004	0.012	0.00452	0.00059	24.83	0.11	24.77	0.11	99.78	0.29	435.1	1.8	3.49E-16	8.67E-15
3	0.00008	0.00015	0.0102	0.0098	0.00597	0.00044	24.57	0.1	24.55	0.11	99.91	0.26	431.6	1.7	3.50E-16	8.61E-15
4	0.00023	0.00035	0.002	0.012	0.00497	0.00063	24.37	0.12	24.3	0.16	99.72	0.45	427.7	2.5	2.13E-16	5.19E-15
5	0.00018	0.00032	-0.027	0.017	0.00699	0.00058	24.51	0.15	24.45	0.17	99.77	0.44	430	2.7	1.38E-16	3.39E-15
6	0.0001	0.0003	-0.016	0.015	0.00661	0.00048	24.45	0.16	24.42	0.19	99.87	0.43	429.5	2.9	1.41E-16	3.44E-15
7	-0.00002	0.00056	-0.034	0.02	0.00675	0.00047	24.18	0.17	24.19	0.23	100.01	0.72	425.9	3.7	1.36E-16	3.29E-15
8	0.0013	0.001	-0.081	0.054	0.0049	0.00096	23.98	0.34	23.59	0.46	98.4	1.3	416.5	7.2	4.76E-17	1.14E-15
9	-0.0043	0.005	0.18	0.36	-0.0047	0.0048	25	1.5	26.3	2.2	105.2	6.1	459	33	9.87E-18	2.47E-16
10	0.0049	0.0082	-0.27	0.43	0.0139	0.0081	23.7	2.2	22.2	3.2	94	10	395	51	5.83E-18	1.38E-16
11	-0.0044	0.0044	-0.12	0.22	0.0095	0.0043	23	1.2	24.3	1.8	105.7	5.8	427	29	1.04E-17	2.38E-16

Appendix 4. Tabulated $^{40}Ar/^{39}Ar$ data for samples from the Maureen deposit, Queensland.

Step #	$^{36}Ar/^{39}Ar$	± (1σ)	$^{37}Ar/^{39}Ar$	± (1σ)	$^{38}Ar/^{39}Ar$	± (1σ)	$^{40}Ar/^{39}Ar$	± (1σ)	$^{40}Ar^*/^{39}Ar$	± (1σ)	$\%^{40}Ar^*$	± (1σ)	Age (Ma)	± (1σ)	^{39}Ar Moles	^{40}Ar Moles
2007167003-05 Muscovite, J = 0.011009 ± 0.000018 (1σ)																
Aliquot 1																
1	0.00217	0.00085	0.001	0.051	0.0088	0.0014	22.96	0.25	22.31	0.35	97.2	1.2	396.2	5.6	4.44E-17	1.02E-15
2	0.00016	0.00047	0.054	0.025	0.0088	0.00072	37.38	0.32	37.34	0.35	99.88	0.42	621.2	4.9	9.47E-17	3.54E-15
3	0.00049	0.00022	0.017	0.011	0.00565	0.00048	37.91	0.18	37.76	0.19	99.61	0.28	627.2	2.7	2.00E-16	7.57E-15
4	0.00107	0.0003	0.007	0.018	0.00722	0.00059	32.87	0.22	32.55	0.24	99.03	0.32	552.6	3.5	1.32E-16	4.33E-15
5	0.00046	0.00035	0.003	0.018	0.00569	0.00053	29.26	0.17	29.12	0.2	99.53	0.4	501.6	3	1.27E-16	3.72E-15
6	0.00063	0.001	0.009	0.063	0.0067	0.0013	29.37	0.37	29.18	0.47	99.4	1.1	502.6	7.1	3.96E-17	1.16E-15
7	0.0013	0.0016	0.069	0.095	0.0095	0.0023	31.42	0.53	31.04	0.7	98.8	1.6	530	10	2.63E-17	8.27E-16
8	0.001	0.00018	0.0086	0.0086	0.00705	0.00036	34.91	0.17	34.61	0.18	99.14	0.25	582.4	2.6	2.71E-16	9.47E-15
9	0.00116	0.00041	0.033	0.022	0.00744	0.00062	31.65	0.24	31.3	0.27	98.91	0.44	534.2	4	1.06E-16	3.36E-15
10	0.00082	0.00047	0.009	0.031	0.00763	0.0007	30.14	0.23	29.9	0.27	99.19	0.53	513.4	4	9.35E-17	2.82E-15
11	0.00078	0.00029	0.024	0.014	0.00481	0.00051	32.45	0.16	32.22	0.18	99.29	0.3	547.7	2.6	1.57E-16	5.10E-15
12	0.00009	0.00047	0.014	0.027	0.00745	0.00084	31.27	0.24	31.24	0.27	99.92	0.5	533.3	4	9.29E-17	2.91E-15
13	0.00079	0.00019	-0.017	0.011	0.00649	0.00052	34.11	0.18	33.88	0.19	99.31	0.26	571.8	2.7	2.22E-16	7.57E-15
14	0.00113	0.00042	0.012	0.039	0.00678	0.00085	31.74	0.25	31.4	0.27	98.94	0.44	535.7	4	1.03E-16	3.28E-15
15	-0.00068	0.00064	0.06	0.03	0.00627	0.00086	33.43	0.33	33.64	0.38	100.62	0.62	568.4	5.5	6.78E-17	2.27E-15
Aliquot 2																
1	0.00133	0.00064	0.008	0.032	0.00581	0.001	24.23	0.24	23.83	0.3	98.37	0.85	420.4	4.7	6.68E-17	1.62E-15
2	0.00098	0.00024	0.005	0.012	0.00651	0.0004	30.05	0.17	29.76	0.18	99.02	0.29	511.2	2.7	1.68E-16	5.05E-15
3	0.00101	0.00014	-0.0013	0.0061	0.00738	0.00049	31.27	0.13	30.97	0.14	99.04	0.22	529.3	2	3.59E-16	1.12E-14
4	0.00144	0.00035	0.002	0.016	0.00831	0.00064	30.85	0.19	30.42	0.22	98.61	0.38	521.1	3.2	1.30E-16	4.01E-15
5	0.00067	0.0003	-0.026	0.013	0.0065	0.00047	33.3	0.24	33.1	0.25	99.39	0.31	560.5	3.6	1.46E-16	4.88E-15
6	0.00074	0.00036	0.011	0.017	0.00412	0.00052	40.2	0.24	39.98	0.26	99.45	0.31	658	3.6	1.27E-16	5.10E-15
7	0.00089	0.00023	0.0042	0.01	0.00844	0.0006	35.85	0.19	35.59	0.2	99.26	0.31	596.4	2.8	1.90E-16	6.82E-15
8	0.00056	0.00017	0.0047	0.0073	0.00695	0.00046	31.31	0.14	31.15	0.15	99.47	0.24	531.9	2.2	2.91E-16	9.12E-15
9	0.0003	0.00022	0.0022	0.0098	0.00615	0.00034	32.89	0.18	32.8	0.19	99.73	0.33	556.2	2.8	2.06E-16	6.76E-15
10	-0.00045	0.00035	-0.013	0.016	0.00806	0.00062	32.82	0.22	32.95	0.24	100.4	0.36	558.4	3.5	1.31E-16	4.28E-15
11	0.00011	0.00037	-0.036	0.018	0.0061	0.00054	31.49	0.21	31.45	0.24	99.88	0.39	536.4	3.5	1.18E-16	3.72E-15
12	0.00039	0.00034	0.013	0.022	0.007	0.00057	33.31	0.22	33.19	0.24	99.66	0.34	561.9	3.5	1.40E-16	4.67E-15

Appendix 5. U-Pb isotope results for fluorite, Maureen uranium deposit, sample 2007167002-05

sample	weight (mg)	U (ppm)	Pb (ppm)	$^{232}Th/^{238}U$	Pb_{tot} (ng)	Pb_c (ng)	206/204 (a)	207/204 (a)	208/204 (a)	206/238 (b)	± (2s)	207/235 (b)	± (2s)	207/206 (b)	± (2s)	$^{206}Pb/^{238}U$ Age (Ma)	± (2s)	$^{207}Pb/^{235}U$ Age (Ma)	± (2s)	$^{207}Pb/^{206}Pb$ Age (Ma)	± (2s)	Disc. (c) %	rho 6-8 vs 7-5
NB25.5 ap	0.39	376.3	429.3	17.4	167.4	22.0	88.44	21.36	408.8	0.18219	0.186	2.0616	0.67	0.08207	0.61	1078.9	2.0	1136.1	7.6	1247	12	13.5	0.46
NB25.6 ap	0.28	505.0	411.1	17.3	115.1	16.0	87.77	21.31	402.3	0.13041	0.188	1.4789	0.68	0.08225	0.61	790.2	1.5	921.8	6.2	1251	12	36.8	0.46
NB25.7 ap	0.22	688.9	766.5	17.4	168.6	23.0	88.43	21.35	407.8	0.17774	0.238	2.0093	0.69	0.08199	0.61	1054.6	2.5	1118.6	7.7	1245	12	15.3	0.48
NB25.8 ap	0.22	224.6	266.0	17.3	58.5	7.9	88.27	21.33	405.5	0.18970	0.179	2.1438	0.67	0.08196	0.61	1119.7	2.0	1163.0	7.8	1245	12	10.1	0.46

Notes

Data reduction done using PBDAT 1.24 (Ludwig 1993)

model $^{232}Th/^{238}U$ estimated from radiogenic 208/206 and upper intercept age of 1240 Ma

Pb_{tot} is total Pb, Pb_c is common Pb; in nanogram

(a) corrected for mass bias, spike and blank

(b) corrected for mass bias, blank and common Pb; errors in % errors for Pb/U and Pb/Pb ages in Ma

(c) degree of discordance (normal) expressed as % (Disc% = 100*(207/206age - 206/238age) / 207/206age)

blank: 50±25 pg Pb, 5 ±2.5 pg U, blank isotopic composition: $^{206}Pb/^{204}Pb$ 17.05±0.2, $^{207}Pb/^{204}Pb$ 15.50±0.20, $^{208}Pb/^{204}Pb$ 36.82±0.20; errors 2sigma absolute

common Pb correction: 1200 Ma Pb from Stacey-Kramers Pb growth curve